Università
Ca'Foscari
Venezia

Scuola Dottorale di Ateneo
Graduate School

Dottorato di ricerca
in Scienze Chimiche
Ciclo XXVII
Anno di discussione 2016

Development of Analytes' Screening Methods using Voltammetric Techniques and Scanning Electrochemical Microscopy

SETTORE SCIENTIFICO DISCIPLINARE DI AFFERENZA: CHIM/01

Tesi di Dottorato di Pecchielan Giulia, matricola 816881

Coordinatore del Dottorato	**Tutore del Dottorando**
Prof. Maurizio Selva	**Prof. Salvatore Daniele**

A mia Nonna Ester, con tutto l'amore che ho

Contents

Abstract

As a result of several advantages offered by Scanning Electrochemical Microscopy (SECM) and Microcapillary techniques (MCs), there has been a great deal of interest in their development for probing a variety of materials either to make general characterisation at interfaces or to modify the surface with specific functionalities. In this thesis, both SECM and MC were used to investigate chemical phenomena taking place at interfaces with high spatial resolution or to perform local modifications of the surface. In particular, some strategies to fabricate/characterise silver micro- and nano-particles (AgNPs) either synthesised on purpose or that can be present in commercially available consumer goods are presented. New synthetic routes, making use of the MC and meniscus-based methods, or more traditional chemical and electrochemical approaches to produce micro- and nano-silver deposits were investigated. To rationalise some of the experimental results obtained with the MC technique, not previously reported theory, based on simulation, for the mass transport at the meniscus pipette end kept above a recessed conducting substrate, is presented and discussed.

The redox state of Ag in the silver particles and the local reactivity of the silver micro- and nano-particles, embedded in solid or soft matrices such as Nafion®, exopolysaccharides and commercially available goods are investigated by using SECM and stripping voltammetry. Due to their distinctive physicochemical and biological properties, AgNPs are of interest because they are widely used as antibacterial agent. The useful action of AgNPs seems to depend on the amount of free Ag^+ released in the media and relevant kinetic of the release. These measurements were performed by immersion of the silver-containing substrates in water or water/ethanol mixtures, which, according to the European Recommendation (10/2011), simulate the behavior of food matrices.

Finally, in order to promote the use of new nanostructured materials in sensor technology, an investigation was performed for establishing the properties of reduced graphene oxides (rGO) prepared by a pressure-wax based transferring technique, to be used as electrode materials. Thin layers of GOs were deposited as bands or disk in either inert or conducting substrates and investigated by SECM and voltammetry.

Sommario

I numerosi vantaggi offerti dalla Microscopia Elettrochimica a Scansione (SECM) e dalle tecniche microcapillari (MC) hanno visto di recente un loro crescente sviluppo e applicazione nello studio e la caratterizzazione di una grande varietà di materiali all'interfase substrato/soluzione. In questo lavoro di tesi, la SECM e la MC sono state usate per studiare fenomeni chimici che avvengono all'interfase solido/soluzione di sistemi costituiti da micro- e nano-particelle di argento preparati allo scopo, sfruttando diverse strategie di fabbricazione. Lo studio è stato rivolto anche a materiali contenenti AgNPs disponibili in commercio.

Per razionalizzare alcuni risultati sperimentali ottenuti con la tecnica MC, è stato presentato e discusso un approccio teorico, basato su metodi di simulazione digitale, mai riportato in precedenza in letteratura, per stabilire i fenomeni di trasporto di massa che si realizzano in corrispondenza del menisco liquido in contatto con un substrato conduttore recesso.

Lo stato redox di Ag presente nelle micro- e nano-particelle e la reattività locale delle stesse, incorporate in matrici solide o soft, quali Nafion®, esopolisaccaridi e prodotti disponibili in commercio, sono stati studiati utilizzando la SECM e la voltammetria nella versione *anodic stripping*. Il grande interesse verso materiali contenenti argento è dovuto alle loro peculiari proprietà chimico-fisiche e biologiche e per questo esse sono impiegate come sostanze antibatteriche. L'azione antibatterica di AgNPs dipende dalla quantità Ag^+ rilasciata e dalla velocità di rilascio nei mezzi con cui esse sono a contatto. Sono state pertanto eseguite misure di rilascio immergendo i vari substrati contenenti argento in acqua o miscele acqua/etanolo. Tali miscele, in accordo con la normativa europea vigente (Regolamento Europeo 10/2011), sono usate per simulare il comportamento di matrici alimentari.

Infine, allo scopo di promuovere l'uso di nuovi materiali nanostrutturati nella tecnologia di preparazione di sensori elettrochimici, è stata effettuata un'indagine per stabilire le proprietà di ossidi di grafene ridotto (rGO) preparati depositando ossidi di grafene su substrati sia isolanti che conduttori con la tecnica *pressure/wax-based transferring*. Strati sottili di GOs sono stati depositati sotto forma di bande e di dischi e sono stati sottoposti ad indagine mediante SECM e voltammetria.

Chapter 1: Introduction

The advent of microelectrodes during the early 1980s has led to a considerable development and application of electroanalytic methodologies based on amperometry and voltammetry.[1,2,3,4] A microelectrode is commonly defined as an electrode with at least one dimension sufficiently small, typically less than 50 μm[1,2,3.4]. Microelectrodes, therefore, can be fabricated in various geometries as is shown schematically in Fig. 1.1, for the commonest types employed. The advantages offered by microelectrodes in analytical chemistry come from their unique properties such as: low ohmic drop; high Faradaic to capacitive current ratio; high rate of diffusion to the microelectrode surface under steady state; quick achievement of steady state currents; possibility to operate with electrochemical cells in the two-electrode configuration and in small volume of sample[2,3,4]. Thanks to their properties, microelectrodes have been employed in many fields of electroanalysis, ranging from environmental[5,6], food[7], biomedical[8,9,10], material science[11] and at micro-locations, *e.g.*, in-vivo measurements[8].

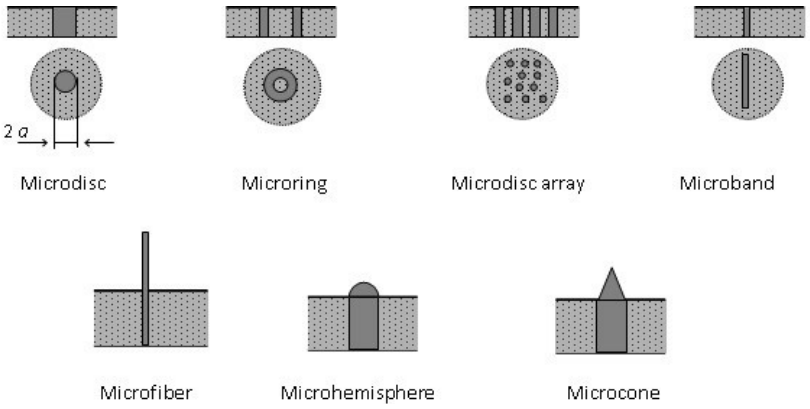

***Fig. 1.1**: Most common geometries of microelectrodes and microelectrode arrays.*

[1] M. I. Montenegro, M. A. Queirós, J. L. Daschbach, Microelectrodes: Theory and Applications, Eds., Proceedings of the NATO ASI Series E197, Kluwer Academic Press, **1990**.
[2] K. Štulik, C. Amatore, K. Holub, V. Mareček, W. Kutner, *Pure and Applied Chemistry* (Technical Report) **2000**, 72, 1483-1492.
[3] M. R. Deakin, D. Wipf, R. M. Wightman, *J. Electrochem. Soc.* **1986**, 133, C135–C135.
[4] M. Fleischmann, S. Pons, D. R. Rolison, P. P. Schmidt, *Ultramicroelectrodes* **1987**, Datatech Systems Inc., Morganton, NC, p. 363.
[5] F. Davis, S. P. J. Higson, *Environ. Sci.: Processes Impacts* **2013**, 15, 1477–1489.
[6] F. Tan, J. P. Metters, C. E. Banks, *Sensors and Actuators B: Chemical* **2013**, 181, 454–462.
[7] K. Peckova, J. Barek, *Curr. Organic Chem.* **2011**, 15, 3014–3028.
[8] S. Marinesco, O. Frey, *Neuromethods* (eds S.Marinesco and N.Dale) **2013**, vol. 80, Microelectrode Biosensors, 3–25.
[9] X. P. Sun, Y. L. Luo, F. Liao, W. Lu, G. Chang, *Electrochim. Acta* **2011**, 56, 2832–2836.
[10] O. Ordeig, J. del Campo, F. X. Munoz, C. E. Banks, R. G. Compton, *Electroanalysis* **2007**, 19, 1973–1986.
[11] C. M. Li, W. H. Hu, *J. Electroanal. Chem.* **2013**, 688, 20–31.

Recently, microelectrodes have been employed to characterize and even detect metal and metal oxide nanoparticles (MNPs) (*i.e.*, silver, gold, platinum, copper, nickel, iridium, titanium and their oxides), which are nowadays widely used in electronics, medicine, energy production and consumer goods. For these studies, various detection strategies have been developed, most of them are based on the impact frequency of the MNPs with the microelectrode surface[12,13,14,15,16,17,18]. The small electrode surface limits the number of nanoparticles that can interact with it, thus simplifying the interpretation of the electrochemical responses. The unique properties of microelectrodes and their theoretical achievements have had a significant impact also in the development of the new electroanalytical techniques such as Scanning Electrochemical Microscopy (SECM) and Microcapillary Amperometry/Voltammetry[19,20], which can be included within the Scanning Probe Microscopy (SPM) techniques.

1.1 Scanning Probe Microscopy

The introduction of Scanning Probe Microscopies (SPMs) has had a considerable impact on the knowledge of the local structure and reactivity of surfaces and interfaces. These techniques, developed during the 1980s, use the response of a micro- or nano-probe, the latter being scanned close to or in contact with an interface, to create an image of the topography or some other property of interest. The family of SPMs includes Scanning Tunneling Microscopy (STM), Atomic Force Microscopy (AFM), Scanning Electrochemical Microscopy (SECM) and Microcapillary (MC).

In STM, a bias voltage is applied between a sharp conductive tip and a conductive sample. At a distance of few nanometers, tunneling current flows between the sample and the tip and provides topographical information with atomic resolution. In AFM a cantilever, which has a sharp tip at the end, is deflected by short range forces between the tip and a non conductive surface. The measurement of these deflection is usually carried out by bouncing focused laser diode light off of the cantilever. By recording the motion of the laser beam as a function of the tip position, sample topography can be constructed and displayed. In SECM, the tip is a microelectrode and the tip signal is usually a Faradaic current resulting from oxidation/reduction of solution species; in some cases, SECM experiments use an ion-selective electrode as tip. Since the performance of a variety of biological and nanotechnological systems is based on electrochemical processes, SECM represents a

[12] A. Boika, S. N. Thorgaard, A. J. Bard, *J. Phys. Chem. B* **2013**, 117, 4371–4380.
[13] X. Y. Xiao, A. J. Bard, *J. Am. Chem. Soc.* **2007**, 129, 9610–9612.
[14] S. J. Kwon, F. R. F. Fan, A. J. Bard, *J. Am. Chem. Soc.* **2010**, 132, 13165– 13167.
[15] S. J. Kwon, H. J. Zhou, F. R. F. Fan, V. Vorobyev, B. Zhang, A. J. Bard, *Phys. Chem. Chem. Phys.* **2011**, 13, 5394–5402.
[16] E. J. E. Stuart, N. V. Rees, J. T. Cullen, R. G. Compton, *Nanoscale* **2013**, 5, 174–177.
[17] E. J. E. Stuart, Y. G. Zhou, N. V. Rees, R. G. Compton, *RSC Advances* **2012**, 2, 6879–6884.
[18] Y. G. Zhou, N. V. Rees, J. Pillay, R. Tshikkudo, S. Vilakazi, R. G. Compton, *Chem. Commun.* **2012**, 48, 224– 226.
[19] N. Aydemir, J. Parcell, C. Laslau, M. Nieuwoudt, D. E. Williams, J. Travas-Sejdic, *Macromol. Rapid Commun.* **2013**, 34, 1296-1300.
[20] C. Laslau, D.E. Williams, B. Kannan, J. Travas-Sejdic, *Adv. Funct. Mater.* **2011**, 21, 4607-4616.

powerful route for their full characterization. A further advantage offered by SECM compared with other SPMs is the availability of well-developed quantitative theory.

Microcapillary techniques (MCs) have been introduced, recently, for high-resolution imaging of conducting surfaces, microfabrication and to perform micro- and nano-electrochemistry onto a variety of substrate materials. In MCs, the probe is a laser pulled pipette or theta pipette, which is filled with an electrolyte solution, which forms a protruded meniscus at the pipette end. In the case of a single barrelled micropipette a two-electrode electrochemical cell is formed by a pseudo-reference/counter electrode, which is immersed in the solution within the pipette, and a working electrode made by the small portion of the substrate that comes into contact with the electrolyte solution[21,22].

1.2 Scanning Electrochemical Microscopy

Scanning Electrochemical Microscopy was coined by Bard and coworkers in 1989. However, from a historical point of view, it was already over the 1940s that the concept of localized electrochemical study took place, thanks to the work of Evans[23], who performed potentiometric measurements for probing corrosion events, and Davies[24] who recorded amperometric responses in biological tissues of animals. It was only during the 1980s that the concept of localized study was developed by Engstrom and coworkers[25,26,27], who investigated the properties of the diffusion layer of a larger active electrode by the use of a microelectrode. Few years later, Bard and coworkers described the use of a microelectrode tip held by a three-dimensional micropositioning system as a scanning electrochemical microscope, from which the acronym SECM comes from. Since then on, a series of papers have been published on principles[28,29], theory[30] and applications[31] of SECM, which have provided the framework and foundations for many of the subsequent development in this field. The versatility and innovation introduced by SECM is testified by the increasing number of articles, reviews and books published on the subject, since the SECM technique has been set-up. Figure 1.2 (A and B) illustrates the frequency of publications on SECM by year (1 A) and by Country (1 B) in the period 1989 end July 2015; the sources are Scopus and Web of Science.

[21] C. Kranz, *Analyst* **2014**, 139, 336-352.
[22] N. Ebejer, A. G. Guell, S. C. S. Lai, K. McKelvey, M. E. Snowden, P. R. Unwin, *Annu. Rev. Anal. Chem.* **2013**, 6, 329-351.
[23] U. R. Evans, *Journal of the Iron and Steel Institute* **1940**, 141, 219–234.
[24] P. W. Davies, F. Jr Brink, *Review of Scientific Instruments* **1942**, 13, 524–533.
[25] R. C. Engstrom, M. Weber, D. J. Wunder, R. Burgess, S. Winquist, *Anal. Chem.* **1986**, 58, 844–848.
[26] R. C. Engstrom, T. Meaney, R. Tople, R. M. Wightman, *Anal. Chem.* **1987**, 59, 2005– 2010.
[27] R. C. Engstrom, R. M. Wightman, E. W. Kristensen, *Anal. Chem.* **1988**, 60, 652–656.
[28] A. J. Bard, F. R. F. Fan, J. Kwak, O. Lev, *Anal. Chem.* **1989**, 61, 132–138.
[29] A. J. Bard, M. V. Mirkin, *Scanning Electrochemical Microscopy*, Marcel Dekker, Inc, New York, **2001**.
[30] J. Kwak, A. J. Bard, *Anal. Chem.* **1989**, 61, 1221–1227.
[31] J. Kwak, A. J. Bard, *Anal. Chem.* **1989**, 61, 1794– 1799.

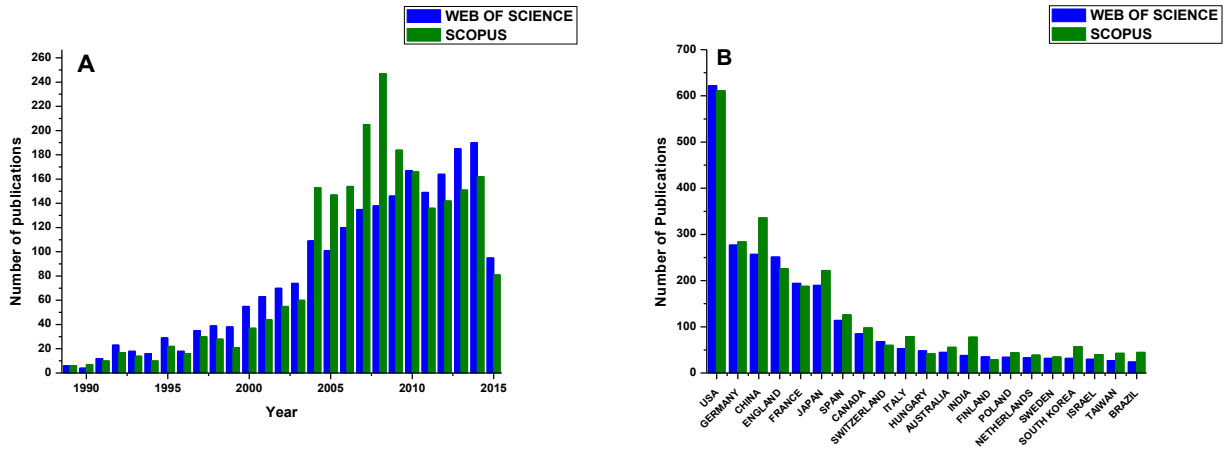

***Fig. 1.2**: A) Number of publications on Scanning Electrochemical Microscopy per year and B) per Country in the period 1989/July 2015; bibliographic research performed with Web of Science and Scopus. Keywords: scanning-electrochemical-microscopy and refine for article, review, book and book chapter, depending on the browser.*

The main research topics investigated by SECM are concerned with the general field of *Chemistry* (1500 articles), *Electrochemistry* (870 articles) and Material Science (420 articles) for a wide variety of processes, spanning from metal corrosion to metabolism in single living cells. To provide some examples, SECM has found application in fundamental electrochemistry, bioanalytical electrochemistry, catalyst screening, corrosion studies, molecular transport, surface patterning and modification[32,33] with direct mode[34,35,36,37,38] and feedback mode [39,40,41,42,43]. SECM is used to study electron transfer kinetics at solid/liquid interfaces[44,45], to detect and image regions with different catalytic activities[46,47,48]. In the latter topic, most of the articles published were concerned with the hydrogen oxidation and the oxygen reduction processes, which are of great importance for fuel cells, bio-fuel cells and air batteries applications[49,50,51,52,53].

[32] S. M. Oja, M. Wood, B. Zhang, *Anal. Chem.* **2013**, 85, 473-486.
[33] D. Battistel, S. Daniele, D. Fratter, *Electrochim. Acta* **2012**, 78, 557-562.
[34] L. Stratmann, J. Clausmeyer, W. Schuhmann, *ChemPhysChem* **2015**, article in press.
[35] J. Claumeyer, J. Henig, W. Schuhmann, N. Plumeré, *ChemPhysChem* **2014**, 15, 151-156.
[36] T. Danieli, D. Mandler, *J. Solid State Electrochem.* **2013**, 17, 2989-2997.
[37] F. Grisotto, A. Ghorbal, C. Goyer, J. Charlier, S. Palacin, *Chem. Mater.* **2011**, 23, 1396-1405.
[38] F. Hanquier, T. Matrab, F. Kanoufi, C. Combellas, *Electrochim. Acta* **2009**, 54, 5127-5136.
[39] Y. Kanno, K. Ino, K. V. Inoue, M. Sen. A. Suda, R. Kunikata, M. Matsudaira, H. Abe, C.-Z. Li, H. Shiku, T. Matsue, *J. ELectroanal. Chem* **2015**, 741, 109-113.
[40] X. Wang, Y. Xia, Y. Zhan, L. Nie, F. Cao, J. Zhang, C. Cao, *Acta Metall. Sinica* **2015**, 51, 631-640.
[41] W. Liu, F. Cao, Y. Xia, L. Chang, J. Zhang, *Electrochim. Acta* **2014**, 132, 377-388.
[42] L. Han, Y. Yuan, J. Zhang, X. Zhao, Y. Cao, Z. Hu, Y. Yan, S. Dong, Z.-Q. Tian, Z.-W. Tian, D. Zhan, *Anal. Chem*. **2013**, 85, 1322-1326.
[43] R. Cornut, S. Poisier, J. Manzeroll, *Anal. Chem*. **2012**, 84, 3531-3537.
[44] R. M. Penner, M. J. Heben, T. L. Longin, N. S. Lewis, *Science* **1990**, 250, 1118-1121.
[45] Y. Wang, J. Velmurugan, M. V. Mirkin, *Isr. J. Chem.* **2010**, 50, 291-305.
[46] Y. Selzer, I. Turyan, D. Mandler, *J. Phys. Chem B* **1999**, 103, 1509-1517.
[47] J. Zhou, Y Zu, A. J. Bard, *J. Electroanal. Chem.* **2000**, 491, 22-29.
[48] S. Jayaraman, A. C. Hillier, *J. Combinat. Chem.* **2004**, 6, 27-31.
[49] J. Fernández, A. J. Bard, *Anal. Chem.* **2003**, 75, 2967-2974.

In the biological field, SECM has been employed for studying: the transport of molecules across biological cell membranes, including planar bilayer lipid membranes and liposomes[54,55], living cells for monitoring respiration and other cellular function and redox processes[56,57,58,59,60,61,62].

In the field of material science, SECM has been employed for the characterization of one-dimensional substrate like single-walled carbon nanotubes (SWCNT)[63]; the determination of heterogeneous electron transfer rate constant and imaging the reactivity of various types of graphenic substrates prepared by using different synthetic either physical or chemical approaches (CVD, bubble method, lithography, ink-jet printing)[64,65].

The growing interest on SECM is therefore due to the wide spectrum of systems that can be investigated and the information that can be acquired. This can also be achieved through the combination of SECM with other scanning probe microscopies and electrochemical techniques. The combination of various techniques allows obtaining complementary information during imaging of the sample surface.

A great number of analytical techniques have been combined with SECM and these include near-field scanning optical microscopy (NSOM), surface plasmon resonance (SPR), electrochemical quartz crystal microbalance (EQCM), fluorescence spectroscopy (FS), electrogenerated chemiluminescence (ECL) and atomic force microscopy (AFM). Among these hybrid techniques, AFM-SECM is the most widely used for the positioning capabilities[66,67,68]. In the applications exposed above, the tips are solid electrodes, but recently pipette-based probes have also been implemented[69]. These systems operates in a similar manner as those for SECM.

[50] F. Li, I. Ciani, P. Bertoncello, P. R. Unwin, J. J. Zhao, C. R. Bradbury, D. J. Fermin, *J. Phys. Chem. C* **2008**, 112, 9686-9694.
[51] J. W. Lee, H. C. Ye, S. L. Pan, A. J. Bard, *Anal. Chem.* **2008**, 80, 7445-7450.
[52] J. Zhang, C. J. Slevin, C. Morton, P. Scott, D. J. Walton, P. R. Unwin, *J. Phys. Chem. B* **2001**, 105, 11120-11130.
[53] A. P. O'Mullane, J. V. Macpherson, J. Cervera-Montesinos, J. A. Manzanares, F. Frehill, J. G. Vos, P. R. Unwin, *J. Phys. Chem. B* **2004**, 108, 7219-7227.
[54] M. Tsionsky, J. Zhou, S. Amemiya, F.-R. Fan, A. J. Bard, R. A. Dryfe, *Anal. Chem.* **1999**, 71, 4300-4305.
[55] S. Amemiya, A. J. Bard, *Anal. Chem.* **2000**, 72, 4940-4948.
[56] R. K. Zhu, S. M. Macfie, Z. F. Ding, *J. Exp. Bot.* **2005**, 56, 2831-2838.
[57] K. B. Holt, A. J. Bard, *Biochemistry* **2005**, 44, 13214-13223.
[58] B. Liu, S. A. Rotenberg, M. V. Mirkin, *Proc. Natl. Acad. Sci. U.S.A.* **2000**, 97, 9855-9860.
[59] J. H. Shim, Y. Lee, *Anal. Chem.* **2009**, 81, 8571-8576.
[60] S. Bergner, P. Palatzky, J. Wegener, F. M. Matysik, *Electroanalysis* **2011**, 23, 196-200.
[61] Y. Takahashi, H. Shiku, T.Murata, T. Yasukawa, T.Matsue, *Anal. Chem.* **2009**, 81, 9674-9681.
[62] P. Sun, F. O. Laforge, T. P. Abeyweera, S. A. Rotenberg, J. Carpino, M. V. Mirkin, *Proc. Natl. Acad. Sci. U.S.A.* **2008**, 105, 443-448.
[63] H. Xiong, D. A. Gross, J. Guo, S. Amemiya, *Anal. Chem.* **2006**, 78, 1946-1957.
[64] A. Ambrosi, C. K. Chua, A. Bonanni, M. Pumera, *Chem. Rev.* **2014**, 114, 7150-7188.
[65] J. Azevedo, C. Bourdillon, V. Derycke, S. Campidelli, C. Lefrou, R. Cornut, *Anal. Chem.* **2013**, 85, 1812-1818.
[66] J. V. Macpherson, P. R. Unwin, *Anal. Chem.* **2000**, 72, 276-285.
[67] J. V. Macpherson, P. R. Unwin, *Anal. Chem.* **2001**, 73, 550-557.
[68] J. Abbou, C. Demaille, M. Dret, J. Moiroux, *Anal. Chem.* **2002**, 74, 6355-6363.
[69] A. W. Hassel, M. M. Lohrengel, *Electrochim. Acta* **1997**, 42, 3327-3333.

1.2.1 SECM apparatus

Fig. 1.3 shows the scheme of a typical SECM apparatus. It consists of an electrochemical cell equipped with three electrodes (microelectrode, ME, counter electrode, CE, and reference electrode, RE), a bipotentiostat for controlling the potential (*versus* reference electrode) applied to the microelectrode (working electrode) and/or to the substrate, if it is a conductor, and a micropositioner. The substrate investigated is usually placed on the bottom of the cell and the electrolyte solution contains a so called redox mediator, *i.e.*, an electroactive species of known electrochemistry, whose response at the microelectrode allows characterizing the substrate properties.

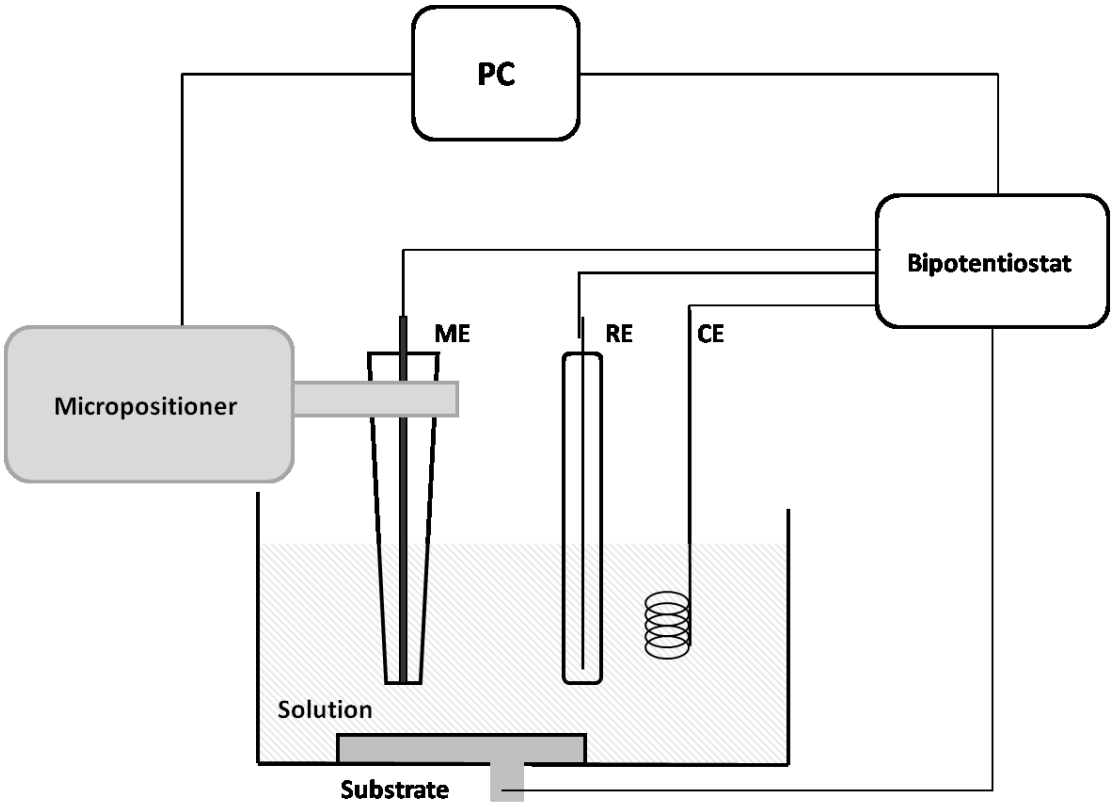

Fig. 1.3: *Scheme of a typical SECM apparatus.*

1.2.2 Modes of operation

There are several operation modes of SECM, and their classification derives from the way the tip is moved/kept above the substrate or on the interaction of the redox mediator with both microelectrode and substrate. In the following, SECM modes employed in the present thesis are briefly illustrated[29].

In the *feedback mode* the microelectrode is moved away or approached perpendicularly to the substrate surface. In this way it is possible to investigate the features of the sample surface by recording the so called approach curves[29].

In the *scanning mode* the microelectrode is placed at a fixed distance above the substrate and it is translated parallel to the surface in a two or one dimension along the surface. The plot of current as a function of the spatial coordinates allows imaging the investigated surface in terms of either topography and/or chemical reactivity.

The *generation/collection mode* can be distinguished in tip generation/substrate collection (TG/SC) and substrate generation/tip collection (SG/TC) modes. In TG/SC mode the tip generates an electroactive species that diffuses across the tip-substrate gap and eventually reacts with the substrate (see Fig. 1.4 A). In the SG/TC mode an electroactive species is generated at the substrate surface and it is collected at the tip[70], Fig. 1.4 B.

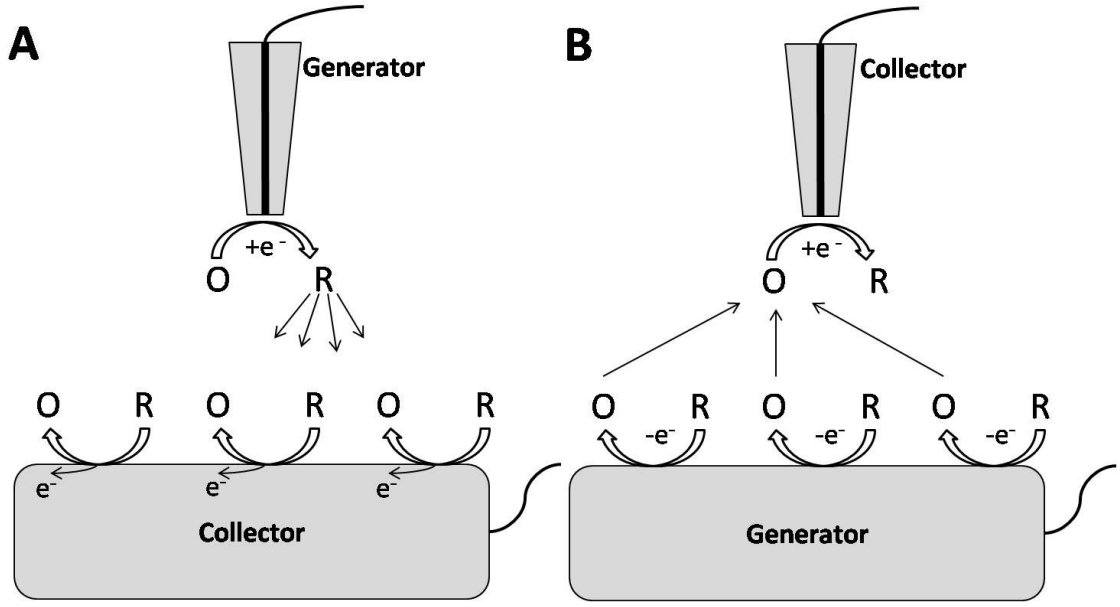

***Fig. 1.4**: Generation Collection mode. A) TG/SC, the species generated at the tip is collected at the substrate. B) SG/TC, the species generated at the substrate is collected at the tip.*

1.3 Microcapillary Techniques

Microcapillary-based techniques have been employed to probe the electrochemistry of small areas of macroscopic surfaces[71,72]. These techniques have allowed individual measurements to be performed at specific surface locations and, initially, have been applied to investigate corrosion or passivation processes on metal surfaces. Innovation of the techniques has led to

[70] P. Sun, F. O. Laforge, M. V. Mirkin, *Phys. Chem. Chem. Phys.* **2007**, 9, 802-823.
[71] C. G. Williams, M. A. Edwards, A. L. Colley, J. V. Macpherson, P. R. Unwin, *Anal. Chem.* **2009**, 81, 2486-2495.
[72] D. Battistel, G. Pecchielan, S. Daniele, *ChemElectroChem.* **2014**, 1, 140-146.

scanning microcapillary techniques, which have allowed high-resolution imaging of conducting surfaces, and microfabrication, to perform micro- and nano-electrochemistry onto a variety of substrates materials[73,20].

Micropipettes and nanopipettes have also been utilized as SECM probes to investigate chemical and redox phenomena occurring at liquid/liquid interfaces of immiscible solvents. With this setup it was possible to probe electron-transfer and ion-transfer processes across the liquid phase boundary. In these experiments, usually, the pipette was filled with an organic solvent immiscible with the outer aqueous solution; the liquid/liquid interface is formed at the tip end. Single-phase experiments, in which the same solvent is used inside and outside the pipette, have been performed in Scanning Ion Conductance Microscopy, (SICM)[74,75]. SICM has nowadays gained significant attention and attraction due to the high-resolution non-contact imaging of biological samples like living cells[21]. By integrating SICM with SECM, it was possible deconvoluting responses related to topography and chemical activity of surfaces[76].

Microcapillary systems and methods

In all microcapillary methods the probe is a laser-pulled pipette (single channel) or a theta pipette (double channel), which is filled with an electrolyte solution; it usually contains a redox mediator, and forms a thin meniscus at the pipette end (see Fig. 1.5 A and B).

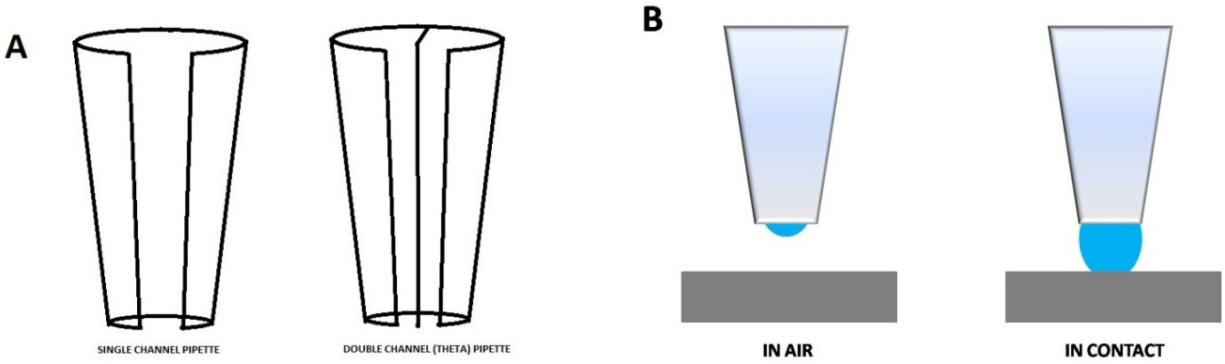

***Fig. 1.5**: A) Scheme of a single channel pipette and double/theta channel pipette. B) Meniscus detail.*

Using a single channel pipette, a two-electrode micro-electrochemical cell is formed; a pseudo-reference/counter (PRCE) electrode is immersed in the solution within the pipette, while the working electrode is made by the small portion of the substrate that comes into contact with the meniscus. The use of a theta pipette allows obtaining more complex cell systems with

[73] P. V. Dudin, P. R. Unwin. J. V. Macpherson, *J. Phys. Chem. C* **2010**, 114, 13241-13248.
[74] P. K. Hansma, B. Drake, O. Marti, S. A. C. Gould, C. B. Prater, *Science* **1989**, 243, 641-643.
[75] P. Novak, C. Li, A. I. Shevchuk, R. Stepanyan, M. Caldwell, S. Hughes, T. G. Smart, J. Gorelik, V. P. Ostanin, M. J. Lab, G. W. J. Moss, G. I. Frolenkov, D. Klenermann, Y. E. Korchev, *Nat. Methods* **2009**, 6, 279-281.
[76] D. J. Comstock, J. W. Elam, M. J. Pellin, M. C. Hersam, *Anal. Chem.* **2010**, 82, 1270-1276.

multifunction properties. Pipette-based electrochemical methods were originally developed for high-resolution corrosion studies, which required to confine measurements to a small area. The scheme of the evolution of the setup for microcapillary techniques is presented in Fig. 1.6. The first setup utilized (Fig. 1.6 A) a single-channel pipette probe with a diameter between 100 and 1000 µm, with the end coated with a thick silicone rubber gasket to prevent (solvent) evaporation and to define the electrode area[77,78,79,80,81]. The pipette was mounted on a micropositioner system, which allowed its easy and precise positioning on the surface. This set-up allowed for the electrochemical interrogation of localized pitting sites on stainless steel[66,67].

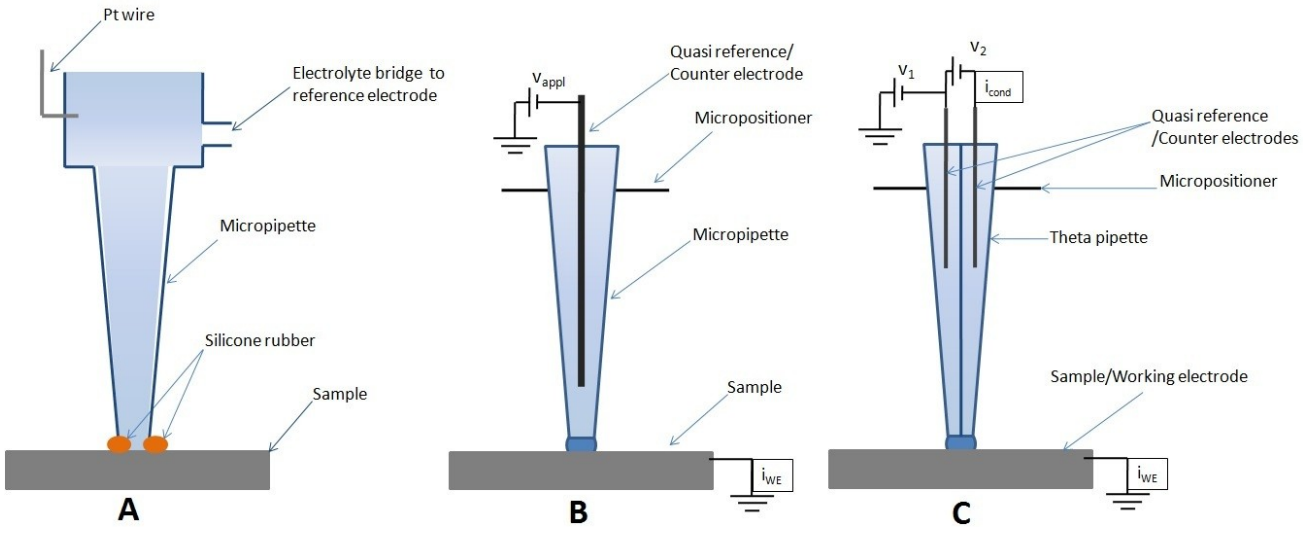

Fig. 1.6*: A) Scheme of the microcapillary technique using a silicone rubber gasket to define the contact area; B) Principle of the scanning microcapillary technique; C) Scheme of scanning electrochemical cell microscopy.*

Subsequently, a flow-through microcell reactor was developed for collecting products of reactions carried out at large current densities for off-line analysis of reactions[82]. For this purpose a dual-channel (theta) capillary, defined by a silicone rubber gasket, was used. The electrolyte flow was achieved via an external pump, and this approach has been used for metal dissolution and corrosion studies[83,84,85].

The microcapillary electrochemical method has been employed for a variety of applications such as to control the microfabrication of crystal of iron hexacyanides[86,87,88], to investigate the

[77] H. Böhni, T. Suter, A. Schreyer, *Electrochim. Acta* **1995**, 40, 1361-1368.
[78] T. Suter, H. Böhni, *Electrochim. Acta* **1997**, 42, 3275-3280.
[79] A. W. Hassel, M. M. Lohrengel, *Electrochim. Acta* **1997**, 42, 3327-3333.
[80] M. M. Lohrengel, A. Moehring, M. Pilaski, *Fresenius' J. Anal. Chem.* **2000**, 367, 334-339.
[81] M. M. Lohrengel, A. Moehring, M. Pilaski, *Electrochim. Acta* **2001**, 47, 137-141.
[82] M. M. Lohrengel, C. Rosenkranz, I Klüppel, A. Moehring, H. Bettermann, B. Van den Bossche, J. Deconink, *Electrochim. Acta* **2004**, 49, 2863-2870.
[83] S. O. Klemm, J.-C. Schauer, B. Schuhmacher, A. W. Hassel, *Electrochim. Acta* **2011**, 56, 9627-9636.
[84] S. O. Klemm, J.-C. Schauer, B. Schuhmacher, A. W. Hassel, *Electrochim. Acta* **2011**, 56, 4315-4321.
[85] S. O. Klemm, S. E. Pust, A. W. Hassel, J. Hüpkes, K. J. J. Mayrhofer, *J. Solid State Electrochem.* **2012**, 16, 283-290.
[86] T. M. Day, P. R. Unwin, J. V. Macppherson, *Nano Lett.* **2006**, 7, 51-57.
[87] P. V. Dudin, M. E. Snowden, J. V. Macpherson, P. R. Unwin, *ACS Nano* **2011**, 5, 10017-10025.

electroactivity of basal plane of highly oriented pyrolitic graphite and aluminum alloy[71], to probe the electrochemistry of individual single-walled carbon nanotubes[87,88], to deposit nanoparticles on nanostructured substrates[89], to explore passive oxide breakdown and pit initiation on Al (111) thin films[90,91], to interrogate single metallurgic sites[92] and to understand the behavior of metallic phases and non-metallic heterogeneities in alloys[93].

An innovation of MC is the Scanning Micropipette Contact Method (SMCM, Fig. 1.6 B), where a moving micropipette is positioned at the sample surface such that the liquid meniscus makes contact. Positioning is achieved by detecting the current flow upon the liquid meniscus comes into contact with the sample surface. An imaging can be constructed by point-to-point measurements, while the pipette is retracted and then re-approached for the next measurements, similar to the *hopping mode operation*[21]. More recently, the basic principle described above was extended to using double-barrel pipettes fabricated from theta capillaries (Fig. 1.6 C)[22]. In contrast to the single barrel approach, a voltage may now be applied between the two reference electrodes, which leads to migration of ions across the meniscus between the two barrels. Again, if the dual-barrel pipette is moved towards the sample surface the meniscus at the end of the barrels initiates a contact, while changes the measured ion current. With this approach multiple and simultaneously information on topography, electroactivity and conductivity can be obtained[22].

The resolution of microcapillary electrochemical methods depends on the size of the pulled pipette, and the meniscus realized on the substrate surface[94]. The contact radius may vary by up to 10-20% of the pipettes radius, according to the local wetting properties of the substrate[22].

[88] D. Yang, L. Han, Y. Yang, L.-B. Zhao, C. Zong, Y.-F. Huang, D. Zhan, Z.-Q. Tian, *Angew. Chem.* **2011**, 123, 8838-8841; D. Zhan, B.-S. Yin, J. Zhang, Z. Q. Tian, *Anal. Chem.* **2012**, 84, 9276-9281.
[89] S. X. Chen, K. Eckhard, M. Zhou, M. Bron, W. Schuhmann, *Anal. Chem.* **2009**, 81, 7597-7603.
[90] K. R. Zavadil, *ECS Transactions* **2012**, 41, 133-142.
[91] V. Vignal, H. Krawiec, O. Heintz, R. Oltra, *Electrochim. Acta* **2007**, 52, 4994-5001.
[92] H. Krawiec, V. Vignal, R. Akid, *Electrochim. Acta* **2008**, 53, 5252-5259.
[93] H. Y. Ha, C. J. Park, H. S. Kwon, *Corrosion Science* **2007**, 49, 1266-1275.
[94] Y. H. Shao, M. V. Mirkin, *Anal. Chem.* **1998**, 70, 3155-3161.

Objectives of the thesis

The aim of the research reported in this thesis was to investigate and develop various strategies based on Scanning Electrochemical Microscopy (SECM), Microcapillary (MC) and Voltammetric techniques, for probing nano-locations and nanomaterials that can find applications in fields such as food industry and sensors. The electrochemical techniques considered have several advantages over others. In particular, both SECM and MC can be used to investigate chemical phenomena taking place at interfaces with high spatial resolution, or to perform local modification of the surface. These characteristics are mandatory for local monitoring of chemical species that are delivered or trapped in a solid matrix in contact with a liquid phase or a solution. Local modification of a surface is of great interest to fabricate individual nanostructures because of their several potential applications in sensor and life science technologies.

Specifically, in this thesis, MC, also in the scanning mode, and SECM are used to propose procedures to fabricate/characterise silver micro- and nano-particles (AgNPs) either synthesised on purpose or present in commercially available consumer goods. New synthetic routes, making use of the MC and meniscus-based methods, or more traditional chemical and electrochemical approaches to produce nanosilver deposits are investigated. One of the main objectives of this project was to investigate the local reactivity of AgNPs embedded in solid or soft matrices. AgNPs are, nowadays, widely employed as antiseptic because of their distinctive physicochemical and biological properties. On the other hand, the large use and, consequently, diffusion of AgNPs in the environment poses problems in terms of toxicity towards human cells, aquatic organisms and more in general, bacterial strains. The toxicity or useful action of AgNPs seems to depend on the amount of free Ag^+ released in the media and its kinetic. Therefore, a topic investigated in the thesis was to establish the redox state of AgNPs prepared in different ways and the correlation with the amount of Ag^+ released at the substrate/solution interface. For the latter studies SECM in combination with voltammetry in the anodic stripping mode, which provides very sensitive responses, was employed.

Another objective of the thesis, undertaken to promote new nanostructured materials in sensor technology, was to investigate the properties of reduced graphene oxide (rGO) prepared by a pressure-wax based transferring technique, to be used as electrode material. Thin layers of GOs deposited as arrays of band electrodes were prepared and investigated by SECM.

Overview of the thesis

Chapter 2 reviews theoretical background of mass transport regimes at microelectrodes of different geometries. Theoretical aspects of the feedback mode of SECM are also given.

Chapter 3 discusses the experimental aspects of the work done. It includes methods of fabrication of microelectrodes and their characterization by voltammetry. The fabrication of the micropipette for the MC experiments and the specific cell used for reproducible measurements are also illustrated. The description of the instruments, preparation of all solutions and standard procedures used are also presented.

Chapters 4, 5 and 6 are devoted to the results and discussion. In particular:

- ***Chapter 4*** is devoted to the characterization of the micropipette used in the microcapillary methods for investigating and patterning with micro and nanosilver deposits either on conducting or non-conducting substrates. Theory, not previously reported, for the mass transport at the meniscus pipette end kept above a recessed conducting substrate is also discussed to rationalize some of the voltammetric responses obtained.
- ***Chapter 5*** is dedicated to a comprehensive investigation of the redox state of Ag in silver particles and the release of Ag^+ from various silver containing substrates, in water or water/ethanol mixtures. These mixtures are used to simulate the behavior of food matrices. The synthesis and SEM images of various micro- and nano-Ag deposits embedded in various polymeric matrices are reported. The study is performed by using SECM and anodic stripping voltammetry (ASV). Results concerning the voltammetric behavior of silver ions in water/ethanol mixtures at a platinum microelectrode, used as SECM tip, are reported.
- ***Chapter 6*** is devoted to the characterization of substrates made of graphene oxides, prepared by a patented procedure, to establish their suitability as voltammetric electrodes in sensor technology. The characterization is performed by SECM in feedback mode.

Chapter 7 summarizes the main conclusions that can be drawn from the preceding chapters and formulates some proposals for future developments/applications of the methodologies/materials employed in the thesis.

Chapter 2: Theory for microelectrodes and Scanning Electrochemical Microscopy

2.1 Microelectrodes

Microelectrodes have, according to IUPAC, at least one dimension called ***critical dimension*** in the range of 10 nm – 25 μm[1,2]. To attain the features which properly characterizes the microelectrode behavior, apart from the electrode size and shape, the characteristic time must be taken into consideration and it depends on the electroanalytical technique employed in the measurements. The latter parameter governs the thickness of the diffusion layer developed around the electrode surface. From this point of view, according to IUPAC, a microelectrode is "any electrode whose characteristic dimension is, under the given experimental conditions, comparable to or smaller than the diffusion layer thickness"[1]. In what follows, the diffusion mass transport that will control the current at microelectrodes of different size and geometries will be described.

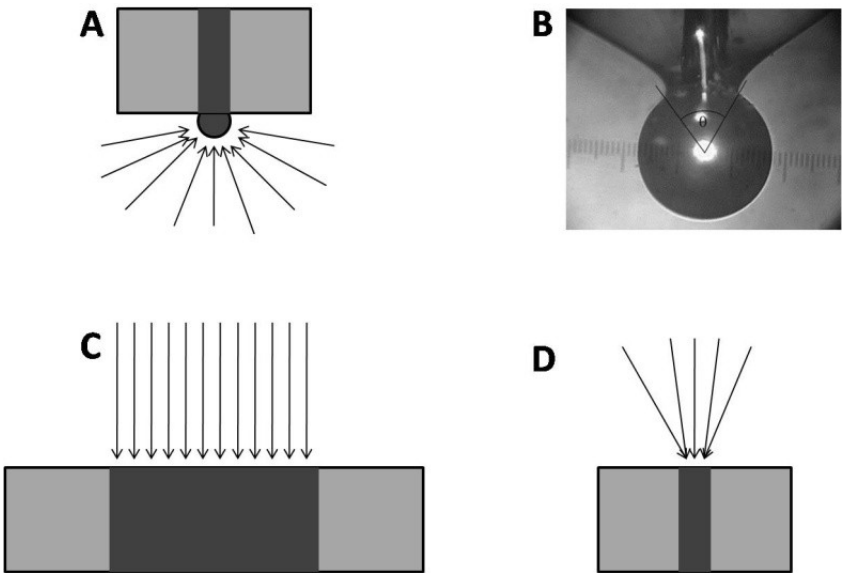

Fig. 2.1*: A) Diffusion fields at microsphere electrode; B) dropping mercury electrode; C) macroelectrode and D) microdisk electrode.*

[1] K. Štulik, C. Amatore, K. Holub, V. Mareček, W. Kutner, *Pure and Applied Chemistry* (Technical Report) **2000**, 72, 1483-1492.

[2] A. J. Bard, L. R. Faulkner, *Electrochemical Methods*, M. Dekker, New York, **2001**.

2.1.1 Mass transport under diffusive conditions

Starting from the random walk theory, it is possible to describe the diffusion by formulating differential equations for flux and concentration of a substance as a function of time and position. The equations that describe these processes are known as Fick's equations. Let *r* denotes the position in the three dimensional space, *t* the time, J(r, t) and C(r, t) are the local flux and concentration of a substance undergoing spatial diffusion, measured in mol/(s cm^2) and mol/cm^3, respectively. Fick's first law establishes that the flux is proportional to the concentration gradient $\boldsymbol{\nabla C(r,t)}$

$$J(r,t) = -D\nabla C(r,t) \tag{2.1}$$

where D is the diffusion coefficient of the chemical species considered. Fick's second law concerns the change of concentration with time:

$$\frac{\partial C(r,t)}{\partial t} = D\nabla^2 C(r,t) \tag{2.2}$$

The form of the Laplacian operator, ∇^2, depends on the electrode geometry.

Fick's second law is used routinely in order to find the electrode current either as a function of time or in steady state for a settled microelectrode geometry. In order to solve this differential equation and to specify this for the system under study (geometry, electroanalytical technique etc.), it is necessary to specify: *i*) initial conditions for every point in space at *t=0* and *ii*) boundary conditions at the physical contour of the system, for any time *t*. The form of the Laplacian and these conditions will be specified for each case separately.

2.1.2 Mass transport to microsphere and spherical electrodes

The microsphere electrode (Fig. 2.1 A) is the simplest case to be treated analytically, and its mathematical solution allows one to explain qualitatively the mass transport properties of microelectrodes. This diffusion problem was solved many years ago because of the importance of spherical electrodes in the classical polarographic experiments with a dropping mercury electrode[3] (Fig. 2.1 B). We consider a potential step experiment at an electrode with the geometry of a sphere of radius r_0, placed in a solution containing the supporting electrolyte and an electroactive species at a concentration c_b(r, t). The experiment involves stepping the potential from an initial value, where no electrode reaction takes place, to one sufficient to completely reduce or oxidise the electroactive species at the electrode surface. The process involves electron transfer across the electrode/solution interface and the rate at which this occurs is described by the heterogeneous

[3] D. MacGillavry, E. K. Rideal, *Trav. Chim. Pays-Bas* **1937**, 56, 1013-1021.

electron transfer rate constant. If this rate constant is large, mass transport will control the current measured. We assume that mass transport occurs via diffusion only, and consequently, Fick's laws govern the system. In this geometry it is natural to use spherical coordinates, so that Fick's second law becomes:

$$\frac{\partial c(r,t)}{\partial t} = D\left[\frac{\partial^2 c(r,t)}{\partial r^2} + \frac{2}{r}\frac{\partial c(r,t)}{\partial r}\right] \tag{2.3}$$

where c(*r*, *t*) is the concentration at the position *r* and time *t*; r denotes the radial distance away from the centre of the electrode. The initial and boundary conditions for this problem are the following:

$$c(r,0) = c_b \qquad (t = 0), \tag{2.4}$$

$$\lim_{r\to\infty} c(r,t) = c_b \qquad (t > 0), \tag{2.5}$$

$$c(r0,t) = 0 \qquad (t > 0). \tag{2.6}$$

where c_b is the bulk concentration of the electroactive species and r_0 is the radius of the spherical electrode.

Initially, the concentration of the electroactive species, c_b, is constant and uniform throughout the cell (Eq. 2.4). As the potential is switched on, the bulk value is assumed to be attained at the far boundaries of the cell (Eq. 2.5), whereas on the electrode surface the concentration is zero at all times (Eq. 2.6), because the species is completely reduced or oxidised. Equation (2.3) can be solved using Laplace transform techniques[2] to give the time evolution of the current, *i(t)*, subject to the boundary conditions just described. The solution provides the following:

$$i(t) = nFADc_b\left(\frac{1}{a} + \frac{1}{\sqrt{\pi Dt}}\right) \tag{2.7}$$

where *n* is the number of electrons transferred in the redox reaction, *F* is Faraday's constant and *A*, given by $4\pi r_0^2$, is the geometrical electrode area. Eq. (2.7) shows that the current response following a potential step contains both time independent and time dependent terms. The differences in the electrochemical responses observed at macroscopic and microscopic electrodes arise because of the relative importance of these terms at conventional electrochemical time scales. It is possible to distinguish two limiting regimes depending on whether the experimental time scale is short or long.

At sufficiently short times, the thickness of the diffusion layer that is depleted of reactant is much smaller than the electrode radius and the spherical electrode appears to be planar to a molecule at the edge of this diffusion layer. Under these conditions, the electrode behaves like a

conventional macroelectrode (Fig. 2.1 C) and mass transport is dominated by linear diffusion to the electrode surface[2]. At these short times, the $t^{-1/2}$ dependence of the second term in Eq. (2.7) makes it significantly larger than the first and the current response induced by the potential step initially decays in time according to the Cottrell equation[2]:

$$i(t) = nFAc_b\sqrt{\frac{D}{\pi t}} \tag{2.8}$$

At long times, the transient contribution given by the second term of Eq. (2.7) has decayed to the point where its contribution to the overall current is negligible. At these long times, the spherical character of the electrode becomes important and the mass transport process is dominated by spherical diffusion.

The current attains a time-independent steady state value given by:

$$i_{ss} = \frac{nFADc_b}{r_0} \tag{2.9}$$

The steady state response is typical of radial diffusion and arises because the electrolysis rate is equal to the rate at which molecules diffuse to the electrode surface.

Since *short* and *long* times are relative terms, it is useful to determine the times over which transient and steady state behaviors will predominate and how this time regime is affected by the electrode radius. This objective can be achieved by considering the ratio of the steady state (Eq. 2.9), to transient current contribution (Eq. 2.8). This analysis gives a dimensionless parameter $\frac{\sqrt{\pi Dt}}{r_0}$ that can be used to calculate a lower time limit at which the steady state contribution will dominate the total current to a specified extent. For instance, the time required for the steady state contribution to be ten times larger than the transient one is 8×10^5 s, taking as a typical value of D 10^{-5} cm^2/s, for an electrode with r_0 = 5 mm (typical of a conventional, *i.e.*, macroelectrode). However, reducing the electrode radius by a factor of a thousand to 5 µm means that a steady-state response can be observed for times longer than 0.8 s. Since the steady-state current becomes more dominant with increasing time, steady state responses are easily observed for microelectrodes in electrochemical experiments run at conventional time scales. It is important to emphasize that there is no theoretical barrier to observing steady-state behavior for any size of electrode. However, for conventional millimetric dimension macro-electrodes, the time taken is too long to be experimentally practical. Moreover, unintentional convection, *e.g.* caused by building vibrations, or natural convection will play an important role in the mass transport process at these long time scales.

A treatment similar to that for the sphere can be used for the case of a hemispherical microelectrode. The only difference in the mathematics relies on the surface area A given by $A = 2\pi r_0^2$. All general equations, results and considerations equally apply.

2.1.3 Mass transport to microdisk electrodes

Fabrication of microelectrodes with disk geometry embedded in an infinite insulating plane (Fig. 2.1 D) is easier to accomplish than forming spherical microelectrodes. Therefore, it is important to have an analytical expression to describe the current at electrodes of this geometry. In this case, the derivation of a rigorous expression to predict the current response is complicated, because the surface is not uniformly accessible (Fig. 2.1 D). In fact, the flux of material reacting at the surface is unequal across the electrode surface[4] because the electrolysis that occurs at the outer circumference of the disk diminishes the flux of the material to the central portion of the disk[5,6].

Early approaches to the mathematics of this problem used either simplifications[7] or digital simulation procedures[8] attempting to get a solution to the chronoamperometry problem analogous to the Eq. (2.7). To a first approximation one might expect the results for a disk to be very similar to those we have already examined for spherical electrodes. In particular, there should be close analogy between the results for a hemisphere and a disk, and this has been shown[9,10]. Thus, for small values of Dt/a^2, where a is the radius of the disk, it would be expected that the Cottrell equation still describes the current as a function of time. For large values of Dt/a^2, a hemispherical diffusion layer can be envisioned over the disk, and steady state behavior would be expected[11].

Saito was the first to give a clear insight into the steady state nature of the current at microdisk electrodes[12]. To solve the problem for a disk, a cylindrical coordinate system was used. The steady state solution has the form similar to that for a spherical electrode and in fact Saito arrived at the correct conclusion that the limiting steady state current for a disk is:

$$i_{ss} = 4nFDc_b a \qquad (2.10)$$

Eq. (2.10) and eq. (2.7), for a hemispherical electrode are identical when $a_{disc} = \frac{\pi}{2} a_{hemisphere}$.[5]

The above relations hold for a potential step experiment. In voltammetry, the potential changes, usually in a linear fashion, up to a given value (in LSV) and eventually it can be reversed and returned linearly to the initial value (in CV). In these techniques, the transition from planar to radial diffusion for a given microelectrode and electrode geometry, is achieved by reducing the scan rate. The faster the transition, the smaller the characteristic length of the microelectrode. Figure

[4] J. Albery, S. Bruckenstein, *J. Electroanal. Chem.* **1983**, 144, 105-112
[5] K. B. Oldham, *J. Electroanal. Chem.* **1981**, 122, 1-17.
[6] J. Newman, *J. Electroanal. Soc.* **1966**, 113, 501-502.
[7] Z. G Soos, P. J. Lingane, *J. Phys. Chem.* **1964**, 68, 3821-3828.
[8] J. B. Flanagam, L. Marcoux, *J. Phys. Chem.* **1973**, 77, 1051-1055.
[9] J. O. Howell, R, M. Wightman, *Anal. Chem.* **1984**, 56, 524-529.
[10] Z. Galus, J. O. Schenk, R. N. Adams, *J. Electroanal. Chem.* **1982**, 135, 1-11.
[11] A. Dayton, J. C. Brown, K. J. Stuttus, R. M. Wightman, *Anal. Chem.* **1980**, 52, 946-950.
[12] Y. Saito, *Rev. Polarogr. Jpn.* **1968**, 15, 177-187.

2.2 shows, for instance, a series of CVs obtained at a microdisk electrode at different scan rates. It is evident that at high *v*, the CV displays the peak-shaped voltammogram as for macroelectrodes; as the scan rate decreases, the CV becomes sigmoidal with the forward and backward curves retracing one another. This is caused by the formation of a stationary diffusion layer that is due to the relatively high diffusion mass transport. The current at the stationary state is essentially independent of scan rate and the diffusion-limited current corresponds to that evaluated by a large potential step experiment described above. Theoretical modeling of the current-potential profiles at microelectrodes is usually difficult, and because of the complexity of the task, numerical solutions or digital simulation procedures have often been used. The only exception is the case of the spherical microelectrodes for which Eq. (2.7) can be applied.

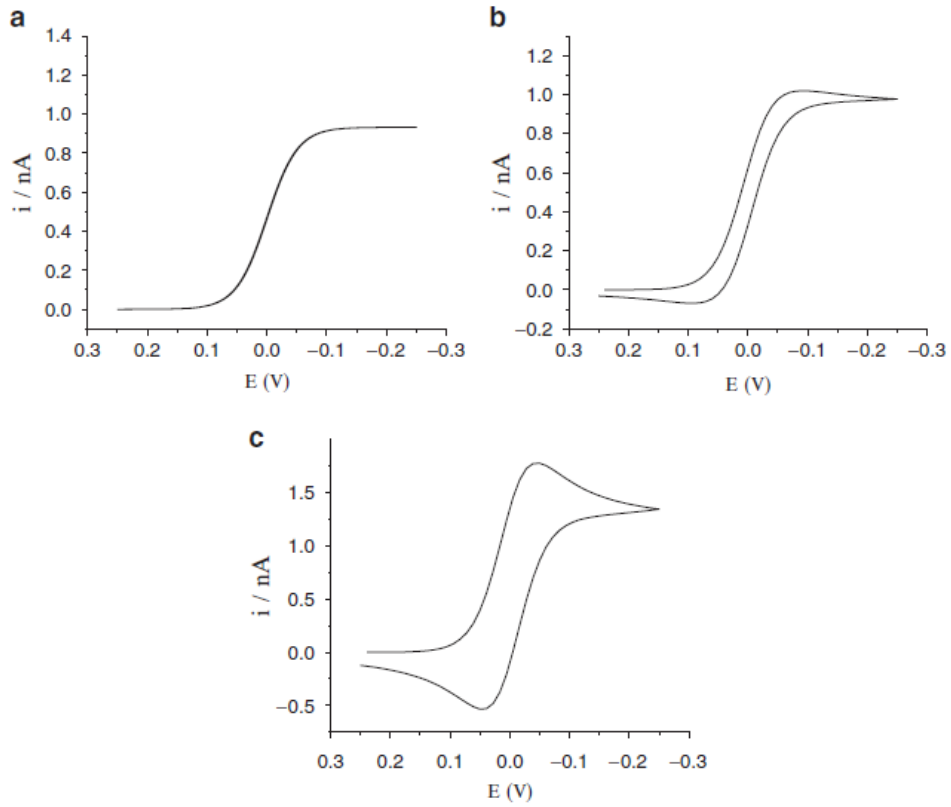

Fig. 2.2*: Simulated CVs for a microdisk 12.5 µm at different scan rates: a) 1 mV/s; b) 200 mV/s; c) 2 V/s.*

For disk and cylinder microelectrode geometries, theoretical expressions of the voltammograms have been derived as a function of the parameter p which contains the characteristic dimension of the specific microelectrode. Since the peak or maximum current characterizes quantitatively the voltammograms, relevant expressions are given and shown in Table 2.1.

***Table 2.1**: Voltammetric peak current for different electrode geometries.*

Electrode geometry	*Peak or maximum current*
Microdisk	$I = 4nFDC\,a[0.34\exp(-0.66p^{d})+0.66-0.13\exp(-11/p^{d})+0.351p^{d}]$
Microcylinder	$I = n^2F^2CAr_0\,v/(RT)\,(0.446/p+0.335/p^{1.85})$
$\boldsymbol{p^{d}}$	$p^{d} = (nFa^2v/RTD)^{1/2}$
$\boldsymbol{p^{1.85}}$	$p^{1.85} = (nF\,r_0\,v/RTD)^{1/2}$

In general, for large values of *p*, the equations shown in Table 2.1 are identical with the equation for planar diffusion. For small values of *p*, the latter equations approach those for the steady-state current displayed in Table 2.1 for the corresponding microelectrode geometry.

2.2 General aspects of SECM feedback mode

In the feedback mode, the microelectrode serves as working electrode in an electrochemical cell containing a solution of the redox mediator (*e.g.*, a reducible species, *O*). The tip is moved in the *z* direction perpendicular to the substrate and its response is recorded as a function of the tip-substrate distance. Suppose that the redox mediator is a reducible species *O*. If a sufficiently negative potential is applied to a microdisk electrode tip of radius *a*, the reduction of *O* occurs at a rate governed by the diffusion of *O* to the microelectrode and the species *R* is generated. When the tip is in the bulk of the solution, *i.e.* positioned far away from the target substrate (usually at a distance $d > 10a$, where *d* is the tip-substrate distance, as shown in Fig. 2.3 A), it behaves as a conventional microelectrode.

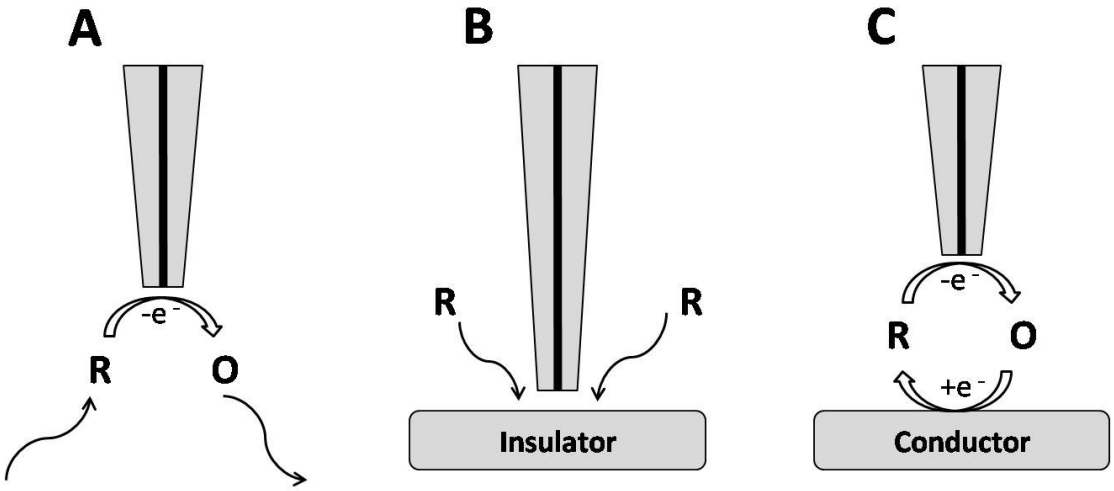

***Fig. 2.3**: Feedback mode: A) the tip is in the bulk of the solution containing the redox mediator; B) Negative feedback; C) Positive feedback.*

In this situation, a steady-state current, i_{ss}, is rapidly established due to hemispherical diffusion of the target species, *O*. As the tip is brought close to the substrate, it is possible to distinguish between two feedback effects, depending on the nature of the substrate itself. If the substrate is inert with respect to species involved in the electrode process, diffusion to the microelectrode becomes hindered (Fig. 2.3 B), and the steady-state current, *i*, decreases compared to i_{ss}. Indeed, the closer the tip to the substrate, the smaller will be *i*. This effect is called *negative feedback*. When the tip gets close to a conductive substrate, the *R* species diffuses to the substrate where it may be oxidised back to *O* (Fig. 2.3 C) by an electrochemical, chemical or enzymatic reaction. This process produces an additional flux of *O* to the tip and hence the tip current increases compared to i_{ss}. The smaller the tip-substrate distance, the larger is *i*. In fact, when the electrode process is rapid, $i \to \infty$ as $d \to 0$. This phenomenon is termed *positive feedback*.

Approach Curves

The feedback effects are, in general, visualized by plots of the normalized current i/i_{ss} as a function of the normalized tip-substrate distance *d/a*. These plots are called *approach curves* and allows the identification of the microelectrode position with respect to the sample surface under investigation. Theoretical approach curves have been derived for several electrode geometry.

To derive the normalized steady-state tip current, also known as *i(L)*, for disk shaped microelectrodes, as a function of normalized tip-substrate distance, *L= d/a*, numerical approaches have been employed[13]. In particular, digital simulation procedures have been considered. From these methods, approximate analytical equations were derived, which are simpler to use from a practical point of view[14].

For a microdisk, Equations (2.12) describes the negative feedback approach curves:

$$i(L) = \frac{i}{i_\infty} = \frac{1}{K_1^N + K_2^N / L + K_3^N \exp\left(K_4^N / L\right)} \qquad (2.12)$$

where K_1^N, K_2^N, K_3^N and K_4^N are constants depending on the *RG* parameter as reported in Table 2.2. The *RG* parameter is defined as the ratio between the overall tip radius to the electrode radius. The resulting approach curves have the shape shown in Fig. 2.4.

[13] A. J. Bard, F. R. F. Fan, M. V. Mirkin, *Scanning Electrochemical Microscopy*, Electroanalytical Chemistry Vol. 18, M. Dekker, **1994**.
[14] M. V. Mirkin, F. R. F. Fan, A. J. Bard, *J. Electroanal. Chem.* **1992**, 328, 47-62

***Table 2.2**: K_1^N, K_2^N, K_3^N and K_4^N values for negative feedback approach curves as a function of RG.*

RG	K_1^N	K_2^N	K_3^N	K_4^N
1002	0.132	3.371	0.821	-2.347
100	0.279	3.054	0.686	-2.759
50.9	0.305	2.62	0.667	-2.669
20.1	0.355	2.025	0.628	-2.556
15.2	0.373	1.851	0.613	-2.495
10.2	0.404	1.601	0.588	-2.372
8.13	0.426	1.46	0.568	-2.285
5.09	0.486	1.177	0.512	-2.078
3.04	0.604	0.86	0.395	-1.894
2.03	0.761	0.609	0.238	-2.032

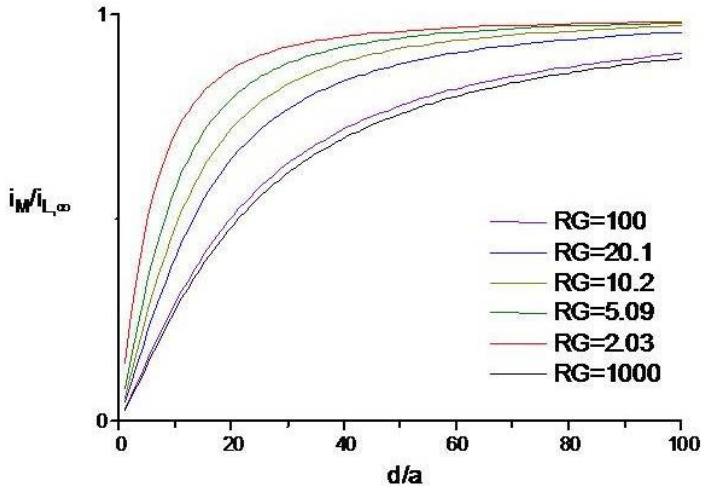

***Fig. 2.4**: Theoretical approach curves in negative feedback conditions obtained for different RG values.*

From the curves reported in Fig. 2.4 it can be observed that for large *L* values (*i.e.*, long distances microelectrode/substrate), *RG* has no influence; this is evident from the relatively low slope of the curves for a certain *L* value. For small *L* values, the slope is affected by *RG* and, in particular, it becomes higher as *RG* decreases. This indicates a higher sensitivity of the probe in the z direction.

For a microdisk, Equations (2.13) describes the positive feedback approach curves:

$$i(L) = K_1^P + \frac{K_2^P}{L} + K_3^P \exp\left(-K_4^P / L\right) \qquad (2.13)$$

where K_1^P, K_2^P, K_3^P and K_4^P are constants depending on *RG*, as illustrated in Table 2.3. The resulting approach curves have the shape shown in Fig. 2.5.

***Table 2.3**: K_1^P, K_2^P, K_3^P, K_4^P values for positive feedback approach curves as a function of RG.*

RG	K_1^N	K_2^N	K_3^N	K_4^N
1002	0.7314	0.77957	0.26298	-1.2907
10.2	0.72627	0.76651	0.26015	-1.41332
5.1	0.72035	0.75128	0.26651	-1.62091
1.51	0.63349	0.67476	0.36509	-1.42897

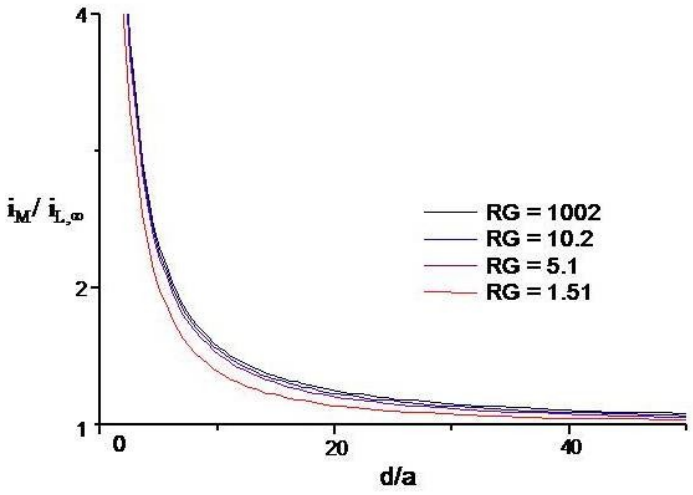

***Fig. 2.5**: Theoretical approach curves in positive feedback conditions obtained for different RG values.*

As is evident, in this case, *RG* is relatively unimportant in determining the shape of the approach curve. In fact, either for large or small *L* values, the response of the working electrode is, respectively, little or much influenced by the presence of the substrate, regardless of the *RG* value. The approach curves are extremely useful from a practical point of view as to each value of normalized current is associable with a distance electrode/substrate[15,16]. Therefore knowing the experimental current and the radius of the electrode it is possible to determine the distance electrode/substrate by graphic interpolation or employing the Equations (2.12) and (2.13).

[15] I. Ciani, S. Daniele, *Anal. Chem.* **2004**, 76, 6575-6581.
[16] S. Daniele, I. Ciani, D. Battistel, *Anal. Chem.* **2008**, 80, 253-259.

Chapter 3: Experimental

3.1 Chemicals

Potassium chloride (KCl), potassium nitrate (KNO_3), sodium carbonate (Na_2CO_3), hexaammine ruthenium (III) chloride (Ru $(NH_3)_6Cl_3$), potassium hexachloroiridate (III) (K_3IrCl_6), formaldehyde, ethanol and Nafion® 117 solution ≈5% w/v were from Sigma-Aldrich (Milan, Italy). Methanol were from Suprasolv (Merck Millipore, Darmstadt, Germany). Glacial acetic acid (CH_3COOH) was from Rudipont (Eurobase SpA, S. Giuliano Milanese, Italy). Sulfuric acid (H_2SO_4) was from Carlo Erba (Cornaredo, Italy), sodium acetate (CH_3COONa) and silver nitrate ($AgNO_3$) 0.1 N standard solution were from Vetrotecnica s.r.l. (Padua, Italy). All reagents employed were of analytical grade and were used as received without any further purification.

All the aqueous solutions were prepared with deionised water purified via Milli-Q unit (Millipore System, Darmstadt, Germany).

3.2 Electrochemical apparatus

Microelectrodes characterization and preliminary voltammetric measurements were performed by using a CHI 760B workstation (CH Instruments Inc., Austin, Texas, U.S.A.) controlled with a personal computer via the CHI760b software.

The SECM apparatus was a CHI920C Scanning Electrochemical Microscope (CH Instruments Inc., Austin, Texas, U.S.A.) consisting in a digital function generator, a bipotentiostat, a high resolution data acquisition circuitry, a three dimensional positioner and a sample/cell holder. The positioner system consisted in a stepper motor combined with a three dimensional closed-loop piezo positioned having the characteristics summarized in Table 3.1:

Tab. 3.1*: Micropositioner specifications.*

Parameter	***Value***
Piezo positional resolution	1.6 nm
Stepper motor resolution	4 nm
X, Y, Z total distance	50 mm

Unless otherwise stated, the electrochemical experiments were carried out in a two-electrode configuration. The SECM electrode tip was a platinum microdisk, while the

reference/counter electrodes employed were either a platinum coil or an Ag/AgCl (KCl saturated) depending on the specific application.

To avoid external interferences, the electrochemical cell or the SECM apparatus was maintained in Faraday Cage made of aluminum.

3.3 Microelectrodes fabrication and characterization

Platinum microdisk electrodes were prepared by sealing platinum wires of 25 µm in diameter (Goodfellow, Cambridge, England) within glass capillaries by the use of a P-2000 Laser Puller (Sutter Instrument, Novato, CA, U.S.A). About 1.5 cm of a platinum wire was inserted inside a borosilicate glass capillary, of 0.58 mm (i.d.), 1.0 mm (o.d.) and 10 cm length. The capillary was fixed by the clamps to the laser puller. The protocol for microelectrode fabrication foresee a 40 s heating step (by a CO_2 laser) and a 20 s relaxing step. The parameters set for sealing the platinum wire were summarized in Tab. 3.2.

***Tab. 3.2**: Laser puller parameter for sealing platinum wires.*

Parameter	*Heat*	*Filament*	*Velocity*	*Delay*	*Pull*
Value	360	5	20	128	0

Heat represents the power of the laser and consequently the amount of energy supplied to the glass; *filament* specifies the scanning pattern of the laser beam (filament = 2 corresponds to 1.9 mm scan length[1]); *velocity* controls the moment when the glass softens and begins to pull apart under a constant load; *pull* controls the force of the hard pull and the higher the pull, the smaller the pipette tip diameter and the longer the taper; *delay* controls the time between the *heat* is turned off and the hard *pull* is activated.

In order to avoid the formation of bubbles, the two ends of the capillary were connected to a vacuum pump, for the entire length of the sealing procedure. The capillary tube, within the melting zone, was cut by a small circular saw, thus obtaining two tips containing the electrode material. The sealing quality and the continuity of the wire were checked by an optical microscope. The electric contact between the platinum fiber and the external circuit was realized with a copper wire soldered by means of indium flakes.

The active surface of the microelectrodes was exposed mechanically by using emery paper (Buehler, Illinois, U.S.A.) of decreasing grain size and alumina suspensions in water from 1 down to 0.05 µm. The microelectrodes were afterward characterized by cyclic voltammetry (CV) at low scan

[1] P-2000 Laser Puller Guide, Sutter Instruments.

rates and SECM to evaluate the actual radius of the microelectrodes and the overall tip radius to the electrode radius ratio, RG, respectively, as described below.

Determination of the radius and the RG parameter of the microdisk electrodes

The radius of the platinum microdisk electrodes was determined by recording the steady-state limiting current in water solutions containing 1 mM $Ru(NH_3)_6Cl_3$ + 0.1 M KCl or 1 mM K_3IrCl_6 + 0.1 M KNO_3 and using Eq. (2.10). The steady-state limiting current was obtained from cyclic voltammetry at low scan rates, which provided voltammetric pictures as those displayed in Fig. 3.1 for the two redox probes employed.

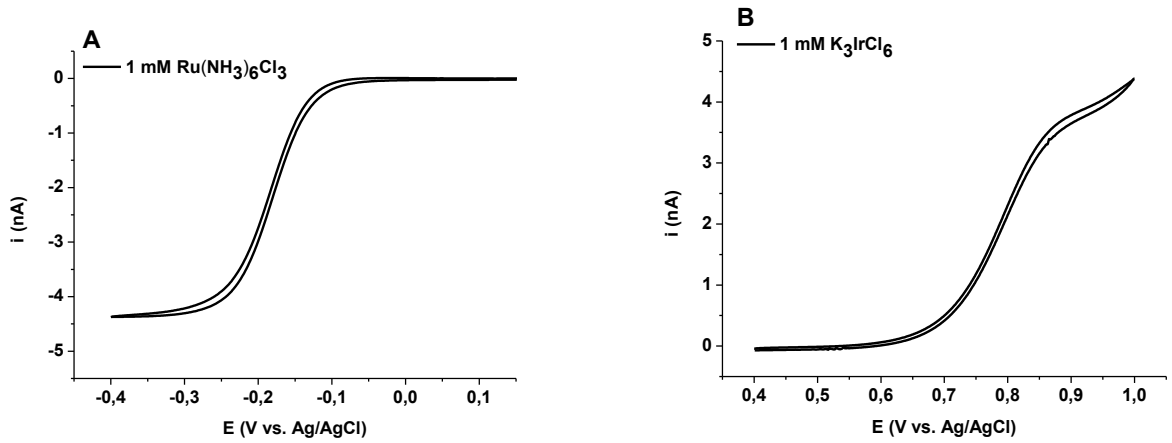

***Fig. 3.1**: Cyclic voltammograms recorded in A) 1 mM $Ru(NH_3)_6Cl_3$ + 0.1 M KCl and B) 1 mM K_3IrCl_6 + 0.1 M KNO_3 at 10 mV/s for a laser pulled Pt microdisk electrode.*

The parameter RG of the SECM tips was evaluated by fitting experimental and theoretical approach curves obtained above either with an insulating (glass substrate) or a conducting (platinum macro disk electrode of 3 mm in diameter) substrate and using $Ru(NH_3)_6Cl_3$ or K_3IrCl_6 as redox mediators. Figure 3.2 compares typical experimental approach curves with theoretical responses obtained with a platinum microdisk of 12.5 µm in radius in 1 mM $Ru(NH_3)_6Cl_3$ solution. The SECM tips used in this thesis were characterized by RG values varying between 8 and 10.

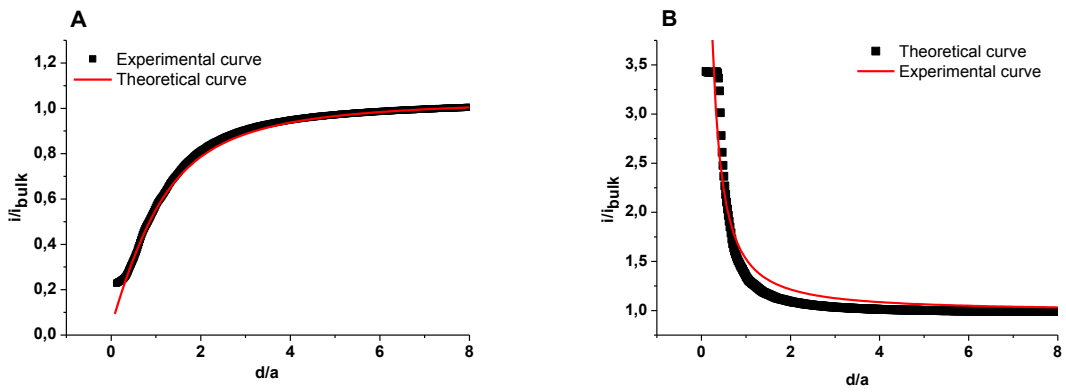

***Fig. 3.2**: Experimental approach curves – A) negative feedback and B) positive feedback – compared with the corresponding theoretical curve for a microdisk electrode having RG = 8. Redox mediator 1 mM $Ru(NH_3)_6Cl_3$ + 0.1 M KCl.*

3.4 Micropipettes fabrication

Micropipettes were pulled from borosilicate capillaries (Sutter) having 1.0 mm (o.d.), 0.58 mm (i.d.) and 150 mm length using the P-2000 Laser Puller system (Sutter Instruments, Novato, U.S.A.). A typical pulling program used in the present work was: *HEAT* = 320, *FILAMENT* = 2, *VELOCITY* = 15, *DELAY* = 128, *PULL* = 100.

After fabrication the pipette was polished flat to reveal openings varying between 40 and 100 µm. Their size were evaluated accurately by scanning electron microscopy. The size of the meniscus generated at the pipette ends were evaluated by cyclic voltammetry (*vide infra*).

3.5 Electrochemical cell for microcapillary experiments

For the microcapillary experiments, the sample and the micropipette were mounted in a home-made cell as that displayed in Fig. 3.3. The cell was sealed to maintain into the chamber a sufficient level of humidity to prevent solvent evaporation from the thin pipette meniscus. The cell was also equipped with a humidity and temperature sensor to supervise the experimental conditions. A constant flux of humidified nitrogen was injected in the cell to avoid interfering processes due to oxygen, while maintaining the desired humidity level.

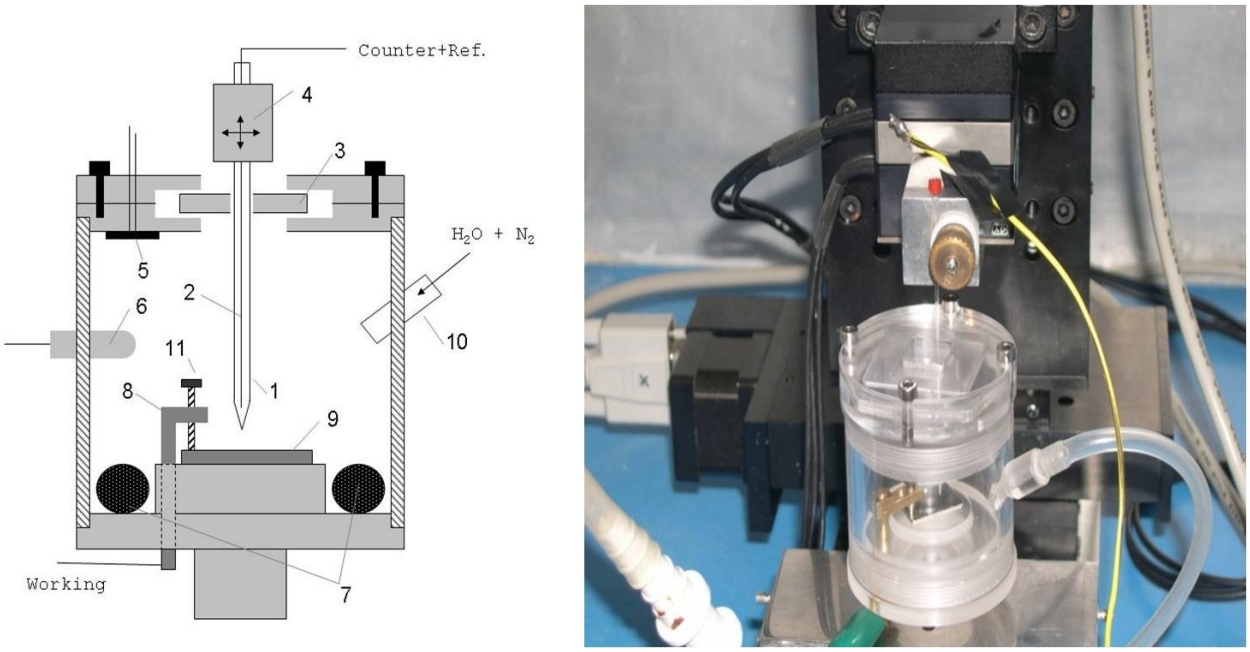

***Fig. 3.3**: Microcapillary cell designed for micropipette experiments in temperature and humidity controlled conditions. 1) Micropipette filled with electrolyte solution; 2) Pt wire (Counter/Quasi reference electrode); 3) Mobile plate handling; 4) SECM micropositioning device; 5) Humidity sensor; 6) Temperature control; 7) water-embedded sponge; 8) External electrical connection; 9) Sample under study; 10) air humidified injector; 11) connection screw.*

The microcapillary, filled with a solution containing a redox mediator and fitted with a reference (or pseudo-reference) electrode, was approached towards the studied substrate surface by a micropositioner. The capillary motion and the meniscus landing were monitored by using an optical microscope. The size of the contact meniscus was evaluated by cyclic voltammetry.

3.6 Non electrochemical apparatus

A M3 WILD Heerbrugg (Heerbrugg, Switzerland) optical microscope was employed to control and check the quality of the samples used in this thesis.

Scanning electron microscopy (SEM) and energy dispersive spectroscopy (EDS) analysis were performed using a TM3000 Hitachi tabletop scanning electron microscope coupled with a X-ray microanalysis system (Nanovision s.r.l., Brugherio, Italy).

Results and Discussion

Chapter 4: Use of micropipette for surface characterization and patterning

The first part of this chapter deals with the characterization of micropipettes to be employed in microcapillary methods. The micropipettes were employed for the local characterization of conducting and non conducting substrates, such as thin platinum film or thin platinum film coated with a thin alumina layer, and for patterning the same substrates with nano-silver.

Cyclic voltammetry is typically employed to characterise the contact meniscuses and the substrates which form the microcells. The voltammetric responses depend on the size of the contact meniscus and on the scan rate employed in the measurements. Steady-state, transient and mixed behaviours can be recorded due to the interplay between linear diffusion that usually applies within the microcapillary and the convergent diffusion that may occur at the substrate wet by the pipette meniscus. This situation can further be complicated when the active surface area of the substrate lies within a recess. In this case, depending on the size of the depth of the recess, linear, convergent diffusion (or mixed conditions) can apply. The above situations are encountered in the various samples investigated. Therefore, in this chapter, in order to better rationalise experimental results, a theoretical investigation is also presented. In particular, the voltammetric behaviour of microcapillaries wetting either flat or recessed substrates is examined. The effect of the pore size, depth of the recess and scan rate of the CVs are investigated in detail. The theoretical behaviour is also fitted to experimental voltammograms obtained for nano- and micro-pores fabricated by the use of a layer of insulating alumina coating a thin film of platinum.

4.1 Simulation

Cyclic voltammograms were simulated considering the following simple one-electron Nernstian electron transfer reaction (1):

$$Ru(NH_3)_6^{3+} + e \rightleftarrows Ru(NH_3)_6^{2+} \quad (1)$$

Simulations were performed in 2D or in 3D cylindrical coordinate systems for symmetric or not-symmetric situations, respectively (see later on). For symmetric models, the diffusion of the redox species in a quiescent solution is expressed as the time-dependent diffusion equation:

$$\frac{\partial c(r,z,t)}{\partial t} = D\left(\frac{\partial^2 c(r,z,t)}{\partial r^2} + \frac{1}{r}\frac{\partial c(r,z,t)}{\partial r} + \frac{\partial^2 c(r,z,t)}{\partial z^2}\right) \quad (4.1)$$

where $c(r,z,t)$ is the concentration of $Ru(NH_3)_6^{3+}$, r and z are the radial and axial coordinates, respectively, and D is the diffusion coefficient shared by both forms of the redox couple considered. For the $Ru(NH_3)_6^{3+/2+}$ system a value of 7×10^{-6} cm^2/s was reported in the literature (*vide infra*).

In 3D simulations the equation employed was in the form:

$$\frac{\partial c(x,y,z,t)}{\partial t} = D\left(\frac{\partial^2 c(x,y,z,t)}{\partial x^2} + \frac{\partial^2 c(x,y,z,t)}{\partial y^2} + \frac{\partial^2 c(x,y,z,t)}{\partial z^2}\right) \qquad (4.2)$$

where x, y, z are the spatial coordinates.

In Fig. 4.1 A, a schematic representation of the simulation domain for a symmetric model is reported. The micropipette semiangle α was taken equal to 10° and the radius of the micropipette (r_p) was 50 µm, as measured by SEM images. L and a are the depth and the radius of the disk shaped pore, respectively, and h is the height of the pipette filled with the electrolyte. The boundary conditions for the simulations are listed below:

Axis of symmetry	$0 < z < -L + h$; $r=0$	$\nabla c \cdot \mathbf{n}=0$
Bulk solution	$0 < r < d$; $z=h$	$c=c_b$
Micropipette wall	$r=z\mathrm{tg}\alpha + r_p$; $0 < z < h$	$\nabla c \cdot \mathbf{n}=0$
Insulating substrate	$z=0$; $a < r < r_p$	$\nabla c \cdot \mathbf{n}=0$
Insulator wall	$-L < z < 0$; $r=a$	$\nabla c \cdot \mathbf{n}=0$
Active surface	$z=-L$; $0 < r < a$	$c = \frac{c_b}{1+\theta}$

where c^b is the bulk concentration and $\theta = \exp\left(-\eta \frac{nF}{RT}\right)$.

In the 3D model (see Figure 4.1B), the center-to-center distance between the micropipette and the pore, is taken into account by the parameter b.

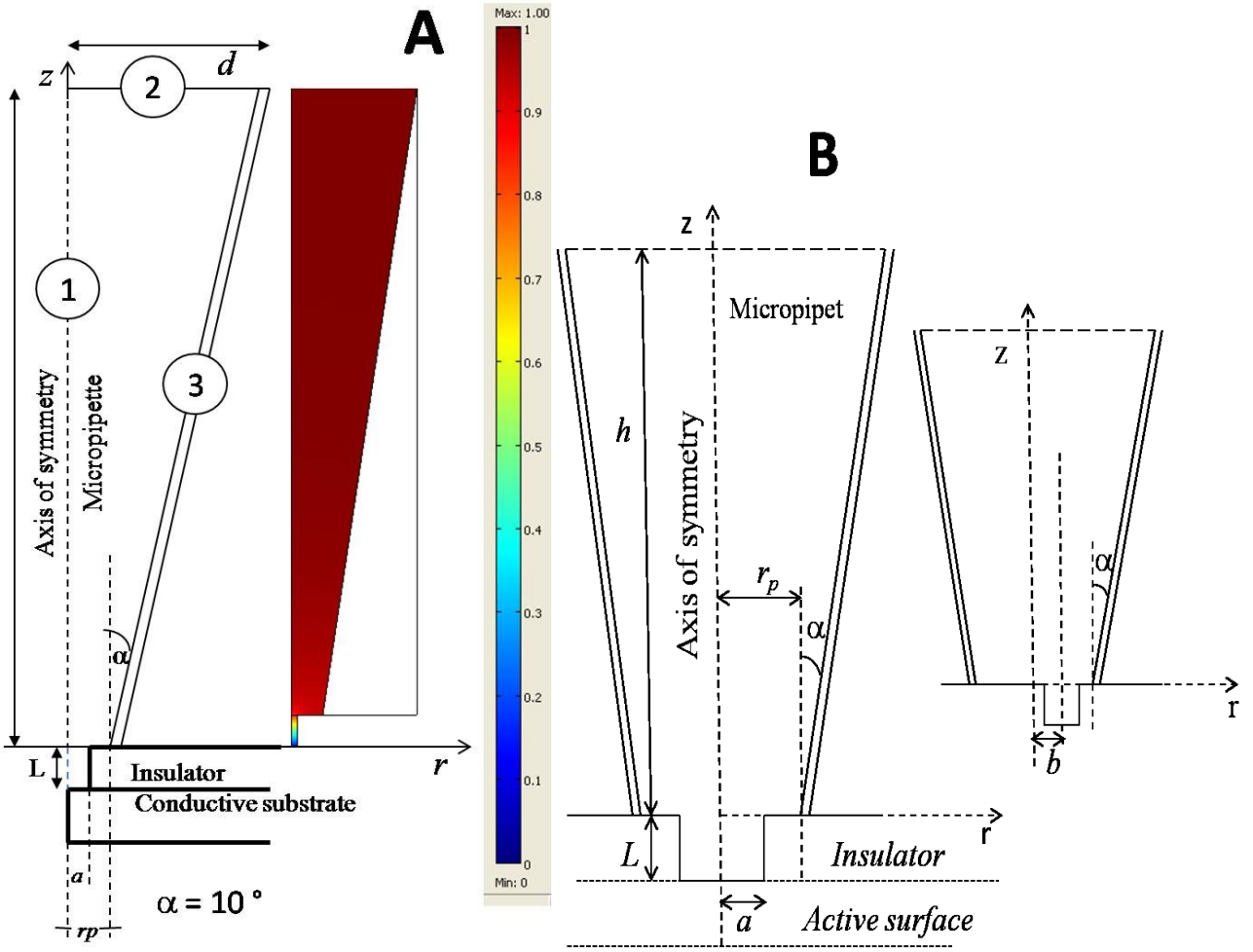

***Fig. 4.1**: Scheme of the simulation domain of the micropipette and the meniscus landing.*

Simulations were performed by using the commercially available program COMSOL Multiphysics 3.4. In these simulations, the height of the liquid meniscus is neglected; indeed the size of the meniscus is very small in comparison with the micropipette radius. Thus, the voltammetric response is not affected by the meniscus, as reported in preliminary simulations[1].

4.1.1 Simulations for not-recessed substrates (*L*=0)

Firstly, a not-recessed (*L*=0) and centred (*b*=0) pore is considered. Thus, the symmetry of the system suggests to employ the symmetric model. The size of the radius (*a*) of the not-recessed active surface area wetted by the solution was changed between 0.5 and 50 µm. For comparison, simulations were also performed to obtain CVs for a disk microelectrode of radius *a* embedded on

[1] C. G. Williams, M. A. Edwards, A. L. Colley, J. V. Macpherson, P. R. Unwin, *Anal. Chem.* **2009**, 81, 2486-2495.

an infinite insulating plane in a semi-infinite solution. These sets of simulations were carried out at a scan rate of 1 mV/s.

Fig. 4.2 compares theoretical CVs obtained for the micropipette (black line) and the microdisk electrode (red line) with identical active surface area and for a range of radii.

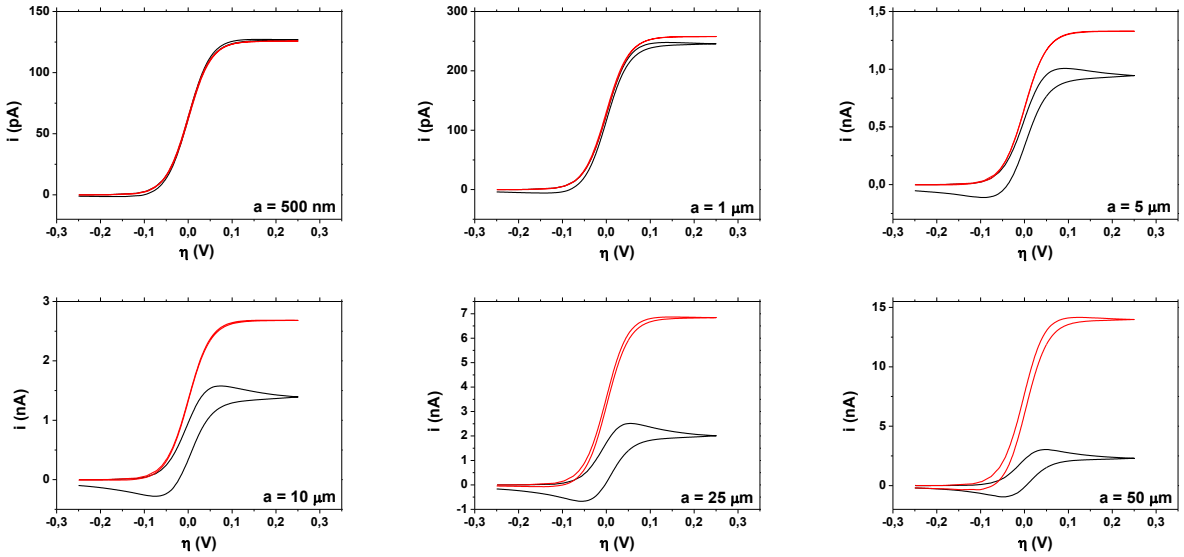

Fig. 4.2*: Simulated CVs for a circular substrate of radius as indicated in the figure, obtained by wetting a conducting substrate with a micropipette meniscus (black line) and for a microdisk electrode in a bulk solution (red line). Scan rate 1 mV/s.*

As is evident, for small active area (*i.e.*, circles with a = 500 nm) the voltammetric responses for both types of electrodes are sigmoidal and the waves fully overlap. A pure radial diffusion regime is therefore operative, which leads to a steady-state limiting current. As the radius of the circular surface increases, an essentially steady state voltammogram is obtained at the microdisk, regardless the electrode radius; a transition from pure radial to planar diffusion is instead observed at the pipette meniscus. For a circular area of radius of 50 µm, fully planar diffusion occurs. This was verified by performing a set of simulations at different scan rates (Fig. 4.3 A). From this figure it is evident that peak shaped CVs are in any case obtained and the forward peak current (i_p) increases as the scan rate becomes larger. The analysis of the i_p *vs.* $v^{1/2}$ gives a linear relation (R^2 = 0.9999) (Fig. 4.3 B), congruent with the Randles-Sevcik equation that holds for planar diffusion of reversible electrode processes[2]:

$$i_p = 2.69 \times 10^5 \, n^{3/2} \, A \, c_b \, D^{1/2} \, v^{1/2} \qquad (4.3)$$

[2] A. J. Bard, L. R. Faulkner, *Electrochemical Methods*, M. Dekker, New York, **2001**.

where *n* is the number of electrons, *A* is the geometrical surface area, c_b and *D* are, respectively, the bulk concentration and the diffusion coefficient ($7x10^{-6}$ cm^2/s)[3] of the redox species, *v* is the scan rate.

Comparison between simulated and calculated by (Eq. 4.3) peak currents agree within 0.34%.

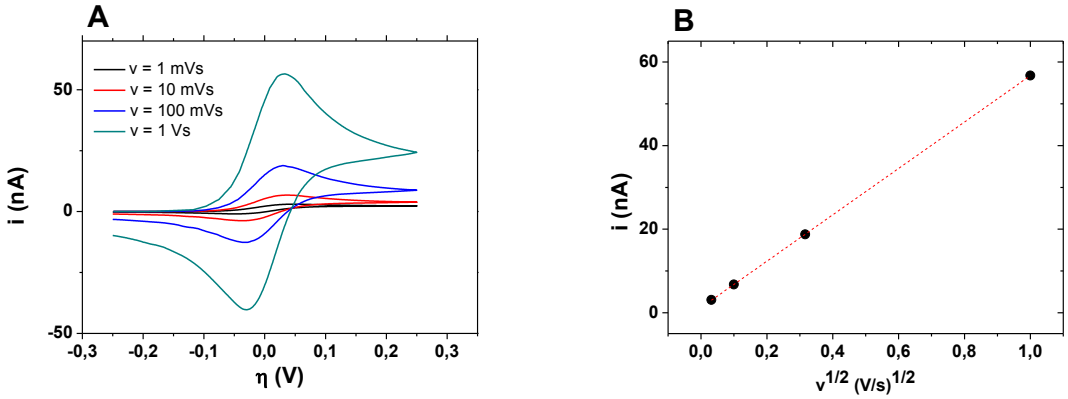

Figure 4.3: *A) Simulated CVs for a circular meniscus of radius 50 µm. B) Forward peak current against square root of scan rate.*

As will be shown below, results similar to those reported in Fig. 4.3 were obtained experimentally.

4.1.2 Simulations for recessed substrates

A set of simulations in symmetric cylindrical coordinates were performed for *a* = 500 nm and varying the depth of the pore (*L*) from 0 to 100 µm (see Fig. 4.4). The simulations were performed at the scan rates of 1 mV/s (black line) and 100 mV/s (red line). As is evident, at the low scan rate, an essentially sigmoidal wave, typical for the achievement of steady state conditions, is obtained, regardless the depth of the recess. At the higher scan rate, essentially, sigmoidal waves are obtained, provided that the recess depth does not exceed 10 µm. For deeper holes a transition from convergent to planar diffusion occurs.

[3] D. Battistel, S. Daniele, G. Battaglin, M. A. Baldo, *Electrochem. Commun.* **2009**, 11, 2195-2198.

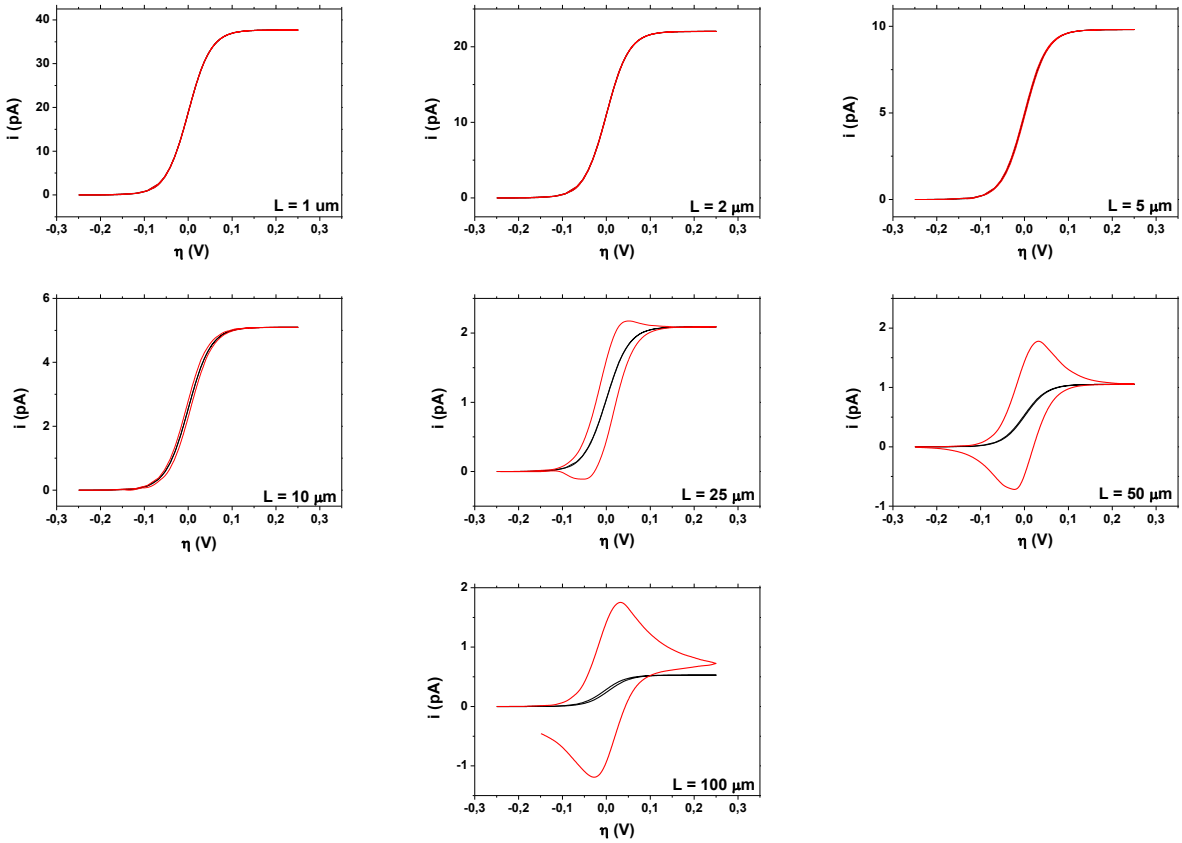

***Fig. 4.4**: Simulated CVs recorded for circular meniscus having a = 500 nm and L as indicated at 1 mV/s (black line) and 100 mV/s (red line).*

The model of recessed microelectrodes, for which the following analytical equation applies[4],

$$i_{ss} = \frac{4n\pi Fc_b Da^2}{4L + \pi a} \tag{4.4}$$

was used to ascertain the validity of the simulation model adopted for recessed substrates wet by the pipette meniscus. In Eq. 4.4 i_{ss} is the steady-state diffusion limiting current, while the other symbols have their usual meaning. Also for these cases, simulated and calculated currents agreed within 0.45%.

4.1.3 Not-centred pores (*b*>0)

The situations discussed above are not easy to realize from an experimental point of view. In fact, more likely, the pore is placed randomly and not-symmetrical within the surface wet by the micropipette. This condition can be simulated by using the coordinates for the not-symmetric

[4] A. M. Bond, D. Luscombe, K. B. Oldham, C. G. Zoski, *J. Electroanal. Chem.* **1988**, 249, 1-14.

model. Apart from geometrical complications, the boundary conditions are the same discussed above. In order to verify the validity of the 3D model, a simulation was performed by using *L*=0, while *b* was varied from 0 to 49 µm. Pore size of 0.5 and 1 µm radius and scan rates of 1 mV/s and 100 mV/s were considered.

CVs simulated at different *b* values for *L*=0 (not-recessed) are reported for *v*=1 mV/s (Fig. 4.5 A) and *v*=100 mV/s (Fig. 4.5 B). For the case *L*=0 and *b*=0, CVs obtained by the 2D and 3D models completely overlapped, indicating the validity of the 3D model adopted. In other cases, as is evident from Fig. 4.5, the limiting current decreased when the mouth of the pore was located towards the edge of the micropipette. However, the change on the limiting current was, in general, negligible even for *b*=10 µm (*i.e.*, within 3%), as is also displayed in Fig. 4.6. In the latter figure the current is normalized by the value of the limiting current simulated in bulk conditions. When the centre of the pore is 1 µm away from the edge of the pipette meniscus, a decrease of the current of about 15% is observed.

The simulations performed with for recessed substrates (*L*=25 µm), reported in Fig. 4.5 C-D, indicate that no significant variations of the current are observed, whatever is the *b* value (Figure 4.6, empty symbols).

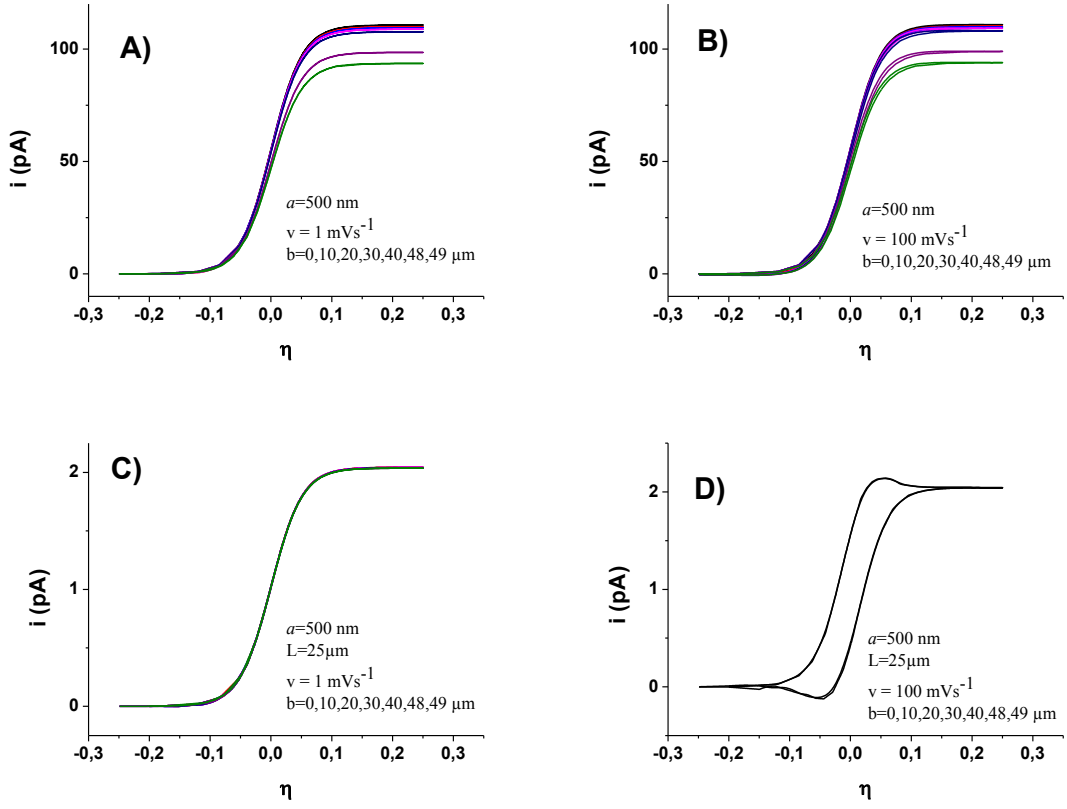

Fig. 4.5: *Simulated CVs recorded for different b values for L = 0 at A) 1 mV/s and B) 100 mV/s and for a recessed pore at C) 1 mV/s and D) 100 mV/s.*

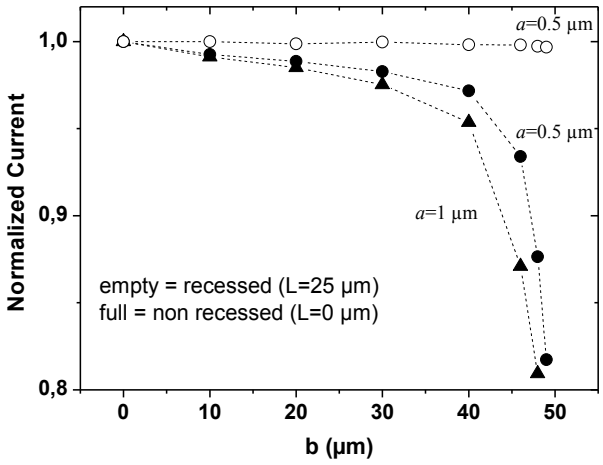

Figure 4.6: *Effect of b on the normalized current.*

4.2 Experimental microcapillary voltammetry at a platinum substrate

The micropipettes prepared following the procedures reported in paragraph 3.4, were characterised by scanning electron microscopy (SEM) and cyclic voltammetry (CV) to obtain information on the size of the contact meniscus. Fig. 4.7 shows a SEM image of a flat polished tip end of a clean micropipette used. For the specific case, the opening diameter was evaluated to be 45± 2 µm.

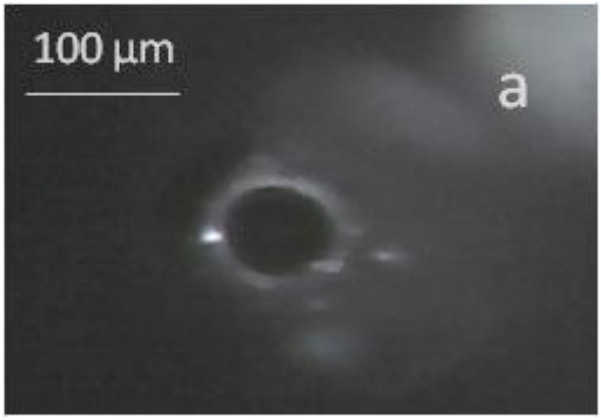

Fig. 4.7*: SEM image of a tip end of a micropipette.*

The contact meniscus was established by cyclic voltammetry with the pipette filled with an aqueous solution containing 1 mM $Ru(NH_3)_6^{3+}$ + 0.1 M KCl, while a conventional platinum disk of 3 mm in diameter was employed as the substrate. A potential of -0.5 V *vs.* a platinum pseudo-reference electrode (PRPt) was applied to the substrate, where the one electron reduction process

of $Ru(NH_3)_6^{3+}$ to $Ru(NH_3)_6^{2+}$ occurred under diffusion control. The micropipette was approached to the substrate in air by a micropositioning system, initially at 10 µm/s, under an optical microscope to control the tip proximity and avoid tip crushing; then the tip was finer moved by the use of a piezo system at 50 nm/s until that a well-defined current flow, due to the reduction of the redox probe, was recorded upon meniscus contacted the substrate (Fig. 4.8).

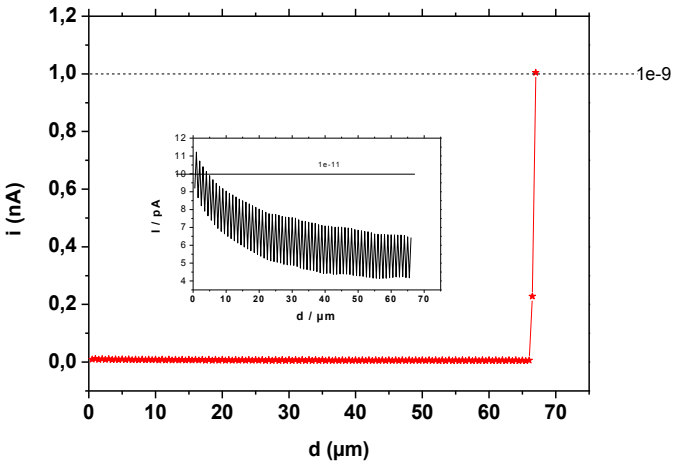

***Fig. 4.8**: Microcapillary approach curve from air to a polycrystalline platinum disk.*

CVs were carried out by applying suitable wave forms at the substrate and Fig. 4.9 shows a series of voltammograms recorded at different scan rates, over the range 5-50 mV/s.

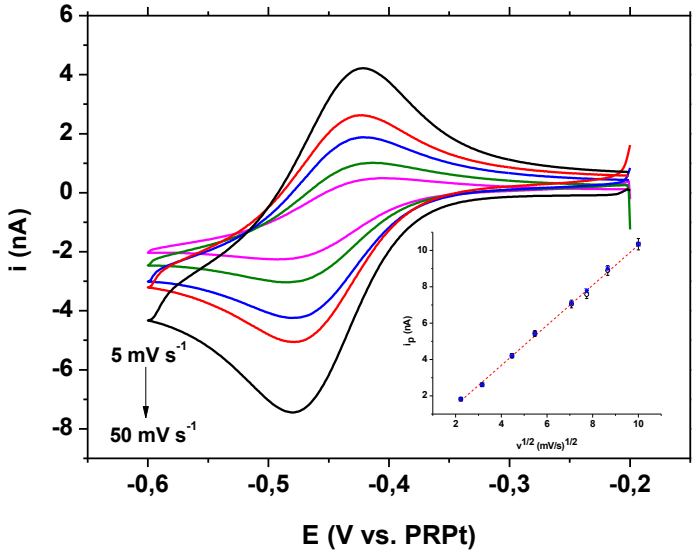

***Fig. 4.9**: Cyclic voltammograms recorded at 5-10-20-30-50 mV/s on 3 mm in diameter Pt disk using a micropipette filled with 3 mM $Ru(NH_3)_6Cl_3$ + 0.1 M KCl. Inset: i_p vs. $v^{1/2}$ plots: (**o**) experimental, (*) simulated data.*

Under these conditions, peak shaped responses, typical for planar diffusion, were obtained. This is related to the fact that the current is essentially dominated by the linear diffusion through the capillary. The cathodic to anodic peak separation equal to 60 (± 1) mV regardless of scan rate, and the linear dependence of the cathodic peak current against the square root of scan rate (inset in Fig. 4.9), confirmed the occurrence of a diffusion limited electrode process, as expected for the redox probe employed here. This behaviour agrees with those reported in earlier works in which pipettes of micrometer size were employed for MC measurements[1,5]. These results are also consistent with the theoretical voltammograms obtained by simulation as described in Section 4.1. The surface area of the platinum substrate wet by the electrolyte, and consequently the diameter of the meniscus, was obtained by using equation 4.3. For the micropipettes used here, the contact radii were of 40 (± 1) µm and 49 (± 2) µm, as evaluated from the slopes of the i_p *vs.* $v^{1/2}$ plots of at least five replicate measurements involving both the tip approaching procedure and CVs recording at different scan rates.

Simulations were also performed by the COMSOL Multiphysics using the micropipette radii determined above and forward peak current agreed with experimental values within 3% (see inset in Fig. 4.9).

4.3 Microcapillary voltammetry at single pores obtained at alumina coated-platinum thin films

The substrate investigated were thin-alumina film coated platinum (Pt/Al_2O_3) samples. They were prepared in a custom-built r.f. magnetron sputtering system, as reported in detail elsewhere[6]. Platinum and alumina layers were deposited in sequence onto silicon wafers. A good adhesion of the Pt layer to the silicon substrates was ensured by a thin Cr layer sputtered at first onto the bare substrates. Fig. 4.10 shows a typical SEM images of cross sections of two Pt/Al_2O_3 samples in which Al_2O_3 thickness is about 250 and 600 nm.

[5] T. M. Day, P. R. Unwin, J. V. Macpherson, *Nano Lett.* **2007**, 7, 51-57.
[6] D. Battistel, S. Daniele, G. Battaglin, M. A. Baldo, *Electrochem. Commun.* **2009**, 11, 2195-2198.

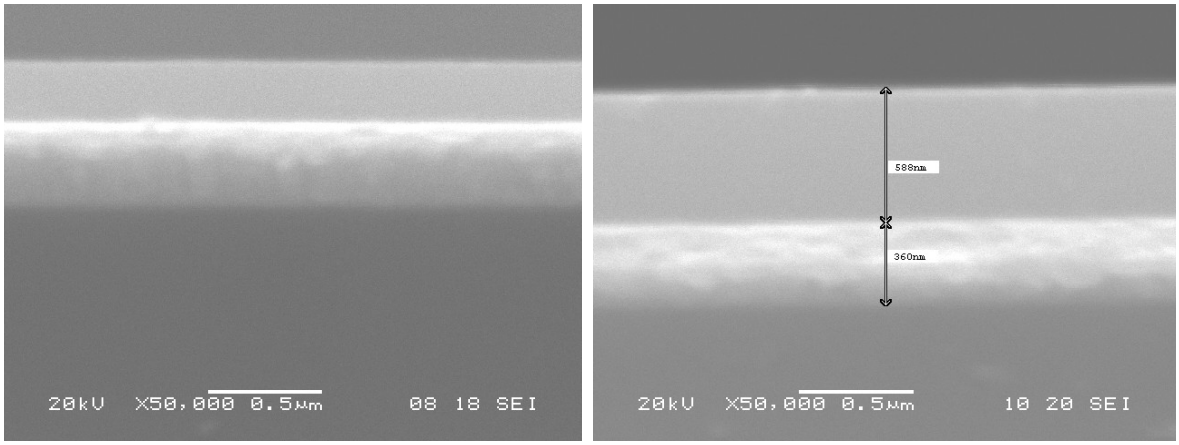

***Fig. 4.10**: SEM images of a cross section of two Pt/Al_2O_3 samples.*

The r.f. magnetron sputtering technique is known to produce densely packed alumina layers[7]. However, when the Pt/Al_2O_3 materials were used as working electrodes in a conventional three electrode electrochemical cell, where the surface area wet by a $Ru(NH_3)_6^{3+}$ solution was 0.13 cm^2 (*i.e.*, 0.2 cm radius), they provided sigmoidal shaped responses as those shown in Figure 4.11. This picture suggested that the samples consisted in ensembles of micro- or nanoelectrodes with no overlap of the individual diffusion layer[8,9].

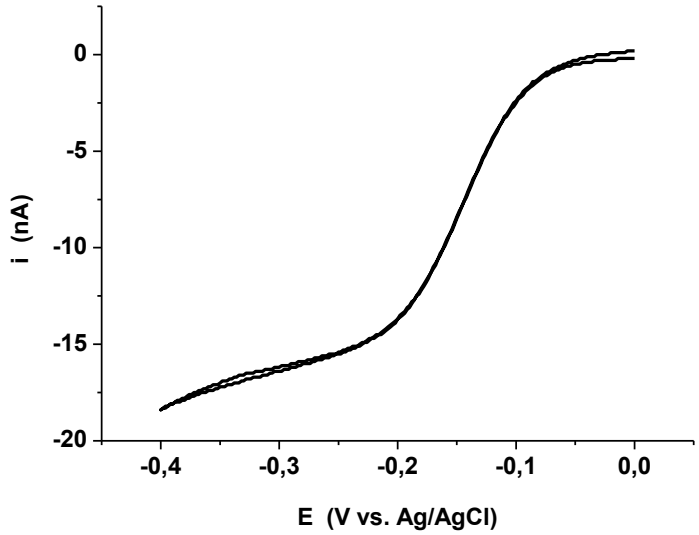

***Fig. 4.11**: Cyclic voltammogram recorded at a Pt/Al_2O_3 sample (0.13 cm^2) used as working electrode in a conventional three electrodes cell containing 3 mM $Ru(NH_3)_6Cl_3$ + 0.1 M KCl aqueous solution. Scan rate: 5 mV/s.*

[7] E. Cattaruzza, G. Battaglin, F. Visentin, E. Trave, *J. Non-Cryst. Solids* **2009**, 355, 1128-1131.
[8] C. Beriet, R. Ferrigno, H. H. Girault, *J. Electroanal. Chem.* **2000**, 486, 56-64.
[9] T. J. Davies, R. G. Compton, *J. Electroanal. Chem.* **2005**, 585, 63-82.

Therefore, it was hypothesised that the alumina layer contained loose pores through which mass transport of the electroactive species down the underlying platinum film could occur. Because of the relatively low pore density of the Pt/Al_2O_3 sample, the micro-electrochemical cell previously described, assembled with the 40-50 µm radius pipettes, seemed suited to ascertain the size of each pore and the distribution over a relatively large surface area. Thus, MC measurements in the scanning mode was employed. To this purpose a square region of a Pt/Al_2O_3 sample (thickness of the alumina layer 500 nm) of 500 µm x 500 µm with 100 µm separation between points, providing 25 sub-areas each of 100 µm x 100 µm (see scheme in Figure 4.12 A), was investigated.

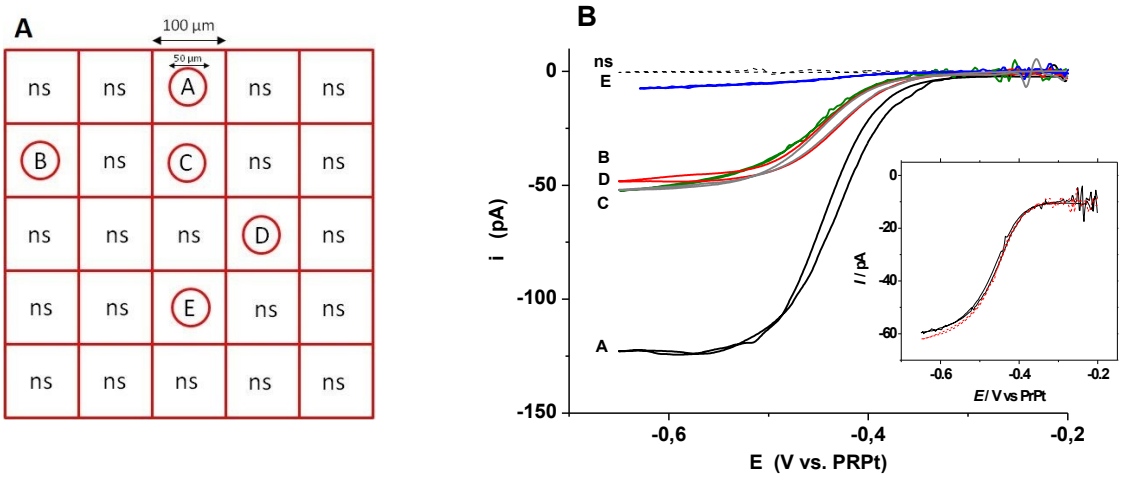

***Fig. 4.12**: A) Scheme of a 500 x 500 µm surface area of the Pt/Al_2O_3 sample examined by MC method. Capital letters indicate the locations where a pore is revealed; ns indicates zones where no current signal is recorded. B) Cyclic voltammograms recorded at 5 mV/s with a pipette (41 µm radius orifice) filled with 3 mM $Ru(NH_3)_6Cl_3$ + 0.1 M KCl aqueous solution; symbols refer to the locations shown in the scheme A). Inset: replicate CVs recorded at the same location (C).*

The micropipette was filled with a 3 mM $Ru(NH_3)_6^{3+}$ + 0.1 M KCl solution and then moved towards the centre of each sub-zone. However, in this case, to enhance the sensitivity in establishing the electrical contact between the meniscus of the pipette and the substrate, a potential of +1.2 V, corresponding to the oxygen evolution process, was applied. In this way sensible current responses (about 20-30 pA) could be readily recorded, as soon as even nanometer-sized conducting surfaces (indicated as capital letters in the scheme of Fig. 4.12 A) came into contact with the pipette meniscus. In case the meniscus contacted an insulating zone (indicated as *ns* in the scheme of Fig. 4.12 A), no current was recorded. When the electrochemical microsystem was set up and the meniscus contacted a conducting zone of the substrate, cyclic voltammograms were recorded at 5 mV/s over the potential range from -0.2 V to -0.7 V.

As is shown in Figure 4.12 B, sigmoidal CVs, similar to that shown in Fig. 4.11, but with much smaller currents, were recorded when the thin meniscus could reveal a continuously open pore across the entire thickness of the alumina layer. Instead, no current was recorded when the meniscus wet only a pore-free alumina surface zone (Figure 4.12 B dashed line). Table 4.1 summarises relevant voltammetric parameters, *i.e.* half wave potential ($E_{1/2}$), steady-state limiting

current (i_{ss}) and potential quartile differences, so-called Tomeš criterion[10] ($|E_{3/4}-E_{1/4}|$, *i.e.*, the difference between the potential measured at ¾ and ¼ of the limiting current), which is related to the reversibility of the electrode process[11]. As is evident from the table, both $E_{1/2}$ and $|E_{3/4} - E_{1/4}|$ values do not depend, within experimental errors, on locations; moreover the Tomeš parameter is very close to 55.8 mV, as expected for a one-electron reversible process at 22° C (which is the working temperature of our experiments).

***Table 4.1**: Voltammetric parameters obtained from CVs recorded at 5 mV/s at different locations of the Pt/Al_2O_3 substrate using a micropipette (orifice 41 µm radius) filled with a 3 mM $Ru(NH_3)_6Cl_3$ + 0.1 M KCl aqueous solution.*

Location	$E_{1/2}$ (± 1 mV)	$\|E_{3/4}-E_{1/4}\|$(±1mV)	i_{ss} (pA)	a (nm)
A	-429	57	133 ± 5	325 ± 10
B	-430	58	48 ± 2	170 ± 5
C	-430	57	51 ± 2	176 ± 6
D	-435	58	53 ± 3	181 ± 6
E	-434	58	7 ± 1	57 ± 7

The steady-state limiting current, instead, depends on the specific locations and the scheme in Figure 4.12 A shows with capital letters the zones where currents could be recorded. From the latter scheme, it is also evident that the pores are unevenly distributed over the alumina surface and are far apart from one another, typically, by more than 100 µm. The reproducibility of the CV responses and consequently the good functioning of the cell apparatus employed here, was assessed by performing at least three replicate measurements in each location; the inset in Fig. 4.12 B shows how well two subsequent voltammograms recorded at the same location overlap.

The size of each pore was evaluated from the steady-state limiting current and using the equation 4.4. It must be considered that, on the basis of the simulations presented in the previous section, the steady-state limiting currents displayed in Table 4.1 can be safely assumed to be not affected by symmetry in the positioning of the pipette meniscus above the pores. Thus, from equation 4.4, assuming the pore is cylindrical-shaped and L is equal to the alumina film thickness, using D = 7.0x10^{-6} cm^2/s, the radii of the pores were evaluated and data are included in Table 4.1. As is evident, the radius of the pores spans from about 55 nm to 325 nm and their average size is 182 (± 95) nm.

A series of measurements as those displayed above was also performed using Pt/Al_2O_3 samples with alumina thickness of 250 and 1000 nm. In general, the results obtained were very similar to the above: the main differences observed among the various samples was the number and average size of the pores determined, which were larger (average 500 ± 180 nm) or smaller (average 100 ± 70 nm), for the 250 nm and 1000 nm alumina sample, respectively.

[10] J. Tomeš, *Collect. Czech. Chem. Commun.* **1937**, 9, 12-18.
[11] A. M. Bond, K. B. Oldham, C. G. Zoski, *Anal. Chim. Acta* **1989**, 216, 177-230.

4.4 Deposition/patterning of a conducting material with silver micro- and nano-particles

The MC technique was also employed to pattern conducting surfaces with a foreign metal and ascertain whether the mass transport characteristics envisaged for soluble redox species also applied in case of species which undergoes nucleation processes onto the electrode surface. Here, in particular, the results concerning the deposition of silver particles onto a platinum surface, arranged in arrays of spots having circular forms and size similar to the pipette meniscus are presented. To this purpose, the pipette was filled with a solution containing 5 mM $AgNO_3$ + 0.1 M KNO_3, acidified to pH 1 with HNO_3, and then assembled in a two-electrode cell by employing a Pt wire as the counter/pseudo-reference electrode. In this case, the electrode process is:

$$Ag^+ + e^- \rightleftarrows Ag^0 \qquad (2)$$

The voltammetric behaviour for this process is displayed in Fig. 4.13. It shows, in the cathodic scan, a peak shaped wave, and in the anodic scan, a current crossover and a stripping peak. Also in this case the cathodic peak current is proportional to the square root of scan rate, although the straight line does not pass through the origin.This behaviour is typical for nucleation processes occurring under planar diffusion, as reported in earlier works for metal deposition at conventional electrodes[12].

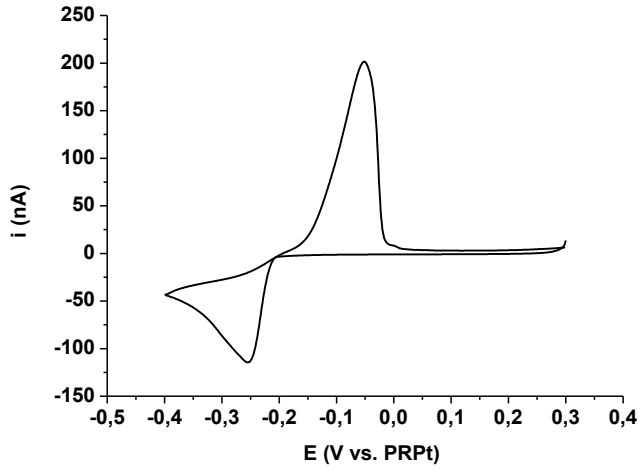

***Fig. 4.13**: Cyclic voltammogram recorded at 50 mV/s with a micropipette filled with an aqueous solution containing 5 mM $AgNO_3$ + 0.1 M KNO_3 acidified to pH 1 with HNO_3 above Pt disk of 3 mm in diameter.*

[12] A) G. Gunawardena, G. J. Hills, I. Montenegro, *J. Electroanal. Chem.* **1982**, 138, 241-254;B) G. Gunawardena, G. J. Hills, I. Montenegro, B. Scharifker, *J. Electroanal. Chem.* **1982**, 138, 225-239; C) A. Hernandez Creus, P. Carro, S. Gonzalez, R. C. Salvarizza, A. J. Arvia, *Electrochim. Act*a **1992**, 37, 2215-2227.

To obtain massive deposition onto an electrode surface, potential step experiments at different deposition times were performed. From the voltammogram in Fig. 4.13, a suitable deposition potential was chosen as -0.4 V *vs.* PRPt. The deposition time was set for 20s, 40s and 60s. Typical current *vs.* time responses recorded under the latter conditions are shown in Fig. 4.14. As is evident, initially the cathodic current increases and then decays to negligible values, once again as expected for nucleation processes governed by planar diffusion. It is dictated by the overlap of the hemispherical diffusion field that arises at each nucleation site.

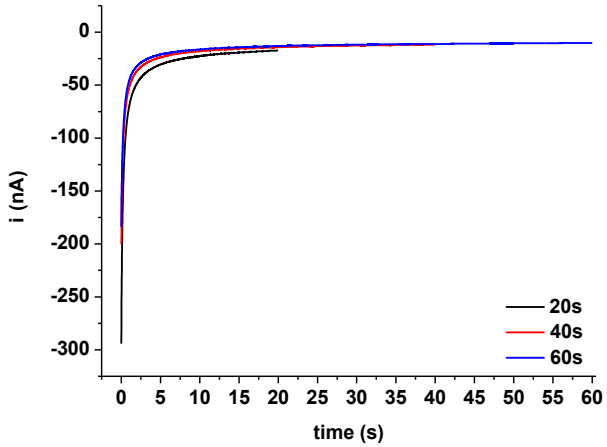

***Fig. 4.14**: Potential step experiments performed with a micropipette filled with 5 mM $AgNO_3$ + 0.1 M KNO_3 acidified to pH 1 with HNO_3 above Pt disk of 3 mm in diameter for different times, as indicated.*

SEM images relevant to an Ag spot recorded after 60 s deposition are displayed in Fig 4.15. From Fig. 4.15 A, it is evident that the size of the circular Ag spot is of about 50 µm diameter, almost equal to that of the pipette meniscus landing. Thus, also for metal deposition processes, the surface area of the substrate involved is dependent on the size of the pipette meniscus. Interesting is also noticing that the silver particles have an almost hemispherical shape with an average size of 200 nm (Fig. 4.15 B-D).

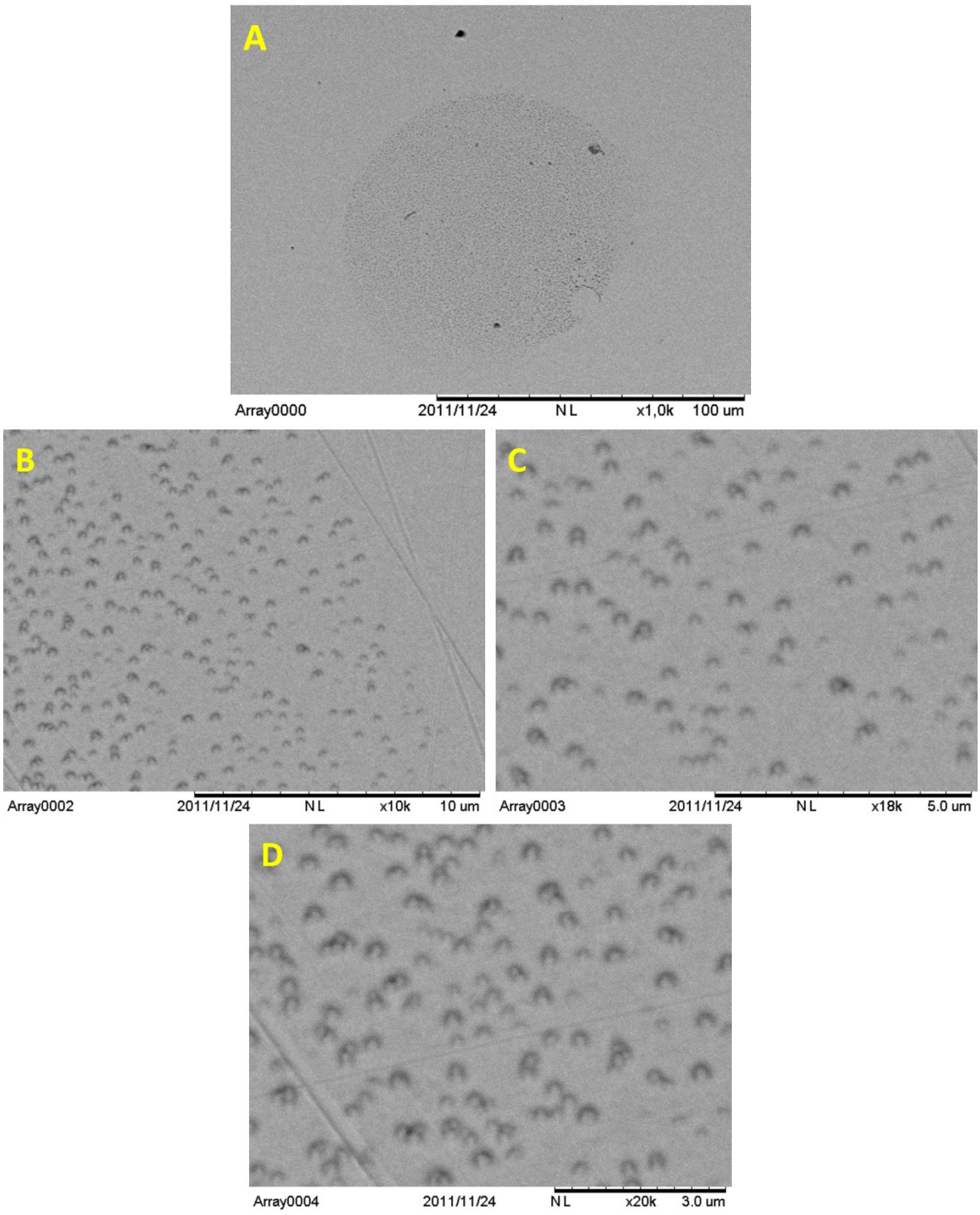

***Fig. 4.15**: SEM images (at different magnifications) for an Ag spot obtained by potential step deposition from a micropipette filled with an aqueous solution containing 5 mM $AgNO_3$ + 0.1 M KNO_3 acidified to pH 1 with HNO_3 above Pt disk of 3 mm in diameter. Deposition potential -0.4 V vs. PRPt; deposition time 60 s.*

The measurements performed at the different deposition times provided similar results, as the size of the silver spots was concerned (*i.e.*, about 50 µm using the same pipette). Also, the size of each particle did not depend on deposition times. Major differences were observed on the

density of particles formed onto the substrate, as is apparent from the optical images of arrays of Ag spots obtained at different deposition times (Fig. 4.16).

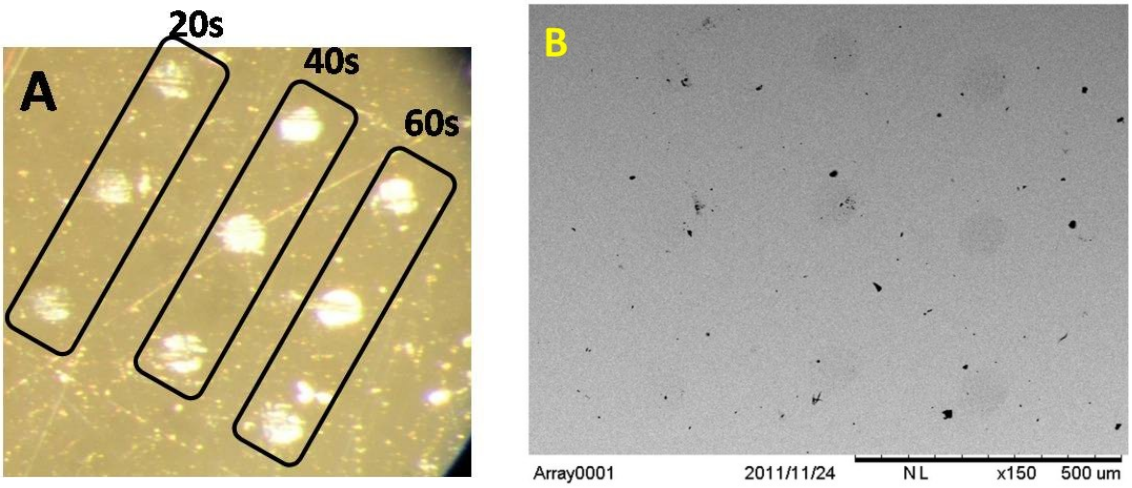

***Fig. 4.16**: A) Optical and B) SEM images of an arrays of nine Ag spots obtained with a micropipette filled with an aqueous solution containing 5 mM $AgNO_3$ + 0.1 M KNO_3 acidified to pH 1 with HNO_3 above Pt disk of 3 mm in diameter. Deposition potential -0.4 V vs. PRPt; deposition time 20s, 40s and 60 s.*

Finally, the reproducibility of the MC approach in the scanning mode was tested by the fabrication of an array of six Ag spots using 60 s deposition time. As is evident from the optical image displayed in (Fig. 4.17) the reproducibility in shape and size is satisfactory.

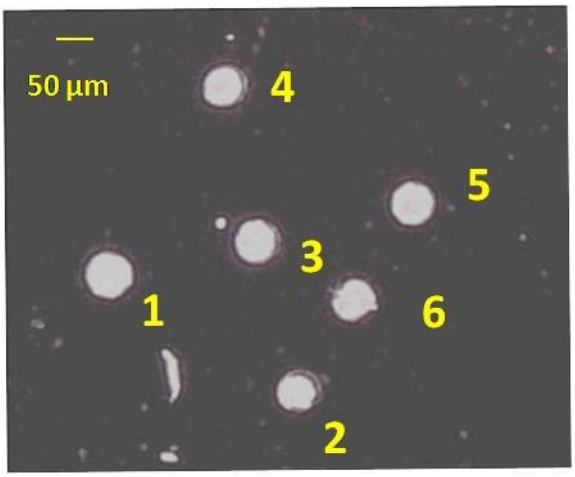

***Fig. 4.17**: Optical image of an array of six Ag spots obtained with a micropipette filled with an aqueous solution containing 5 mM $AgNO_3$ + 0.1 M KNO_3 acidified to pH 1 with HNO_3 above Pt disk of 3 mm in diameter. Deposition potential -0.4 V vs. PRPt; deposition time 60s.*

4.5 Silver deposition on alumina sample by the microcapillary method

A series of measurements, as those discussed in section 4.4 with the micropipette filled with a solution containing 5 mM $AgNO_3$, was also performed to pattern with Ag^0 the Pt/Al_2O_3 sample with an alumina layer of 250 nm. Since the electrode process involved in this case is $Ag^+ + e \rightarrow Ag^0$, in addition to pore distribution on the sample, information on the metal nucleation process within a single nanopore could also be gathered. The measurements were performed at the Pt/Al_2O_3 sample over a 500 x 500 µm region (scheme in Fig. 4.18 A) and, for comparison, above the plain platinum disk electrode. Fig. 4.18 A includes, with capital letters, the locations where conducting zones were revealed. This map provides the same information as those discussed in section 4.3 (scheme of Fig. 4.12 A) in terms of pore distribution and separation between adjacent pores.

As for the CVs, Figure 4.18 B,C show typical responses obtained at three different locations over the Pt/Al_2O_3 substrate, while Figure 4.18 D displays CVs recorded at two different locations over the platinum disk electrode. As is evident, once again, the voltammograms recorded at the two different types of substrates exhibit different features due to the different mass transport regime dominating, it being, as discussed above, radial at the mouth of the pores on the Pt/Al_2O_3 sample and linear at the Pt conventional disk electrode (the behaviour of the Ag^+ deposition under radial diffusion at a microdisk will be discussed in detail in Chapter 5, section 5.3). In addition, the CVs recorded at the Pt/Al_2O_3 sample are dissimilar in terms of current intensity, conceivably due to the different sizes of the pores involved in each specific measurement, while those recorded at the Pt disk are invariant regardless the location examined. However, the shape of the CVs shown in the Figures 4.18 B,C and 4.18 D are congruent with those reported in previous works for metal deposition processes at micro- and nano-electrodes[13] or conventional electrodes[12], respectively. In all cases, the deposition of metallic silver commences at ~ -0.3 V during the cathodic scan, as indicated by the sudden current increase; the process becomes diffusion limited at more negative potentials; a current loop, typical for nucleation and growth of metal above a foreign metal substrate, and a stripping peak at ~ -0.2 V are observed during the anodic scan.

[13] A) B. Scharifker, G. J. Hills, *J. Electroanal. Chem.* **1981**, 130, 81-97; B) S. Daniele, C. Bragato, M. A. Baldo, G. A. Mazzocchin, *Ann. Chim.* **2002**, 92, 203-215; C) J. Velmurugan, J. M. Noel, W. Nogala, M. V. Mirkin, *Chem. Sci.* **2012**, 3, 3307-3314.

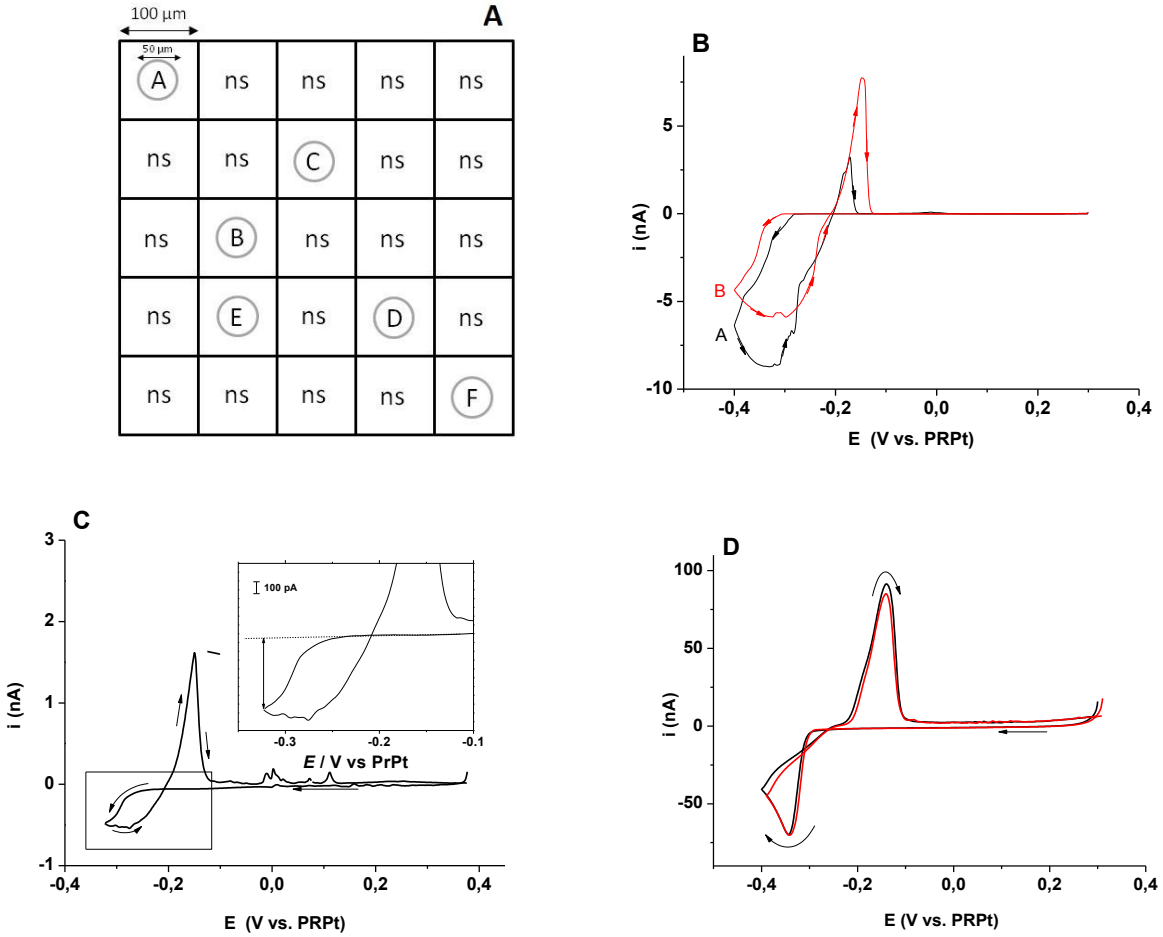

***Fig. 4.18**: A) Scheme of a 500 x 500 µm surface area of the Pt/Al_2O_3 sample examined by MC method. Capital letters indicate the locations where a pore is revealed; ns indicates zones where no current signal is recorded. B)-C) Cyclic voltammograms recorded at 50 mV/s with a micropipette filled with an aqueous solution containing 5 mM $AgNO_3$ + 0.1 M KNO_3, acidified to pH 1 with HNO_3, in different locations: B),C) above the Pt/Al_2O_3 sample and D) above the Pt disk 3 mm diameter. Black and red lines refer to CVs taken in different locations.*

A further distinctive feature of the voltammograms recorded at the Pt/Al_2O_3 substrate with respect to those recorded at the Pt disk was the rather large variability of the charge involved in the stripping peak (Q_{an}) with respect to the corresponding charge passed during the cathodic scan (Q_{ca}) (Table 4.2). In fact, while at the platinum substrate, five replicate measurements, performed at different locations provided Q_{an}/Q_{ca} equal to 0.86 ± 0.01, at the Pt/Al_2O_3 sample, the latter parameter varied from about 0.05 to 0.90.

This fact was explained considering that, at the Pt disk, the silver deposition and stripping processes involved uniformly the entire surface wet by the pipette meniscus; at the Pt/Al_2O_3 sample, metal nucleation and growth occurred, initially within the pore up to the mouth of the orifice, then silver overgrew laterally over the insulating alumina surface. In the latter situation, during the stripping step, only the metal that remained in electrical contact with the Pt nanodisk at the bottom of the pore could be oxidised back to the solution.

***Table 4.2**: Cathodic and anodic charges involved in the CVs recorded at different locations of the Pt disk and Pt/Al_2O_3 substrate using a micropipette (orifice 49 µm radius) filled with 5 mM $AgNO_3$ + 0.1 M KNO_3, acidified to pH 1 with HNO_3. V_S refers to the volume of Ag oxidised during the anodic stripping step.*

Location	*Substrate*	Q_{cat} *(nC)*	Q_{an} *(nC)*	Q_{an}/Q_{cat}	V_S *(µm³)*
[a]	Pt	270.5	235.3	0.87	-
[a]	Pt	278.1	241.9	0.87	-
[a]	Pt	280.4	241.1	0.86	-
[a]	Pt	274.3	233.2	0.85	-
[a]	Pt	281.4	242.0	0.86	-
A	Pt/Al_2O_3	5.1	0.8	0.16	0.08
B	Pt/Al_2O_3	29.7	1.5	0.05	0.16
C	Pt/Al_2O_3	20.6	5.2	0.25	0.55
D	Pt/Al_2O_3	32.4	3.6	0.11	0.35
E	Pt/Al_2O_3	35.1	3.3	0.09	0.35
F	Pt/Al_2O_3	1.1	1.0	0.91	0.11

From Q_{an}, the volume of silver dissolved (V_S) was evaluated by Eq. (4.6):

$$V_S = Q_{an}V_M/nF \qquad (4.6)$$

where V_M = 10.273 cm^3/g is the molar volume of silver[14] and data for the Pt/Al_2O_3 sample are included in Table 4.2. As is evident, in the cases for which $Q_{an}/Q_{ca} << 1$, V_S exceeds that of the largest pore (*i.e.*, 0.08 μm^3) evaluated from steady-state voltammetry in the $Ru(NH_3)_6^{3+}$ solution, probably because tiny amounts of silver surrounding the mouth of the pore, in addition to that filling the pore itself, are dissolved in the anodic process. For the case Q_{an}/Q_{cat} = 0.90, which was obtained by reversing the potential scan at a less negative value (Fig. 4.18 C), V_S corresponds to that of a cylinder of height 250 nm (*i.e.*, the alumina thickness) and basal radius equal to 377 nm. A basal radius for the disk at the bottom of the pore equal to 341 nm was evaluated from the quasi steady-state limiting current obtained in the CV during the cathodic scan (inset in Fig. 4.18 C) and using equation (4.5). This result is consistent with a deposition and stripping process in which a single pore is filled with the metal up to the pore mouth.

Further insights on the nucleation process within a single pore were obtained by performing potential step measurements. Fig. 4.19 A shows a typical current against time (t) transient recorded at the Pt/Al_2O_3 sample (on a conducting location) by stepping the potential from 0.0 V to -0.4 V (*i.e.*, where metal deposition is diffusion-controlled) over a period of 20 s.

[14] *Handbook of Chemistry and Physics*, 72nd Ed. (Ed.: D. R. Lide), CRC, Boca Raton, **1991-1992**.

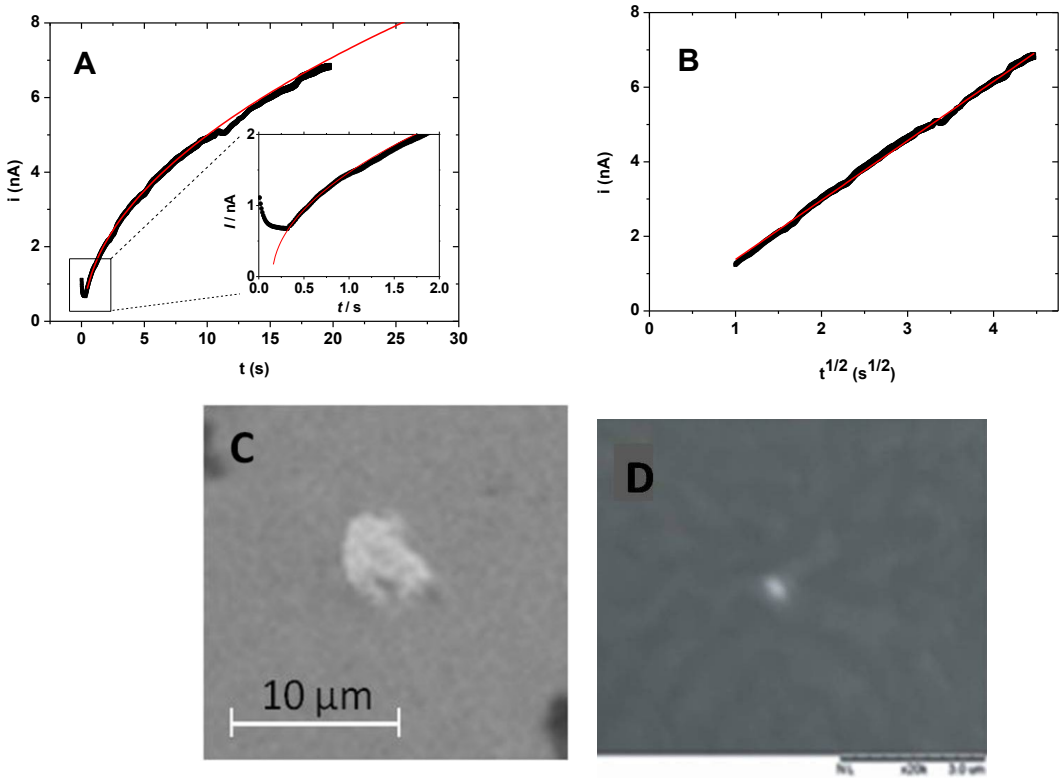

***Fig. 4.19**: A) Chronoamperometry recorded with a micropipette filled with an aqueous solution containing 5 mM $AgNO_3$ + 0.1 M KNO_3, acidified to pH 1 with HNO_3 above the Pt/Al_2O_3 sample, stepping the potential from 0.0 to -0.4 vs. PRPt; inset: enlargement of the transient at shorter times. B) i vs. $t^{1/2}$ plot of the transient recorded in A). C), D) SEM micrographs of silver spots obtained on pores of the Pt/Al_2O_3 sample after deposition times of 20 s and 350 ms respectively.*

The shape of the *i vs. t* response is congruent with those reported in the literature for diffusion controlled growth of a single hemispherical nucleus at solid micro- and nanoelectrodes, and for which the following equation applies[15]:

$$i = 2^{3/2}\pi nF(Dc_b)^{3/2}(V_M t)^{1/2} \qquad (4.7)$$

This equation predicts a linear dependence of *i vs.* $t^{1/2}$ and the plot shown in Figure 4.19 B, which refers to the analysis of the experimental transient, confirms this view. From the slope of the *i vs.* $t^{1/2}$ plot a diffusion coefficient value for Ag^+ ions of 1.41×10^{-5} cm^2/s was calculated. This value compares well with 1.55×10^{-5} cm^2/s reported in ref 16[16]. In Figure 4.19 A a red line indicates the theoretical transient evaluated by equation (4.7). The analysis of the transient at shorter times (inset in Figure 4.19 A) provided a time lag of 150 ms, that is the delay time needed before the silver nucleus started to grow. This value is comparable with those observed at micrometer and conventional electrodes, but it is much larger than 2-7 ms reported recently in nucleation studies of silver at single polished platinum nanoelectrodes of 200 nm radius (*i.e.,* similar to the average value

[15] G. J. Hills, D. J. Schiffrin, J. Thompson, *Electrochim. Acta* **1974**, 19, 657-670.
[16] S. Kariuki, H. D. Dewald, *Electroanalysis* **1996**, 8, 307-313.

found in our sample). These differences might be due to the different experimental conditions employed in the works. In addition, in ref 13C, a faster and sensitive current amplifier was used, against the conventional potentiostat employed in this work.

In order to verify that just one silver spot could be grown from transients as that displayed in Figure 4.19 A, the silver deposit obtained onto the alumina layer of the Pt/Al_2O_3 sample, after 20 s deposition, was visualized by SEM (Figure 4.19 C). In the figure a white, almost circular spot of about 5 µm diameter is evident. This value compares well with 3.14 µm evaluated from the charge obtained by integration of the current passed in the 20 s deposition time (90.3 nC), neglecting the small amount of deposit that is needed to fill the pore, and using the equation $r = (2Dc_bV_Mt)^{1/2}$, which is valid for a hemispherical spot of radius r[17]. The use of a deposition time as low as 350 ms allowed filling just a single pore with orifice radius of 220 nm, which was visualized by SEM (Fig. 4.19 D).

[17] S. Daniele, M. A. Baldo, P. Ugo, G. A. Mazzocchin, *Anal. Chim. Acta* **1989**, 219, 9-19.

Chapter 5: SECM and voltammetric investigation on silver micro- and nano-particles

Recent advances in the research and development of engineered nanomaterials have enabled a wide range of novel applications for commercial and industrial uses. Among others, silver nanoparticles (AgNPs) have received a great attention because of their distinctive physicochemical and biological properties. In fact, AgNPs are increasingly employed in various medical and consumer products[1,2], including household antiseptic sprays and antimicrobial coatings for medical devices that sterilize air and surfaces[3,4]. The antiseptic properties of silver are known since ancient times; Greeks, Romans and Egyptian used silver for the conservation of water and food[5]. Silver has also been used for a long time to prevent infection of burnt skin[6]. In the first half of the 20th century (until the introduction of antibiotics), silver was used to a large extent as aqueous colloidal dispersion for oral consumption. In some cases, this led to argyria, which is due to the incorporation of silver into the skin and into other tissues.

AgNPs are known to dissolve and release Ag^+ ions under physiological conditions, and there has been much debate in the literature to establish if the reactivity of AgNPs arises due to an ionic or particulate effect, or both. To understand and predict how AgNPs behave in biological environments, it is essential considering the thermodynamics driving the dissolution of this material and how this is related to the physicochemical properties of the particles and environmental conditions. Several factors such as ionic strength, composition of the dispersion medium, pH, temperature and oxidation state of the material have been shown to alter the properties and dissolution rates of silver particles. In addition, it has been shown that size, charge, and surface modifications of metallic silver particles affect their cytotoxicity[5]. Therefore, investigation on the redox properties of silver particles and their reactivity at interfaces of various environments is highly desirable. In this chapter, investigation strategies based on combination of SECM and voltammetry to provide information on the redox properties of Ag in various types of silver particles and the kinetic of silver ion release from the various materials are presented. In particular, the oxidation state of silver in silver particles embedded on various solid or soft substrates is investigated by using SECM in feedback mode. The silver ion release from the materials is investigated by combining the proximity mode of SECM with voltammetry. Since one of the goals of the investigation was to establish a procedure for characterizing silver modified polymeric matrices that can find applications in food packaging, the voltammetric behavior of silver ions in different

[1] M. E. Quadros, L. C. Marr, *Environ. Sci. Technol.* **2011**, 45(24), 10713-10719.
[2] J. S. Kim, E. Kuk, K. N. Yu, J. H. Kim, S. J. Park, H. J. Lee, S. H. Kim, Y. K. Park, Y. H. Park, C. Y. Hwang, Y. K. Kim, Y. S. Lee, D. H. Jeong, M. H. Cho, *J. Nanomed. Nanotechnol.* **2007**, 3(1), 95-101.
[3] X. Chen, H. J. Schluesener, *Toxicol. Lett.* **2008**, 176(1), 1-12.
[4] T. Faunce, A. Watal, *Nanomedicine* **2010**, 5(4), 617-632.
[5] J. W. Alexander, *Surg. Infect.* **2009**, 10, 289-292.
[6] H. J. Klasen, *Burns* **2000**, 26(2), 117-130; H. J. Klasen, *Burns* **2000**, 26(2) 131-138.

liquids simulating food matrices (as established by the European Commission with the European Regulation 10/2011) is also illustrated.

5.1. Preparation of the investigated samples and characterization by SEM

The substrates investigated were: silver particles embedded in a Nafion® matrix and cast onto a glass substrate or glassy carbon electrode (GCE); biosynthesized AgNPs embedded in an exopolysaccharide matrix; commercially available goods such as a microfiber kitchen cloth with antibacterial silver ions (distributed by Martini SpA, Coenzo di Sorbolo, PR, Italy) and an antimicrobial food container with Microban® 3G Silver™ Technology (distributed by Adamo srl, Castelfidardo, AN, Italy).

5.1.1 Silver particles in Nafion® films

Chemically reduced samples

50 µL of a suspension made by mixing 1:1 aqueous $AgNO_3$ solutions at different concentrations (*i.e.*, 1/10/50 mM $AgNO_3$) and Nafion® (0.5% w/v in methanol) were cast coated onto a polished glass slide and the solvent let evaporating overnight; the glass slides were washed copiously with milli-Q water to eliminate the excess of silver nitrate. The samples were then treated with a 1:1 Na_2CO_3 (5 g in 100 mL) and formaldehyde (37% CH_2O, 5 mL in 100 mL) solution to allow the reduction of silver ions. The excess of the reagents added were eliminated by rinsing with milli-Q water. The samples were dried in a controlled environment avoiding the contact with light. The samples were used for the optical and electrochemical investigations immediately after their preparation. In what follows, these samples are identified as *cr 1mM Ag/Naf/glass*, *cr 10 mM Ag/Naf/glass* and *cr 50 mM Ag/Naf/glass* for the 1 mM, 10 mM and 50 mM $AgNO_3$ solutions employed, respectively.

The use of different concentrations of $AgNO_3$ aqueous solutions provided Nafion® film with different amounts of silver particles. Typical SEM images of the various samples thus prepared are shown in Fig. 5.1 A-C.

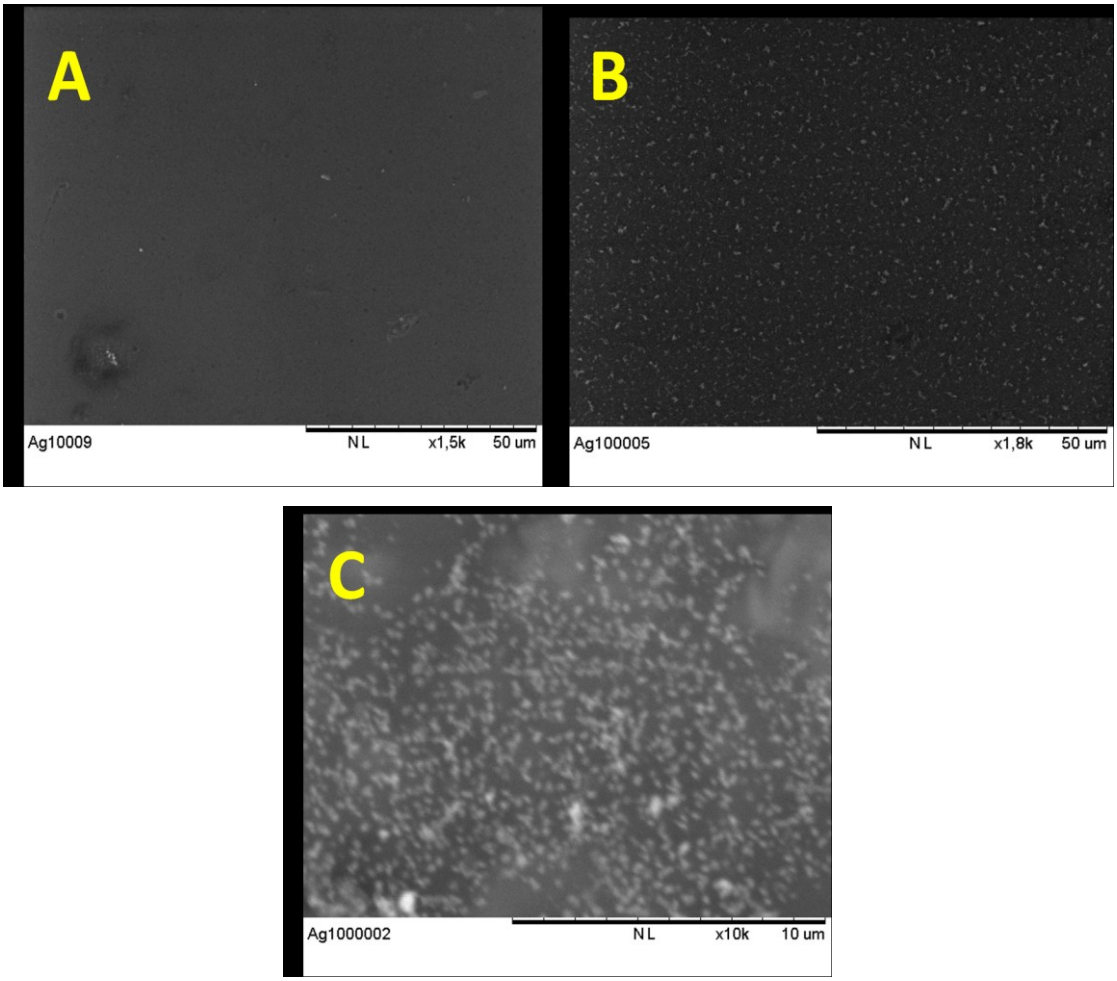

***Fig. 5.1**: SEM images of the silver nanoparticles reduced by formaldehyde and embedded in Nafion® membrane; samples prepared from A) 1 mM $AgNO_3$, B) 10 mM $AgNO_3$ and C) 50 mM $AgNO_3$.*

From the images it is evident that the density of silver nanoparticles increases with increasing the concentration of $AgNO_3$ used for the synthesis of the materials. The average size of the AgNPs, as roughly estimated from the SEM image, was 200 (± 10) nm.

Electrochemically reduced samples

A procedure similar to that described above was employed for the preparation of $AgNO_3$: Nafion® suspensions to be cast onto the surface of a 3 mm in diameter GCE. For these samples, however, the reduction of silver ions was conducted electrochemically using different procedures as outlined below.

1) The first procedure involved the use of the GCE modified by the $AgNO_3$/Nafion® suspension and the reduction of silver ions was accomplished by applying a constant potential at -0.2 V (*vs.* Ag/AgCl) for 300 s. Fig. 5.2 displays the SEM images and relevant EDS responses of silver deposits thus obtained.

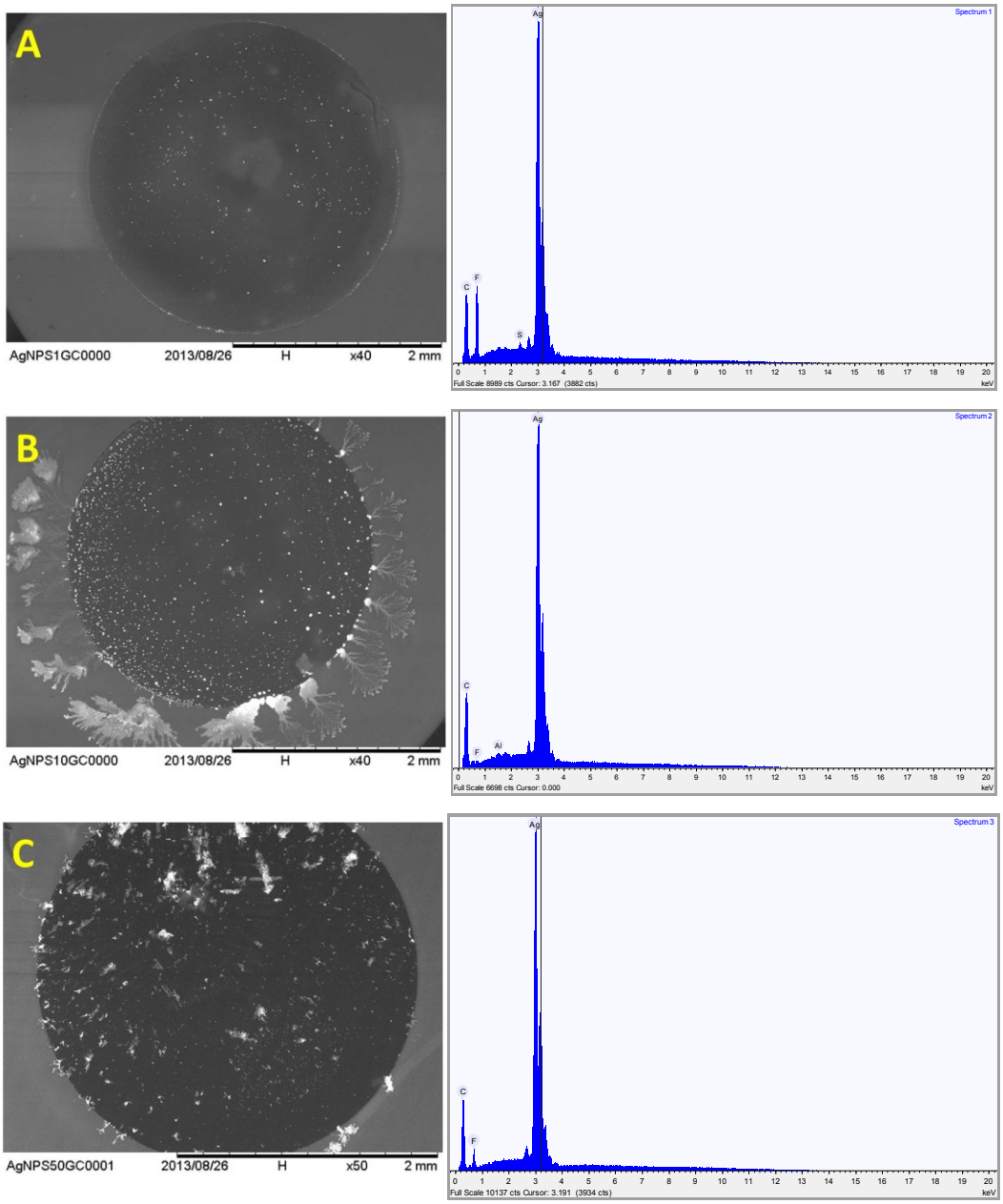

***Fig. 5.2**: SEM images of silver particles deposited by using a constant potential of -0.2 V vs. Ag/AgCl for 300 s starting from GCE coated with $AgNO_3$ and Nafion® suspension containing 0.5% w/v Nafion® and A) 1 mM $AgNO_3$, B) 10 mM $AgNO_3$ and C) 50 mM $AgNO_3$. The corresponding EDS spectra are shown.*

As is evident, polydisperse (average 4 µm in diameter) and randomly distributed silver particles were formed from the 1 mM $AgNO_3$ solution (Fig.5.2 A). Less defined (from a geometrical point of view) silver deposits, formed mainly at the boundary between the glassy carbon surface and the teflon support, were obtained from the 10 mM and 50 mM $AgNO_3$ solutions. The stability of the latter silver deposits was rather poor and therefore not further considered for SECM measurements.

2) In order to improve the homogeneity of the silver deposits and decrease the size of the Ag particles, procedures involving reduction/accumulation and oxidation/dissolution cycles were employed.

In the first case, the 1 mM $AgNO_3$/Nafion® modified GCE was cycled in a silver ion-free 0.1 M KNO_3 aqueous solution for at least 20 cycles over the potential window + 0.2 V to -0.3 V *vs.* PRPt. This procedure was revealed as not useful, as the amount of silver particles formed onto the substrate electrode (as indicated by the CVs responses displayed in Fig. 5.3) was very low. This procedure was therefore further modified and the Nafion®-modified GCE was cycled over the same potential window in a solution containing 1 mM $AgNO_3$ + 0.1 M KNO_3. Under the latter conditions, a more efficient accumulation onto the GCE and better defined silver particle deposits were obtained as is clearly evident from the CVs displayed in Fig. 5.4, and the SEM image and EDS displayed in Fig. 5.5. Under these conditions regular and homogeneously distributed spherical particles were obtained with average size of 1.2 (± 0.6) µm. These samples are identified as *ecv 1 mM Ag/Naf/GCE.*

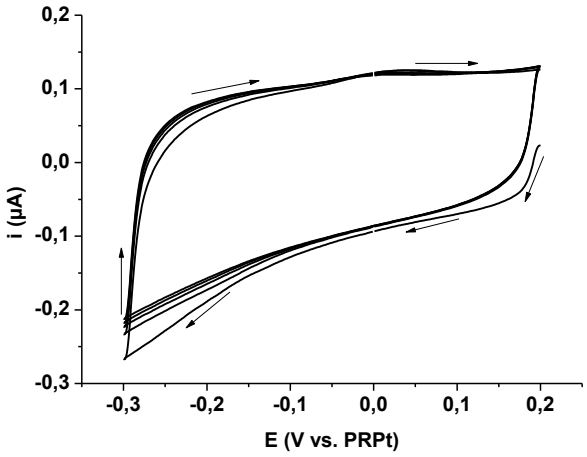

Fig. 5.3 *Cyclic voltammograms recorded for ecv 1 mM Ag/Naf/GCE sample. Scan rate 50 mV/s.*

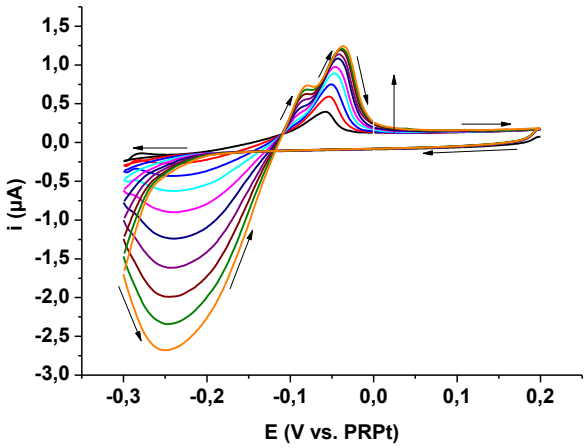

Fig. 5.4: *10 repetitive cyclic voltammograms recorded for the ecv 1 mM Ag/Naf/GCE sample in 1 mM $AgNO_3$ + 0.1 M KNO_3 solution. Scan rate 50 mV/s.*

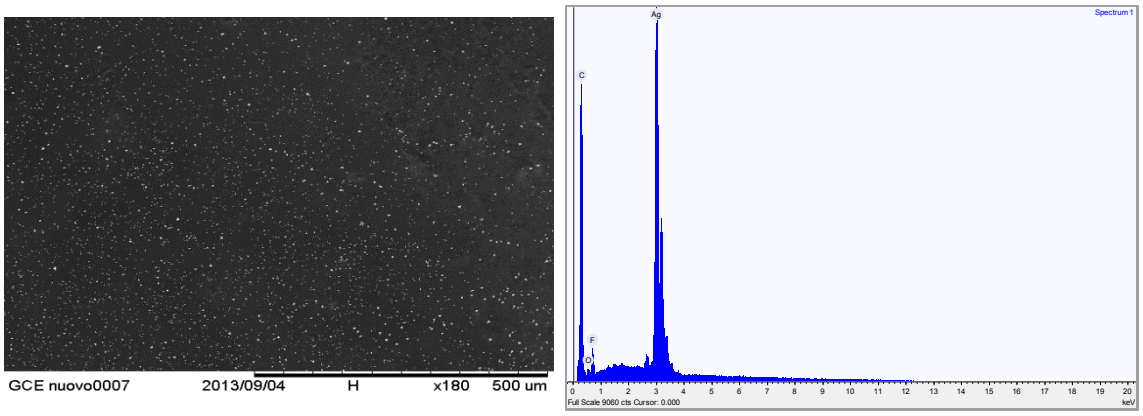

***Fig. 5.5**: SEM image of ecv 1 mM Ag/Naf/GCE in 1 mM $AgNO_3$ + 0.1 M KNO_3 solution (left); EDS spectra (right).*

Commercially available AgNPs particles

AgNPs embedded in Nafion® films were also prepared by casting onto a GCE 3.5 µL of a suspension made of 3 mL of 0.5% w/v Nafion® and 17 mg of silver nanoparticles powder, commercially available (Inframat Advanced Materials™ LLC, Progress, Dr Manchester, CT, U.S.A., particle size: 30 – 90 nm). These samples are identified as *c-Ag/Naf/GCE*.

A SEM image and a relevant EDS response is displayed in Fig. 5.6. As is evident not homogeneously distributed Ag particles onto the GCE surface with average size of 660 (± 50) nm formed. This was probably due to the occurrence of AgNPs aggregation during the sample manipulation. In addition, from CVs measurements (not shown) it resulted that no electrical contact of the AgNPs with the GCE surface existed.

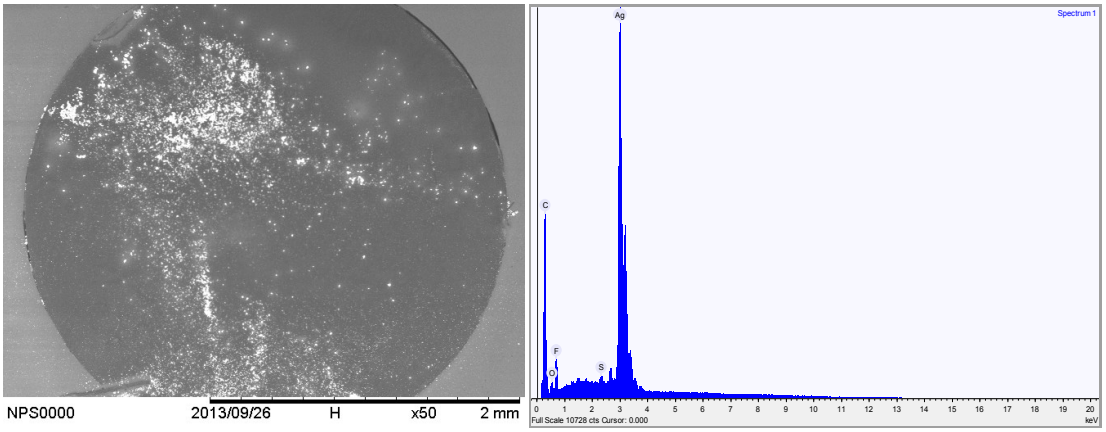

***Fig. 5.6**: SEM image for c-Ag/Naf/GCE sample and EDS spectra.*

5.1.2 AgNPs biosynthesized and embedded in exopolysaccharides

AgNPs embedded in a branched exopolysaccharide matrix (EPS), AgNPs-EPS, were prepared during the growth of *Klebsiella oxytoca* BAS-10, following a procedure reported in detail

elsewhere[7]. Briefly, 200 µL of a suspension containing *KO* BAS-10 cells, kept in cryovials at −80°C in 25% glycerol and nutrient broth, were inoculated in chloride-free NAC medium at pH 7.6, adjusted by adding NaOH[7]. The *KO* BAS-10 cultures were grown in aerobic conditions, at a controlled temperature of 30°C. Aerobic conditions were ensured by stirring the cultures with an orbital stirrer under air-exposed media. At stationary phase of growth, $AgNO_3$ (to provide 50 mg/L of total Ag) was added to the *KO* BAS-10 cultures. These were left for 24–48 hours, till the metal-enriched polysaccharide flocculated in the bottom of the flask. AgNPs-EPS thus obtained were subsequently separated by centrifugation and then treated with cooled ethanol in order to obtain a final hydroalcoholic solution 70% v/v. The colloidal material was kept at 5°C overnight, dried under vacuum and grinded in a mortar.

A TEM image of the material obtained is displayed in Fig. 5.7. As is evident, the high electron-dense spots, due to AgNPs, are embedded on the polysaccharide matrix, and display, predominantly, a spherical shape. Digital analysis provided an average size of 11 ± 5 nm. This value is within those obtained for AgNPs produced by using other bacterial exopolysaccharides[8].

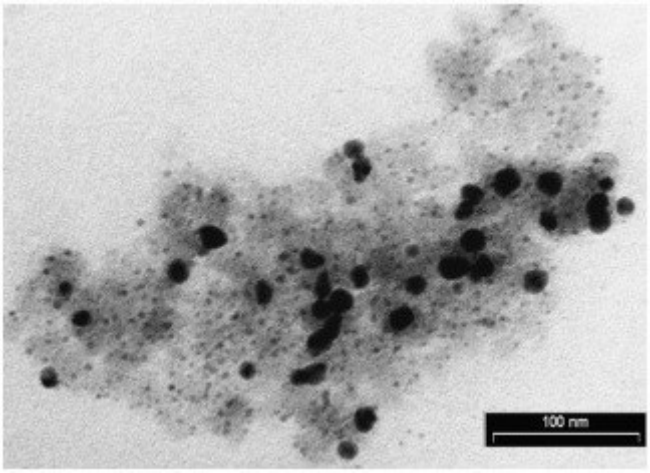

Fig. 5.7*: TEM image obtained for AgNPs loaded in exopolysaccharide.*

For SECM measurements, AgNPs-EPS materials were deposited onto glass slides, previously washed with ethanol and water, dried under a stream of nitrogen and pre-treated with polylysine to allows a better adhesion of AgNPs-EPS onto the glass substrate.

5.1.3 General comments on the preparation procedures of the Ag loaded materials

From the above results it appears that more profitable procedure that enables obtaining AgNPs with regular shape and controlled size is the biosynthetic route. It must be considered, however, that literature reports provide information on the possibility to obtain well defined AgNPs

[7] F. Baldi, D. Marchetto, S. Paganelli, O. Piccolo, *New Biotechnol*. **2011**, 29, 74-78.
[8] P. Kanmani, S.-T. Lim, *Process Biochem.* **2013**, 48, 1099-1106.

in Nafion® matrices using different experimental conditions[9,10]. The synthesized material obtained here were in any case further investigated to ascertain the redox state of Ag in the Ag deposits and their reactivity in aqueous or aqueous/ethanol media.

5.2 SECM approach to establish the redox state of Ag in AgNPs

In order to establish the redox state of the silver nanoparticles embedded in the polymer matrices, SECM strategies based on feedback and linear scan modes were investigated. The measurements were performed by immersion the substrate in aqueous solution, containing 0.1 M KNO_3 as supporting electrolyte and K_3IrCl_6 as redox mediator. The presence of Ag^0 in the AgNPs can be revealed by the occurrence of the following series of reactions:

$$[Ir(Cl)_6]^{3-} \rightarrow [Ir(Cl)_6]^{2-} + e^- \quad (1)$$

$$[Ir(Cl)_6]^{2-} + Ag^0 \rightarrow [Ir(Cl)_6]^{3-} + Ag^+ \quad (2)$$

Reaction 2) can occur because the $[Ir(Cl)_6]^{3-}/[Ir(Cl)_6]^{2-}$ redox system is characterized by a standard potential of 0.867 V *vs.* NHE, which is higher than 0.797 V *vs.* NHE of the Ag^+/Ag^0 system. In the SECM method, reaction (1) occurs at the microdisk electrode when it is poised at a suitable potential, while reaction (2) occurs at the substrate only in the presence of metallic silver and when the tip-substrate distance is less than about 10 times the microdisk electrode radius.

The potential at which the reaction (1) occurs under diffusion controlled conditions was established by steady-state voltammetry in a solution containing 1 mM K_3IrCl_6 and 0.1 M KNO_3. Figure 5.8 shows a typical voltammogram obtained at a 12.5 µm radius Pt electrode, at 10 mV/s. It is evident that an applied potential of 0.95 V *vs.* Ag/AgCl to the micro tip is suitable to guarantee a diffusion controlled process for the redox mediator.

[9] B. Domenech, M. Munoz, D. N. Muraviev, J. Macanas, *Chem. Commun.* **2014**, 50, 4693-4695.
[10] V. Pifferi, V. Marona, M. Longhi, L. Falciola, *Electrochimica Acta* **2013**, 109, 447-453.

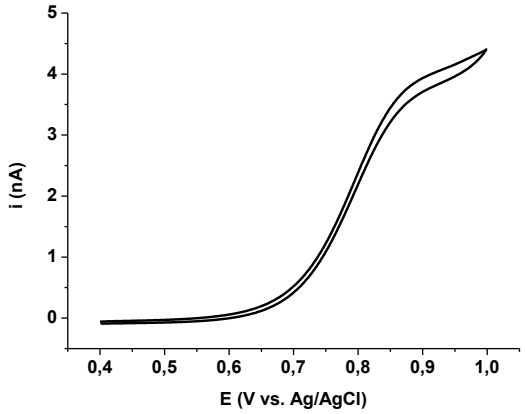

***Fig. 5.8**: Steady-state voltammogram recorded in aqueous solution containing 1 mM $K_3Ir(Cl)_6$ + 0.1 M KNO_3 at 10 mV/s. Working electrode: Pt disk 12.5 µm radius.*

To reveal the presence of Ag^0 in the various Ag loaded materials, approach curves were performed with the microelectrode biased at 0.95 V *vs.* Ag/AgCl. The presence of Ag^0 in the Ag particles containing samples was indicated by the increase of the current upon approaching the substrate (*i.e.*, positive feedback, Fig. 5.9 A, B). In the absence of silver particles containing Ag^0, reaction (2) does not take place, the substrate hinders the diffusion of the redox mediator and the current decreases, as the tip-substrate distance decreases (*i.e.*, negative feedback, Fig. 5.9 C, D).

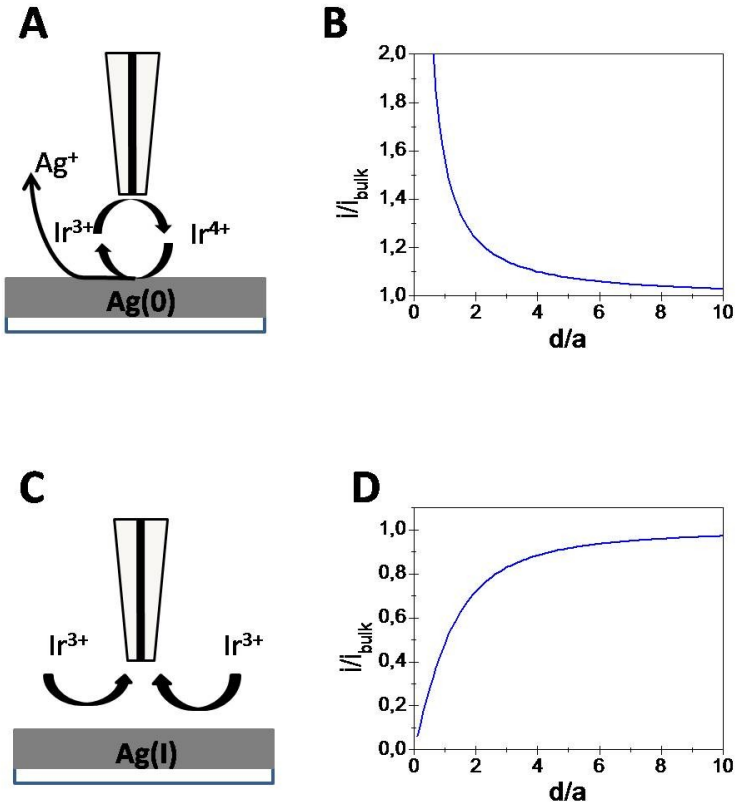

***Fig. 5.9**: Schematic of the redox processes occurring at the microdisk electrode and substrate with $[Ir(Cl)_6]^{2-}$ /$[Ir(Cl)_6]^{3-}$ and Ag^+/Ag^0 systems.*

This procedure was applied to the various samples and the results obtained are summarized below.

Fig. 5.10 shows typical approach curves obtained for the samples prepared as reported in 5.1.1, and, for comparison, those obtained for Nafion® and Nafion® containing $AgNO_3$ untreated with formaldehyde. As is evident, the approach curves recorded above the samples treated with $AgNO_3$ display attenuated negative feedback (*i.e.*, samples treated with 1 mM and 10 mM $AgNO_3$) or complete positive feedback (*i.e.*, sample treated with 50 mM $AgNO_3$). These data clearly suggest that sensible amounts of Ag^0 are present in the investigated samples. However, the amounts of Ag^0 is, as expected, higher in the samples treated with the more concentrated $AgNO_3$ solutions. Measurements performed in different locations of the same samples and in different samples obtained from the same stock displayed similar trends.

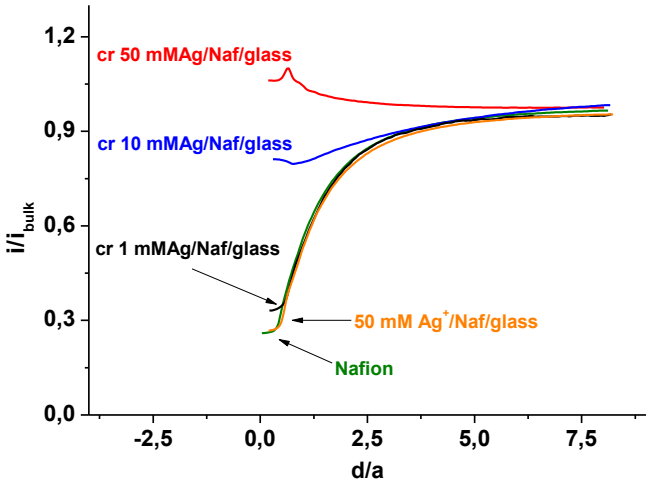

Fig. 5.10*: Approach curves recorded above (--) cr 1mM Ag/Naf/glass, (--) cr 10mM Ag/Naf/glass, (--) cr 50mM Ag/Naf/glass, (--) 50 mM Ag^+/Naf/glass and (--) Nafion samples.*

The sample prepared from 1 mM $AgNO_3$ (black line Fig. 5.10) shows an almost negative feedback approach curve, which would indicate the absence of Ag^0 in the silver deposits. This finding can be explained taking into account the density of the Ag particles embedded in Nafion® film, which is relatively low (Fig. 5.1 A). In fact, it is reasonable admitting that Ag in the silver deposits is mainly in an oxidized form, due to spontaneous corrosion phenomena induced by oxygen from air. This process, likely, also occurs at the samples containing higher amounts of silver deposits; however the Ag^0 containing silver particles are probably still high enough to produce the regeneration of the redox mediator according to reactions 1)-2).

The distribution of Ag^0 in the silver particles was established by performing SECM in the linear scan mode. To contrast the responses obtained above an insulating material and those of the Ag loaded samples, the linear scans were recorded on the glass substrate, glass/Nafion® and glass/Nafion® loaded with silver particles. These measurements were performed by positioning the microelectrode 10 µm above the samples and translated in one dimension over a 500 µm distance.

Fig. 5.11 shows typical line scans obtained for the different samples studied. The black curve refers to the scan acquired above the uncoated glass substrate. It is featureless and the small current changes can be attributed to topography effects[11]. A similar response was obtained above the glass/Nafion® (blue curve), whereas the sample treated with $AgNO_3$ and formaldehyde (red curve) displays current spikes conceivably due to the presence of Ag^0 in the silver particles.

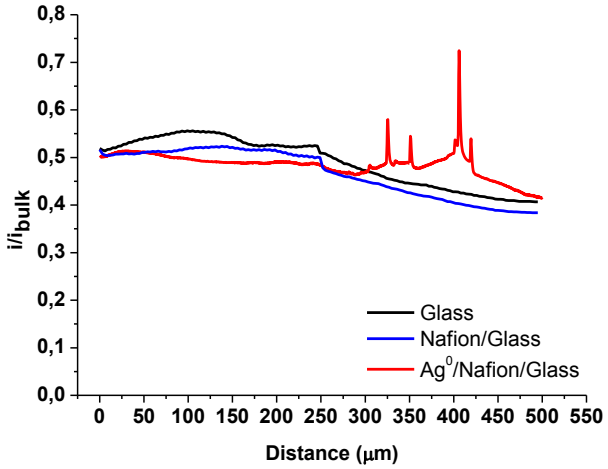

Fig. 5.11*: Line scans recorded above a (--) glass substrate, (--) Nafion modified glass substrate and (--) silver nanoparticles/Nafion modified glass substrate.*

Typical approach curves recorded for the samples prepared as described in 5.1.1 (electrochemically reduced samples, procedure 2) are shown in Fig 5.12.

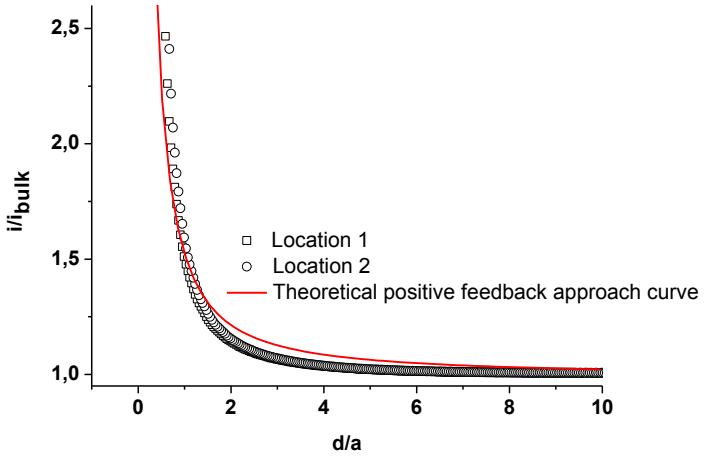

Fig. 5.12*: Approach curves recorded for the sample ecv 1 mM Ag/Naf/GCE in two different locations of the sample.*

[11] A. J. Bard, M. V. Mirkin, *Scanning Electrochemical Microscopy*, Marcel Dekker, Inc, New York, **2001**.

In this case, the approach curves display positive feedback, which agrees with the circumstance that the Ag particles were homogeneously distributed in the sample surface and had a relatively large size. This view is also confirmed by the line scans recorded over a range of 200 µm, that provide responses as those displayed in Fig. 5.13, which denote extensive regions with normalized current higher than 1. This is clearly due to the presence of Ag^0 in the silver particles. On the other hand, the current variations along the scan can be explained as due, in part to the sample topography, which is not completely flat; in part to the fact the amount of Ag^0 directly exposed to the solution may vary from point to point, some of the Ag particles being probably deeply embedded within the Nafion® matrix and not directly accessible to the redox mediator.

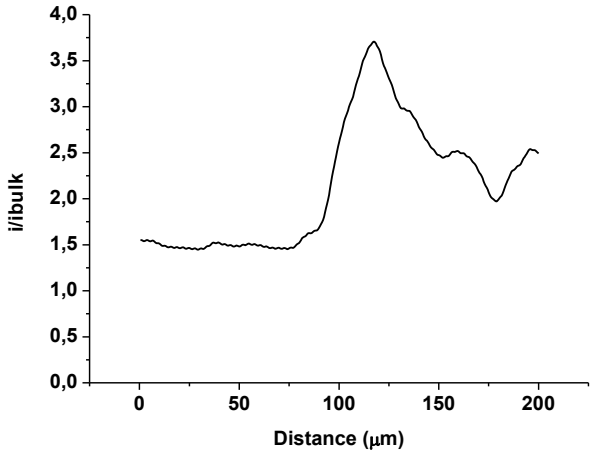

***Fig. 5.13**: Linear scan recorded on the ecv 1mM Ag/Naf/GCE.*

The sample prepared from commercially available silver nanoparticles displayed approach curves shown in Fig. 5.14. In this case, negative feedback responses were always recorded. This suggested that the AgNPs were either deeply buried within the Nafion® matrix or that the Ag in the AgNPs was in an oxidized form and therefore unable to provide the catalytic cycle represented by reactions 1) and 2). Both the latter two hypothesis can be considered.

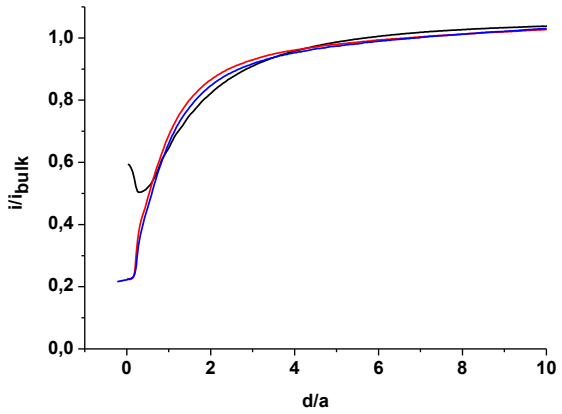

***Fig. 5.14**: Approach curves recorded for c-Ag/Naf/GCE sample in different locations of the GCE modified surface.*

Finally, SECM measurements were performed above the exopolysaccharides loaded with AgNPs (AgNPs-EPS) and Fig. 5.15 and Fig. 5.16 display approach curves recorded at different locations of the same sample and line scan performed above the boundary between glass/AgNPs-EPS.

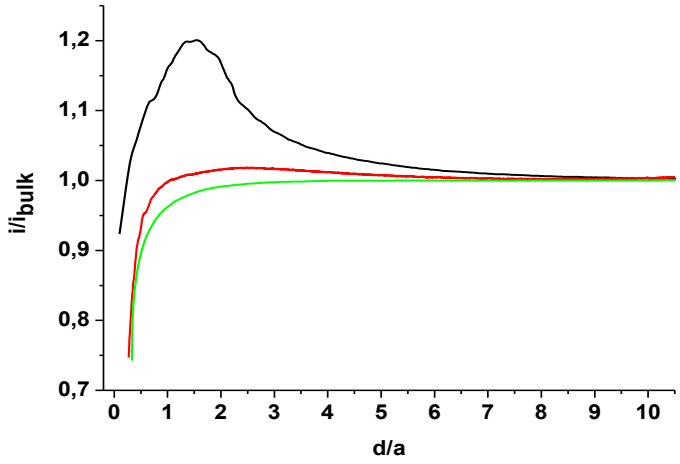

***Fig. 5.15**: Approach curves recorded in different locations of the same AgNPs-EPS sample.*

As is evident in Fig. 5.15, also in this sample approach curves displayed attenuated negative feedback or positive feedback responses, indicating the presence of Ag^0 in the AgNPs. Interesting is to note that the approach curve, which displayed the highest positive feedback manifested a current maximum as the tip approached closer to the substrate. This is explained as due to the complete transformation of the small AgNPs as a consequence of reaction 2). The observed behavior can also be explained considering that the tip can penetrate the soft exopolysaccharide matrix, where the diffusion of the redox mediator is impeded and the lack of Ag^0 forms gives rise to the negative feedback responses.

The distribution of the Ag^0 in the sample was established by line scans and that is displayed in Fig. 5.16 confirming that the AgNPs-EPS sample had large regions containing Ag^0.

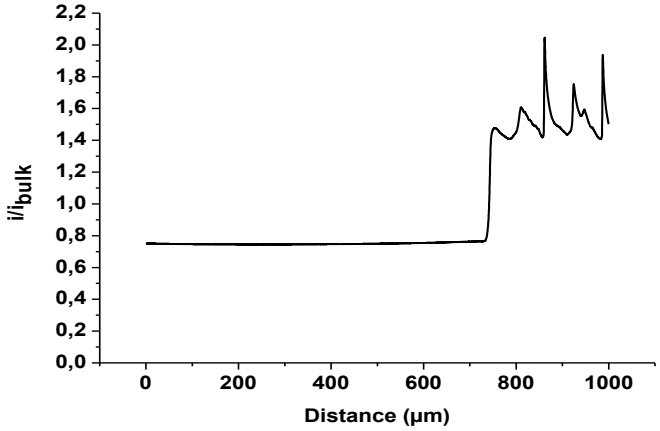

***Fig. 5.16**: Linear scan obtained for AgNPs-EPS sample.*

5.3 Reactivity of silver particles at the substrate/solution interface

In this section, the voltammetric behavior of Ag^+ in water and in hydroalcoholic solutions is investigated to acquire general information concerning the effect of the medium, pH and supporting electrolyte on reduction and oxidation potentials of the Ag^+/Ag^0 system. The media investigated were water, water acidified with acetic acid and water/ethanol mixtures. Specifically: 3% acetic acid; unbuffered aqueous solutions; 10% v/v - 20% v/v and 50% v/v ethanol/milli-Q water mixtures. This choice was related to the circumstance that, according to European Recommendations[12], the above media can be regarded as food simulants in the food packaging industry. All measurements were performed using a platinum disk microelectrode, which was also employed for SECM/ASV determination of silver ions, released at the solid/solution interface of the various samples loaded with silver particles. Since the above simulating media in conventional tests for the Ag^+ release[12,13,14] are employed without addition of electrolytes, voltammetric measurements were also performed in the media with no electrolyte. This was possible thanks to the inherent properties of microelectrodes[15,16,17].

All the media investigated were spiked with 1 mM $AgNO_3$, while, when required, 0.1 M KNO_3 was used as supporting electrolyte. In order to avoid contamination of the solutions with chloride ions, which could come from solution leakage of an Ag/AgCl reference electrode, a platinum wire was used as pseudo-reference electrode.

Typical cyclic voltammograms obtained at low scan rate for Ag^+ reduction in the media cited above without and with supporting electrolyte are shown in Fig. 5.17 A and B, respectively.

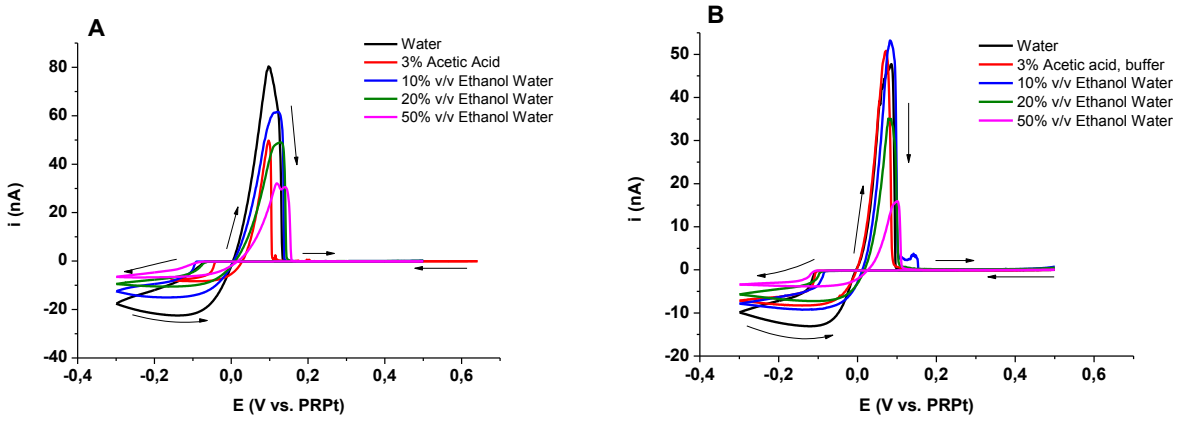

***Fig. 5.17**: Cyclic voltammograms recorded in solution containing 1 mM $AgNO_3$ in different media: (--) water; (--) 3% acetic acid; (--) 10% v/v ethanol/water; (--) 20% v/v ethanol/water; (--) 50% v/v ethanol/water A) in absence of supporting electrolyte and B) in presence of 0.1 M KNO_3. Scan rate 5 mV/s.*

[12] Commission of the European Communities (2011). *Official Journal of the European Union*. Directive EU/10/2011, EC **2011**.
[13] G. Artiaga, K. Ramos, L. Ramos, C. Camara, M. Gomez-Gomez, *Food Chemistry* **2015**, 166, 76-85.
[14] M. Cushen, J. Kerry, M. Morris, M. Cruz-Romero, E. Cummins, *Food Additives & Contaminants: Part A* **2014**, 31(6), 1132-1140.
[15] A. J. Bard, L. R. Faulkner, *Electrochemical Methods*, M. Dekker, New York, **2001**.
[16] S. Daniele, M. A. Baldo, M. Corbetta, G. A. Mazzocchin, *J. Electroanal. Chem.* **1994**, 379, 261-270.
[17] S. Daniele, C. Bragato, M. A. Baldo, *J. Electroanal. Chem.* **1998**, 456, 105-112.

As is evident, the general reduction/oxidation pattern of the Ag^+/Ag^0 couple is not different from that discussed in the previous chapter in section 4.5. In particular, during the forward scan, the current is virtually zero until a sufficiently high overpotential is achieved at which nucleation and growth of the Ag phase onto the Pt surface takes place. The current then increases steeply up to a maximum limiting value. A characteristic nucleation loop is evident on reversal of the sweep followed by the stripping of the deposited metal. Comparison of the cathodic and anodic charges showed that, in general, they were almost equal, in agreement with the occurrence of the following reaction:

$$Ag^+ + e^- \rightleftarrows Ag^0 \qquad (3)$$

However, changing the experimental conditions some peculiar effects arose. These are related to the nucleation potential and the steady state limiting currents, which can affect the processes during both deposition and stripping steps in the procedure adopted for the detection of the Ag^+ released from the silver particles. As for the nucleation potential, in general, it occurs at less negative values in the media with no electrolyte with respect to the fully supported case. This indicates that with low electrolyte, the nucleation process is less affected by kinetic hindering. As for the steady-state limiting current, which is relevant from a quantitative point of view, it varied by changing both the nature of medium and the supporting electrolyte concentration. These effects were related to change of viscosity of the media[16,17] and on migration contribution, as the electroactive species investigated is a charged one[18].

The effect of the viscosity (η) of the media, actually, reflects on the diffusion coefficient D of the electroactive species. It can be accounted for by the Stokes - Einstein equation[19]:

$$D = kT/6D\eta r_h \qquad (5.1)$$

where k is the Boltzmann constant, T is the temperature and r_h is the hydrodynamic radius.

The effect of supporting electrolyte on the current can be corrected by the use of the following equation[16]:

$$i_m/i_d = n+1+2\rho-2[\rho(n+\rho)]^{1/2} \qquad (5.2)$$

where i_m and i_d are the current recorded in the absence and in excess of supporting electrolyte, respectively; $\rho = C_{SE}/C_E$ (C_{SE} and C_E are the concentration of the supporting electrolyte and the electroactive specie, respectively) is the support excess; n is the charge of the electroactive species. In the present case, in the media with no electrolyte, ρ =0 while n = 1, consequently i_m/i_d = 2. I_d is given by:

$$i_d = 4nFDC_Ea \qquad (5.3)$$

[18] S. Daniele, M. A. Baldo, C. Bragato, *Electrochem. Commun.* **1999**, 1, 37-41.
[19] J. O. Bockris, A. K. N. Reddy, *Modern Electrochemistry*, vol. 1, Plenum, New York, **1970**.

Tables 5.3.1 (A-E) summarize steady-state limiting current values and the viscosity of the media investigated. From the experimental steady-state current and considering equations (5.2) or (5.3), for the various situations the diffusion coefficient values for Ag^+ in the different media investigated were evaluated and included in Tables 5.3.1 (A-E).

***Table 5.3.1 A**: Steady-state currents and calculated D_{Ag+} values in water in presence and absence of supporting electrolyte.*

Solvent	*Electrolyte*	*η (cP)*	*i_{ss} (nA)**	*$D\times10^5$ (cm^2/s)**
Water	no	1.000	12.1 (±0.1)	1.47 (±0.01)
Water	0.1 M KNO_3	1.000	7.30 (±0.09)	1.62 (±0.02)

*Standard deviation was obtained from at least three replicates

***Table 5.3.1 B**: Steady-state currents and calculated D_{Ag+} values in 3% acetic acid aqueous solution.*

Solvent	*Electrolyte*	*η (cP)*	*i_{ss} (nA)**	*$D\times10^5$ (cm^2/s)**
Water+3% HAc	no	1.060[20]	7.30 (±0.26)	1.62 (±0.06)
Water+3% HAc	0.04 M AcONa	1.060	6.25 (±0.01)	1.38 (±0.01)

*Standard deviation was obtained from at least three replicates

***Table 5.3.1 C**: Steady-state currents and calculated D_{Ag+} values in 10% v/v ethanol/water solution in presence and absence of supporting electrolyte.*

Solvent	*Electrolyte*	*η (cP)*	*I_{ss} (nA)**	*$D\times10^5$ (cm^2/s)**
10% v/v ethanol/water	No	1.39[20]	9.44 (±0.05)	1.15 (±0.01)
10% v/v ethanol/water	0.1 M KNO_3	1.39	6.31 (±0.01)	1.40 (±0.01)

*Standard deviation was obtained from at least three replicates

***Table 5.3.1 D**: Steady-state currents and calculated D_{Ag+} values in 20% v/v ethanol/water solution in presence and absence of supporting electrolyte.*

Solvent	*Electrolyte*	*η (cP)*	*i_{ss} (nA)**	*$D\times10^6$ (cm^2/s)**
20% v/v ethanol/water	No	1.89[20]	7.51 (±0.05)	9.14 (±0.06)
20% v/v ethanol/water	0.1 M KNO_3	1.89	4.29 (±0.10)	9.50 (±0.03)

*Standard deviation was obtained from at least three replicates

[20] *Handbook of Chemistry and Physics*, 72nd Ed. (Ed.: D. R. Lide), CRC, Boca Raton, **1991-1992**.

***Table 5.3.1 E**: Steady-state currents and calculated D_{Ag+} values in 10% v/v ethanol/water solution in presence and absence of supporting electrolyte.*

Solvent	*Electrolyte*	*η (cP)*	*I_{ss} (nA)**	*$D\times10^6$ (cm^2/s)**
50% v/v ethanol/water	No	2.78[20]	4.88 (±0.11)	5.94 (±0.01)
50% v/v ethanol/water	0.1 M KNO_3	2.78	2.96 (±0.01)	6.55 (±0.02)

*Standard deviation was obtained from at least three replicates

From these tables it is evident that the diffusion coefficient values depend on viscosity and, although to a lesser extent, on whether the media contain or not a supporting electrolyte. However, a simple analysis of the data can be done for the case of water solutions. In fact for this medium, the steady-state limiting current for the reduction of Ag^+ recorded in 0.1 M KNO_3 doubles when the measurements are performed in absence of supporting electrolyte as predicted by Equation (5.2). Also, the value of 1.47×10^{-5} cm^2/s, evaluated here for the diffusion coefficient of Ag^+, agrees well with that reported in a previous work by us[21] and others in the literature[22]. It is obvious that, according to Eq. 5.3, the limiting current increases with D.

As for the effect of viscosity, from Tables 5.3.1 (A-E) it is evident that the increase of ethanol in the water/ethanol mixtures provides an increase of viscosity up to the highest value at 50% (v/v)[18]. This reflects on the limiting current and consequently on the diffusion coefficient. Interesting is to note that in the water/ethanol media, the current in the absence of supporting electrolyte does not double that in 0.1 M KNO_3. This may be due to the fact that, other than the viscosity, the increase of alcohol content may cause a decrease of dielectric constant of the medium and this, in turn, can lead to the formation of ionic couples that shield the charge of silver ions.

A situation similar to that described above can also occur for the case of the acetic acid media. For the latter case, in addition, the charge of Ag^+ can be shielded by the formation of silver/acetate complexes[16]. These aspects, however, were not further investigated here.

Finally, in order to verify whether the diffusion coefficient values obtained in the different media obey the Stokes-Einstein relationship (Eq. 5.1), a plot of *D vs. 1/η* was constructed, as displayed in Fig. 5.18. In the figure black symbols refer to values evaluated in absence of supporting electrolyte, while red symbols refer to those obtained in the electrolyte supported media.

[21] D. Battistel, G. Pecchielan, S. Daniele, *ChemElectroChem* **2014**, 1, 140-146.
[22] S. Kariuki, H. D. Dewald, *Electroanalysis* **1996**, 8, 307-313.

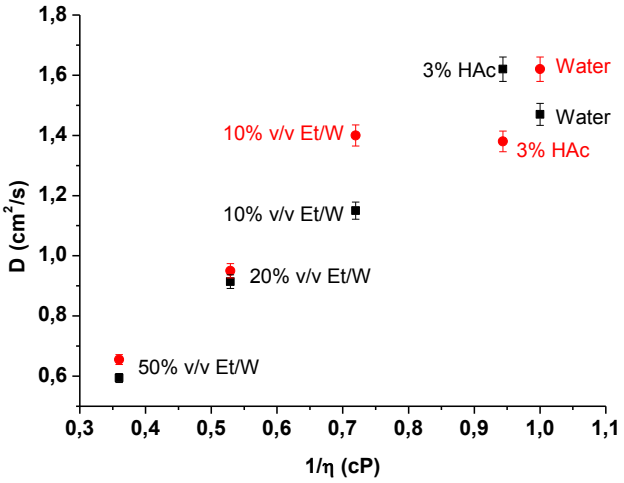

***Fig. 5.18**: Diffusion coefficient vs. viscosity plot. Black (▪) and red (●) symbols refer to values recorded in absence of supporting electrolyte and 0.1 M KNO_3 respectively. Error bar refers to three replicates.*

From the figure it is evident that, in general, diffusion coefficients correlate satisfactorily with 1/η. Major discrepancies arise in the measurements performed in acetic acid media. This further supports the possibility of complexation reactions between Ag^+ and acetate ions.

5.4 Study of the release of Ag^+ from the Ag^0-loaded samples

The antimicrobial activity of silver compounds is generally attributed to Ag(I) species[23,24]. These can be released from micro- and nano-particles to an extent that depends on particles reactivity. The phenomena involved occur at the substrate/solution interface and can be studied by performing localized measurements by SECM coupled with a sensitive voltammetric technique able to quantify even very low concentrations of Ag(I) specie. This approach was employed to establish reactivity, in terms of amounts of Ag(I) released, of the Ag-loaded samples prepared as described in the previous section. In particular, SECM in proximity mode (see scheme in Fig. 5.19), coupled with anodic stripping or cyclic voltammetry was employed. Using CV in a proper potential window, both Ag(I) or Ag(0) forms within the microelectrode-substrate gap could be revealed and quantified.

[23] N. Hadrup, H. R. Lam, *Regul. Toxicol. Pharmacol.* **2014**, 68, 1-7.
[24] Z-M. Xiu, Q.-B. Zhang, H. L. Puppala, V. L. Colvin, P. J. J. Alvarez, *Nano Lett.* **2012**, 12(8), 4271-4275.

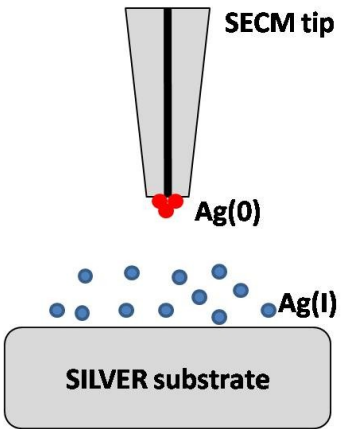

***Fig. 5.19**: Scheme of SECM mode for Ag(I) quantification in the proximity of the substrate.*

In the experimental procedure employed for this study, the microelectrode was initially positioned at a given distance from the substrate by the help of the K_3IrCl_6 redox mediator. Afterward, series of either CVs or ASVs were performed over the potential range -0.2 – 0.6 V *vs.* Ag/AgCl in which suspended colloidal Ag^0 containing particles or Ag(I) soluble species could be oxidized or reduced, respectively. Diffusion profiles of the Ag(I) species from the sample surfaces towards the bulk solutions were also investigated.

For the quantifications of Ag(I) released, two different strategies were used, both based on the charge involved during the CVs or ASVs steps. This depended on the tip-substrate distance (*h*). When it was lower than 10 times the microelectrode radius, the Ag(I) released was estimated assuming that the volume of solution involved was that of the cylinder (V_{cil}) formed between the microelectrode and the substrate, with a basal radius equal to that of the overall SECM tip (including the microdisk and the insulating; see scheme in Fig. 5.20)[25]:

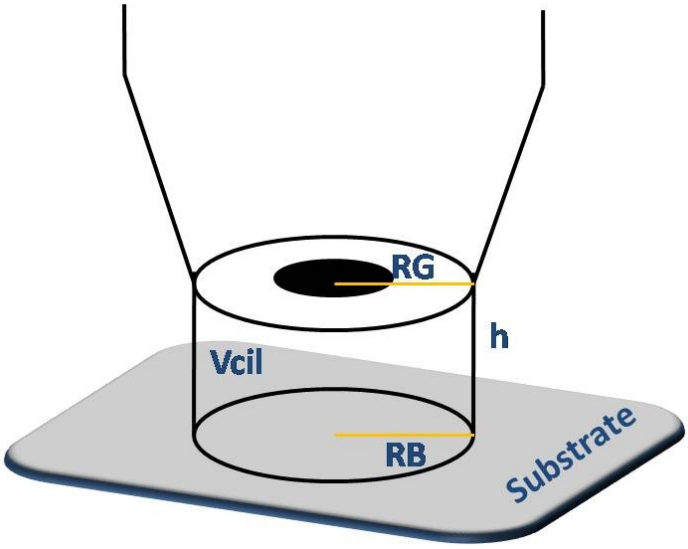

***Fig. 5.20**: Scheme of the diagram for the volume considered for the calculation of the concentration of Ag(I).*

[25] C. Kranz, G. Wittstock, H. Wohlschlager, W. Schuhmann, *Electrochim. Acta* **1997**, 42, 3105-3111.

For example, for a *RG* = 8 and *a* = 13 μm, the basal radius is *RB* = 100 μm; assuming *h* = 5, V_{cil} = 1.57×10^{-10} dm^3. The number of moles (*N*) associated with the charge (*Q*) of the CV or ASV peaks was calculated on the basis of the Faraday's law:

$$N = Q/nF \quad (5.4)$$

where *n* is the number of electrons involved in the process. Therefore, silver ions concentration is given by:

$$C = N/V_{cil} \quad (5.5)$$

When *h* was larger than 10 times the microdisk radius, the concentration of Ag(I) was low and only ASV was enough sensitive for its quantification. In these cases, a procedure already reported in Refs. 26 and 27 was employed[26,27]. In particular, *N* accumulated onto the Pt microdisk surface is given by:

$$N = 1.13AD^{½}C_b t_{d,eff}^{½} + kaDC_b t_{d,eff} \quad (5.6)$$

where *A* is the microelectrode surface area $t_{d,eff}$ is the effective deposition time. The electrical charge, Q_c, involved during the metal ion deposition is given by

$$Q_a = nFN \quad (5.7)$$

Assuming that:

$$Q_a = Q_c \quad (5.8)$$

where Q_a is the charge involved during the stripping step, and combining Eqs. 5.4 – 5.8 yields:

$$Q_a = nFN = nFC_b\,[1.13A\,(Dt_{d,eff})^{1/2} + kaDt_{d,eff}] \quad (5.9)$$

Thus, from Eq.(5.9) and the experimental stripping charge involved in the metal oxidation, the bulk concentration of Ag(I) could be determined, provided that the other parameters were known. As for the parameters *k* and *a*, they were obtained on an experimental basis, as described in Refs.25 and 26. As for the diffusion coefficient of Ag(I), those reported in Tables 5.3.1 (A-E) found for the different media investigated were employed. Finally, as for the concentration profiles of Ag(I), unless otherwise stated, the distance range from 5 μm above the substrate up to 5000 μm towards the bulk solution was examined.

[26] M. S. Abdelsalam, G. Denuault, S. Daniele, *Anal. Chim. Acta* **2002**, 452(1), 65-75.
[27] M. A. Baldo, S. Daniele, M. Corbetta, G. A. Mazzocchin, *Electroanalysis* **1995**, 7, 980-986.

5.4.1 Activity of bulk silver

Preliminarily, in order to compare data obtained with the synthesizes Ag-loaded samples with those that could be expected for bulk silver, a series of measurements for the Ag(I) release was performed using a conventional silver disk electrode as substrate. In this case, the SECM-ASV investigation could be performed by keeping the Ag substrate either at open circuit (OCP), where only spontaneous corrosion could take place, or at a constant potential where substantial amount of silver ions could be produced by "forced" oxidation.

Fig. 5.21 shows a series of CVs recorded with the Pt microelectrode positioned at 5 µm above the silver electrode, while it was either unbiased or biased at 0.2 and 0.4 V *vs.* Ag/AgCl; the sample was immersed in a solution containing 0.1 M KNO_3. The CVs were performed at 50 mV/s, starting from 0.7 V and scanning the potential towards negative values. From the figure it is evident that no process due to the Ag^+/Ag system is observed at OCP or when the substrate was biased at 0.2 V. Instead, a reduction peak in the forward scan, typical for thin layer behavior, and a more complex oxidation peak in the backward scan are observed, when the Ag electrode is biased at 0.4 V. This indicates that, under these conditions, relatively high Ag(I) amounts were formed at the Ag electrode surface. Similar experiments performed in the various aqueous or hydroalcoholic matrices provides similar results (see also below). These results were useful to establish at which potentials soluble Ag(I) species, formed at the substrate/solution interface, could be reduced, or Ag^0-containing particles, eventually detached from a surface, could be oxidized.

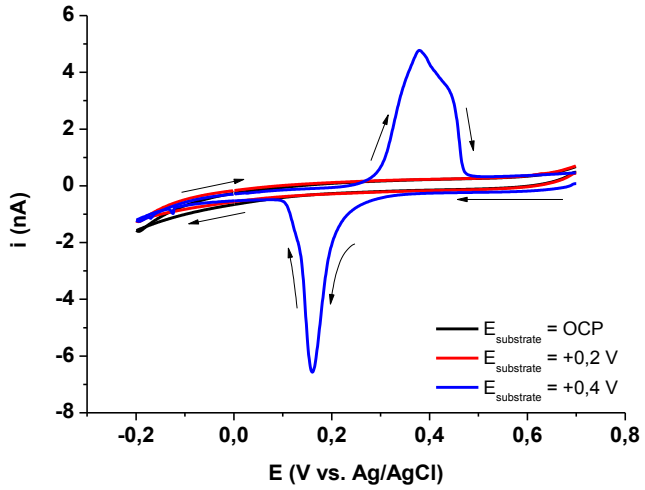

Fig. 5.21*: Cyclic voltammograms recorded in 0.1 M KNO_3 aqueous solution by applying at the silver disk-electrode substrate different potentials: (--) OCP, (--) 0.2 V and (--) 0.4 V vs. Ag/AgCl. Tip/substrate distance 5 µm; scan rate 50 mV/s.*

In all media investigated and biasing the Ag substrate at 0.4 V, SECM-CVs measurements were performed with the microelectrode positioned at different distances above the substrate, and (Fig. 5.22) shows typical CVs obtained.

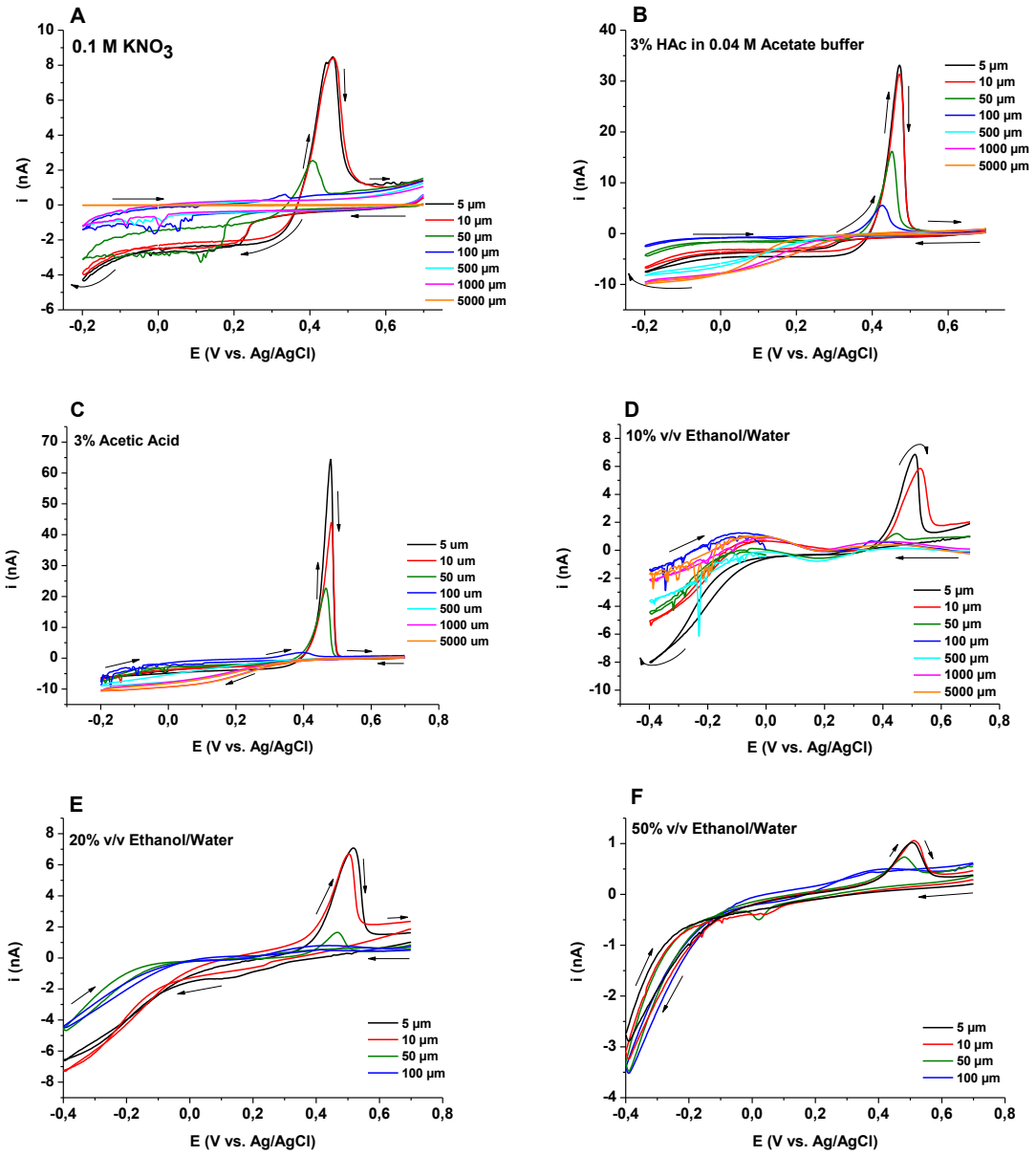

***Fig. 5.22**: Cyclic voltammograms recorded in A) 0.1 M KNO_3, B) 3% acetic acid + 0.04 M acetate buffer, C) 3% acetic acid, D) 10% v/v ethanol/water, E) 20% v/v ethanol/water and F) 50% v/v ethanol/water. Tip-substrate distances as indicated; $E_{substrate}$ = + 0.4 V vs. Ag/AgCl; scan rate 50 mV/s.*

As is evident, both the reduction and stripping processes, due to the Ag^+/Ag^0 system, occur over potential ranges, which are fully congruent (after correction for the different reference electrodes employed) with those recorded in section 5.3 for $AgNO_3$ dissolved in the bulk solutions.

Also, the shape of the peaks and currents involved in both the reduction and oxidation processes, at a given tip-substrate distance, reflect to some extent the properties of the media investigated. For instance, in acidic aqueous media, the peaks are generally sharper and better defined, with respect to those obtained in neutral or hydroalcoholic solutions. Moreover, the current intensity reflect to some extent the viscosity of the media, both reduction and oxidation peaks being the larger for lower viscosity. These results are also consistent with the observations

made before for the voltammetric behavior of Ag^+ ions in different solvents investigated. As for the current responses of both reduction and oxidation processes, as expected, they decrease as the tip-substrate distance increases, up to the background current, when the tip-substrate distance is larger than about 100 µm. This clearly reflects the diffusion profiles and mobility of Ag^+, formed at the substrate surface during its polarization period (*i.e.* overall about 35 s), towards the bulk solution.

As for the activity of bulk silver, even with the biased substrate, it varies upon varying the medium investigated. This is apparent from data shown in (Fig. 5.23), which displays the concentration profiles of Ag(I) released from the Ag substrate. At the closest tip-substrate distance examined (*i.e.* 5 µm), the concentration of Ag(I) released (see Table 5.4.1) is the largest in the 3% acetic acid solution, probably because of a faster kinetic dissolution of silver. On the other hand, it is the lowest in the 50% v/v water/ethanol mixture, conceivably due to adsorption of ethanol onto the Ag substrate, which could lead to a partial passivation of the surface. It must be considered that the concentration values were evaluated with the methods described in the previous section, which accounts for, through the diffusion coefficient utilized, the change of viscosity of the media and its effect on Ag^+ mobility.

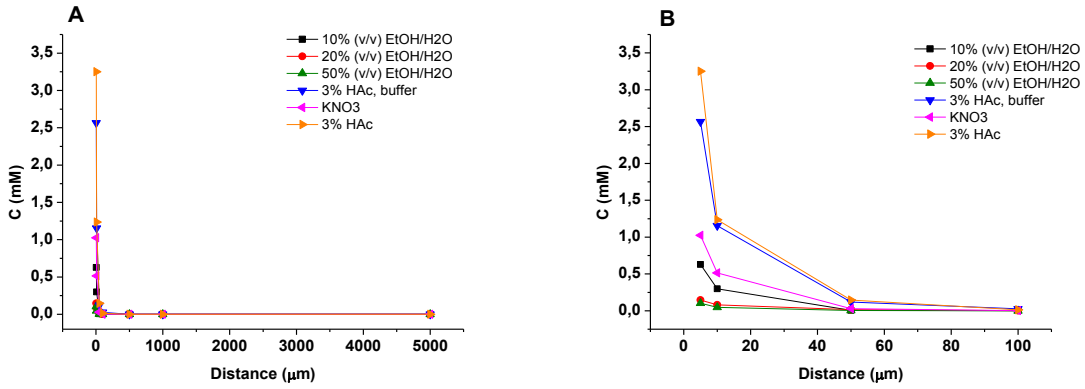

Fig. 5.23*: A) Ag(I) concentration profile at the Ag/solution interface of the solutions and B) expanded plot. The substrate was biased at + 0.4 V. The charge employed for quantification was that involved in the stripping step of the CVs recorded in the solutions A, B, C, D, E, F of Fig. 5.22.*

Table 5.4.1*: Concentration of Ag(I) released at 5 µm with silver electrode biased at + 0.4 V vs. Ag/AgCl.*

Solvent	*Concentration (mM)*
3 % Acetic acid	3.25
3% Acetic acid, buffer	2.57
0.1 M KNO_3	1.02
10% v/v $EtOH/H_2O$	0.63
20% v/v $EtOH/H_2O$	0.15
50% v/v $EtOH/H_2O$	0.10

5.4.2 Activity of unbiased bulk silver

The activity of an unbiased bulk silver substrate was also investigated, using an approach similar to that employed in section 5.4.1. Under these conditions, the release of Ag(I) at the substrate/solution interface could only occur through the spontaneous corrosion of the metal caused by oxygen present in the air saturated media. Since the amount of Ag(I) formed at the substrate/solution interface was expected to be very low and to obtain reliable concentration data, ASV was employed as the most suitable voltammetric technique coupled to SECM. In the ASV measurements, the parameters summarized in Table 5.4.2 were employed. The linear sweep voltammetry was the wave form utilized during the stripping step. Moreover, the release of silver ion was studied by varying the immersion time of the samples in the various solutions from 30 minutes up to few hours (*i.e.*, 5 - 6 h).

***Table 5.4.2**: Optimized stripping parameters for a bulk silver substrate.*

Parameter	***Value***
$\mathbf{E_{accumulation}}$	-0.2 V *vs*. Ag/AgCl
$\mathbf{t_{accumulation}}$	300 s
Stripping scan rate	50 mV/s
$\mathbf{E_{window}}$	-0.2 /+0.5 V *vs*. Ag/AgCl
Tip/Substrate Distances	5-5000 µm

Fig. 5.24 shows typical ASVs obtained in the different solutions a few minute after the introduction of the solution in the cell (t_0 in Fig. 5.24) and after 300 min the samples were immersed in the same solutions, over the range of tip-substrate distances examined.

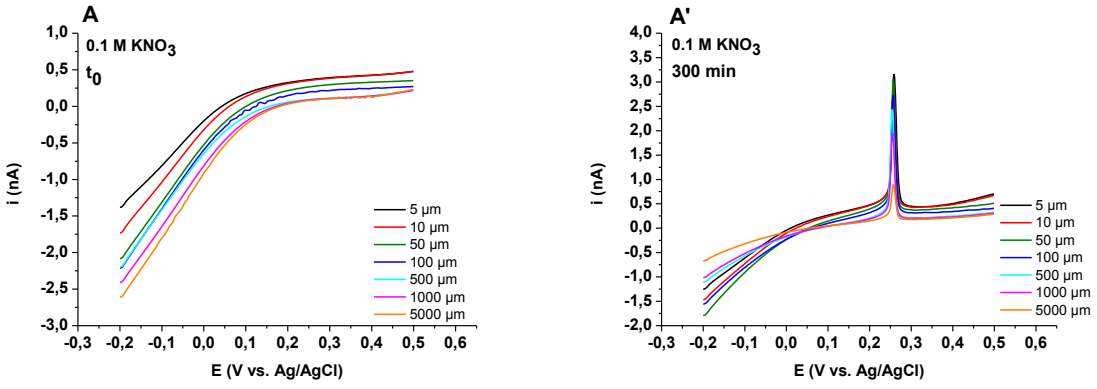

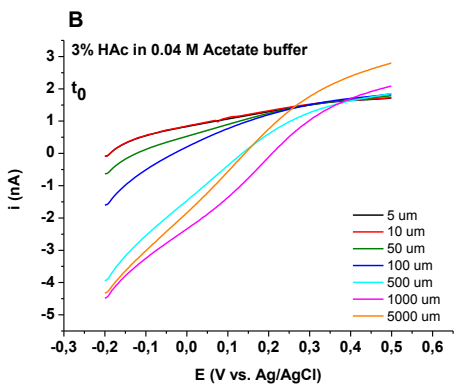
B
3% HAc in 0.04 M Acetate buffer
t_0
i (nA)
E (V vs. Ag/AgCl)
5 um
10 um
50 um
100 um
500 um
1000 um
5000 um

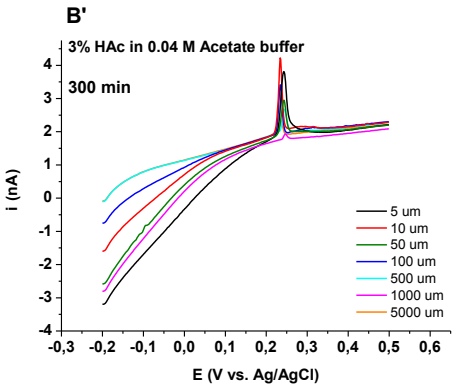
B'
3% HAc in 0.04 M Acetate buffer
300 min
i (nA)
E (V vs. Ag/AgCl)
5 um
10 um
50 um
100 um
500 um
1000 um
5000 um

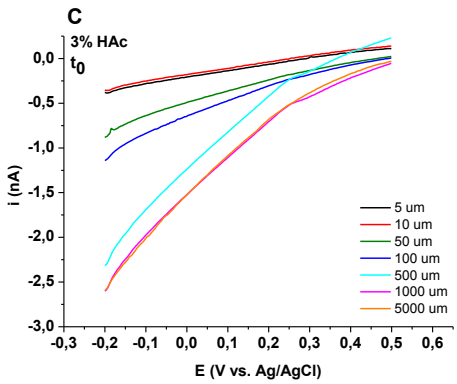
C
3% HAc
t_0
i (nA)
E (V vs. Ag/AgCl)
5 um
10 um
50 um
100 um
500 um
1000 um
5000 um

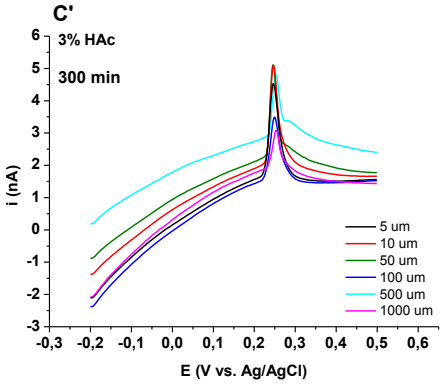
C'
3% HAc
300 min
i (nA)
E (V vs. Ag/AgCl)
5 um
10 um
50 um
100 um
500 um
1000 um

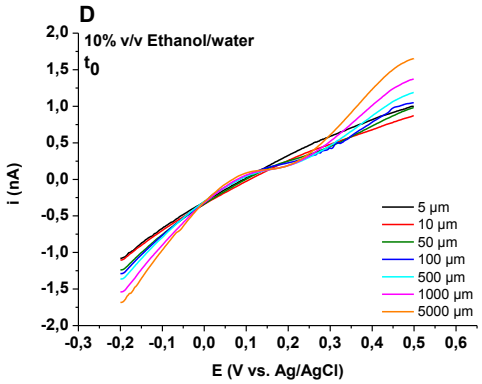
D
10% v/v Ethanol/water
t_0
i (nA)
E (V vs. Ag/AgCl)
5 µm
10 µm
50 µm
100 µm
500 µm
1000 µm
5000 µm

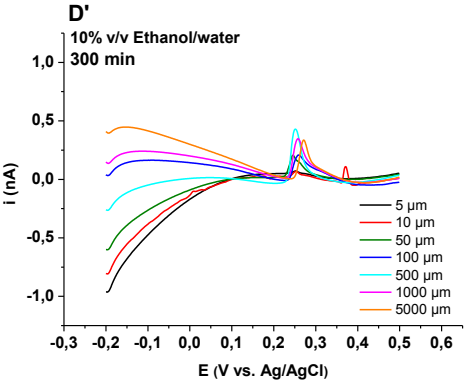
D'
10% v/v Ethanol/water
300 min
i (nA)
E (V vs. Ag/AgCl)
5 µm
10 µm
50 µm
100 µm
500 µm
1000 µm
5000 µm

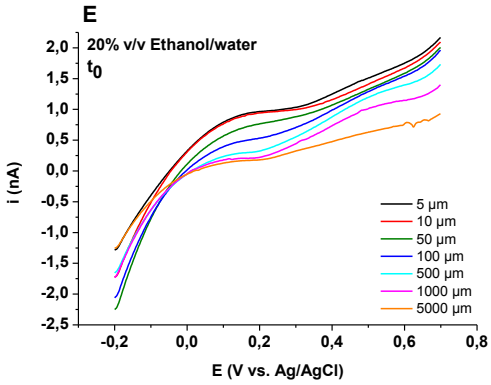
E
20% v/v Ethanol/water
t_0
i (nA)
E (V vs. Ag/AgCl)
5 µm
10 µm
50 µm
100 µm
500 µm
1000 µm
5000 µm

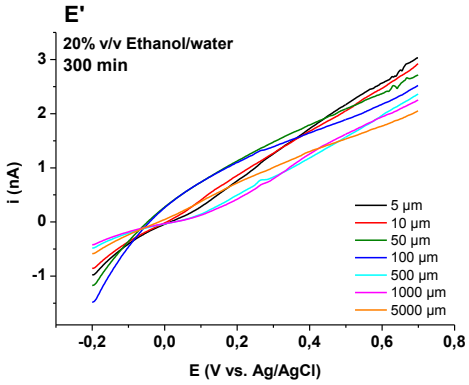
E'
20% v/v Ethanol/water
300 min
i (nA)
E (V vs. Ag/AgCl)
5 µm
10 µm
50 µm
100 µm
500 µm
1000 µm
5000 µm

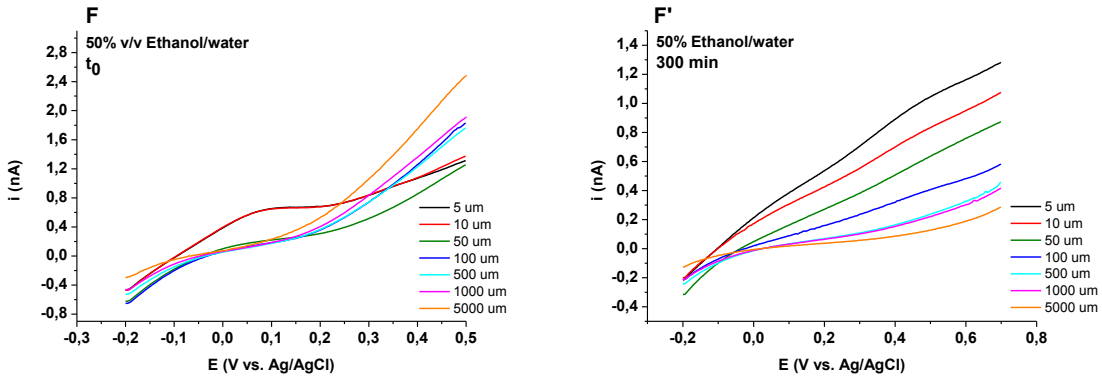

***Fig. 5.24**: ASVs recorded above Ag bulk substrate immersed in A) 0.1 M KNO_3, B) 3% acetic acid in acetate buffer, C) 3% acetic acid solution, D) 10% - E) 20% - F) 50% v/v ethanol/water mixtures; A-F) a few min after the introduction of the solution in the cell and A'-F') after five hours. Tip-substrate distances as indicated; stripping scan rate 50 mV/s.*

As is evident, in this case, in all media investigated, no ASV peak due to the Ag(I) is observed soon after the samples had been immersed in the solution. Sensible, *i.e.* measurable amounts of Ag(I) were recorded at the interface in most media examined after 300 min. The release of Ag^+ was in any case negligible in the 20% and 50% v/v media under the employed conditions. It must be noticed that in the acidic media, stripping peaks that emerged from the background could be recorded after about 120 min immersion time.

The current intensity of the ASV peaks followed same scheme as that depicted in the previous case for the biased substrate, being larger the closer the tip-substrate distance was, as expected. The concentration profiles are displayed in Fig. 5.25. Evidently, also under these conditions the distance at which sensible amounts of Ag(I) could be detected was within about 100 µm. Moreover, at the closest distance (*i.e.*, 5 µm), the Ag(I) concentration was an order of magnitude lower than that recorded in the same media when the substrate was biased (Table 5.4.1).

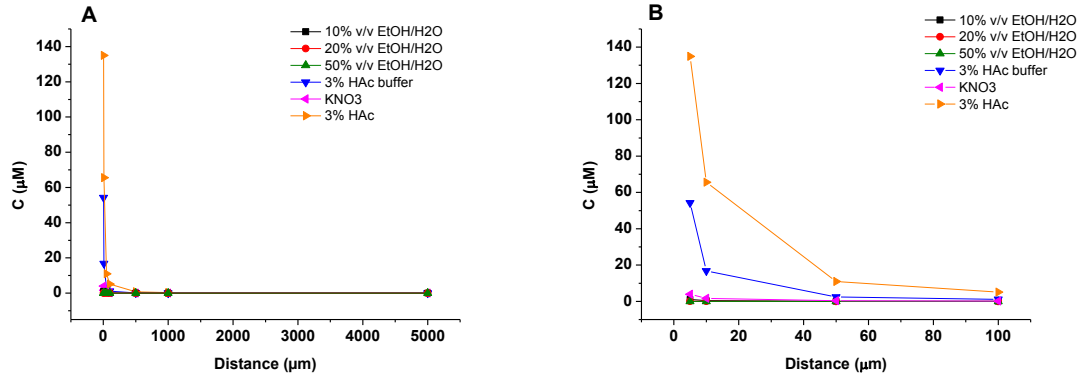

***Fig. 5.25**: A) Ag(I) concentration profile relative to the ASV of Fig. 5.24 B) and expanded plot.*

***Table 5.4.3**: Concentration of Ag(I) released, evaluated at 5 µm after 300 min of immersion of an Ag bulk substrate in the indicated media and for an accumulation time of 300s.*

Solvent	*Concentration (µM)*
3% Acetic acid	135
3 % Acetic acid, buffer	54.3
0.1 M KNO_3	4.00
10% v/v $EtOH/H_2O$	1.10
20% v/v $EtOH/H_2O$	0.082
50% v/v $EtOH/H_2O$	-

5.4.3 Release of Ag^+ from Ag particles embedded in Nafion® films

Ag particles prepared by chemical reduction

The study of Ag(I) released from silver particles, which were obtained by chemical reduction with formaldehyde, was performed by SECM-ASV using the experimental parameters summarized in Table 5.4.4:

***Table 5.4.4**: Optimized stripping parameters for measuring Ag(I) from silver particles embedded in polymeric matrices.*

Parameter	*Value*
$E_{accumulation}$	-0.2 V *vs*. Ag/AgCl
$T_{accumulation}$	**120 s**
Stripping scan rate	50 mV/s
E_{window}	-0.2 /+0.5 V *vs*. Ag/AgCl
Tip/Substrate Distances	5-5000 µm

In this case, because of the expected higher activity of the silver deposits[28,29], the accumulation time, adopted during the pre-concentration step in ASV, was much lower than that required for the bulk silver samples. Moreover, due to the solubility of the Nafion® film in hydroalcoholic mixtures, the release of silver ions were investigated only in 0.1 M KNO_3 aqueous solutions.

[28] S. Horikoshi, N. Serpone, *Microwaves in Nanoparticle Synthesis. Fundamentals and Applications*, Wiley, New York, **2013**.
[29] C. Beer, R. Foldbjerg, Y. Hayashi, D. S. Sutherland, H. Autrup, *Toxicol. Lett.* **2012**, 208(3), 286-292.

Fig. 5.26 shows typical ASVs obtained for the sample prepared starting from 1 mM $AgNO_3$, after 30 min and 360 min immersion in the solution. Fig. 5.27 displays the concentration profiles for a more complete range of immersion time.

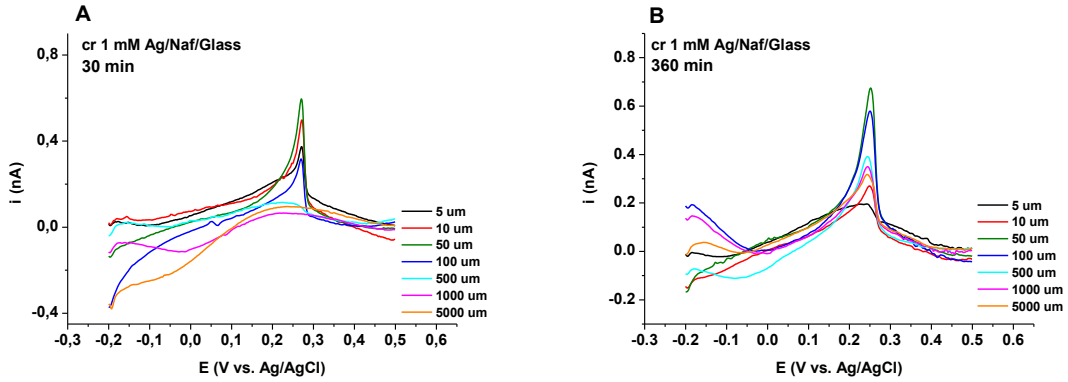

***Fig. 5.26**: ASVs recorded above the cr 1 mM Ag/Naf/glass sample immersed in a 0.1 M KNO_3 aqueous solution. A) immersion time 30 min and B) immersion time 360 min. Tip-substrate distances as indicated. Stripping scan rate 50 mV/s.*

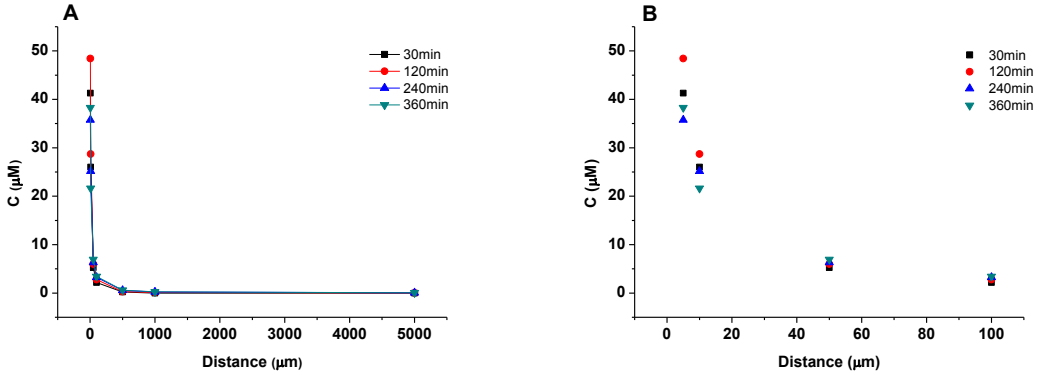

***Fig. 5.27** A) Ag(I) concentration profile relative to the sample cr 1mM Ag/Naf/glass and B) expanded plot.*

As is evident, also in this case the concentration profiles do not extend further than about 100 µm from the sample and almost overlap, regardless the immersion time. This suggests the achievement of a steady-state Ag(I) release kinetic. For this sample, it is likely that Nafion®, being a cation exchanger membrane, could provide local equilibria with the Ag^+ that forms from the Ag^0 silver particles. Therefore, the Nafion® membrane can act, to some extent, as a buffer for the Ag^+ release in the water solution. In any case, the higher silver particles activity provided a silver ion concentration of 3.8×10^{-5} mol/L at 5 µm tip-substrate distance, after about 6 hours immersion of the sample. The evaluated concentration was almost an order of magnitude larger than that provided by bulk silver in the same electrolyte.

Similar considerations can be drawn from the SECM-ASV measurements performed for the sample prepared starting from 50 mM $AgNO_3$ (cr 50 mM Ag/Naf/glass). SECM-ASVs responses and concentration profiles are displayed in Figs. 5.28 and 5.29, respectively. The maximum Ag(I)

concentration, evaluated at 5 µm above the substrate after 6 hours immersion, was 1.21×10^{-4} mol/L, congruently with a larger density of silver particles embedded in the sample.

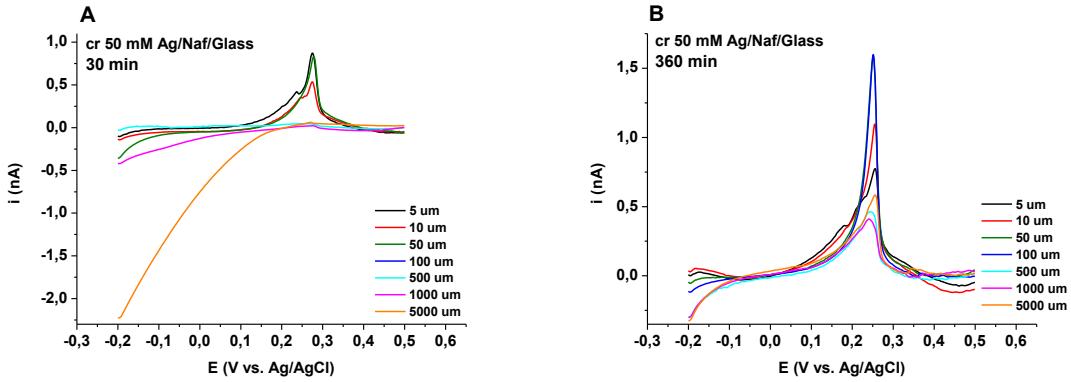

***Fig. 5.28**: ASVs recorded above the cr 50 mM Ag/Naf/glass sample immersed in a 0.1 M KNO_3 aqueous solution. A) immersion time 30 min and B) immersion time 360 min. Tip-substrate distances as indicated. Stripping scan rate 50 mV/s.*

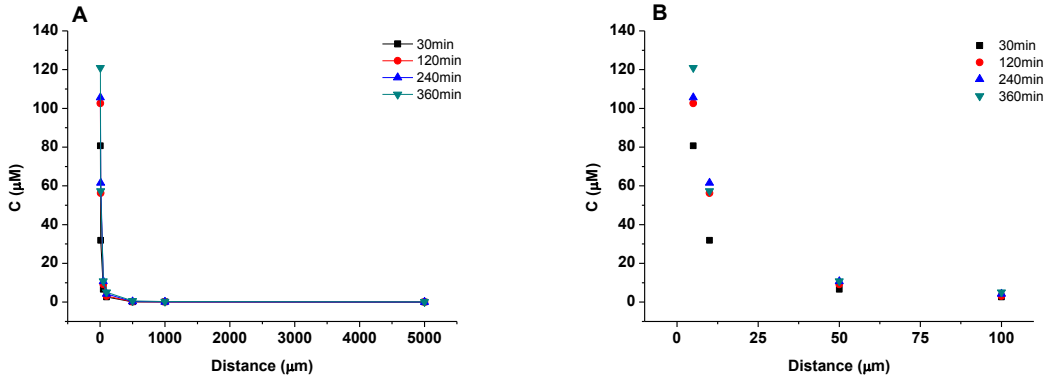

***Fig. 5.29**: A) Ag(I) concentration profile relative to the cr 50 mM Ag/Naf/glass and B) expanded plot.*

Silver particles reduced electrochemically

The SECM-ASV study for Ag(I) release for the ecv 1 mM Ag/Naf/GCE sample was performed using the same conditions reported in Table 5.4.4.

Figs. 5.30 and 5.31 show typical SECM-ASVs responses and relevant concentration profiles, respectively. The maximum Ag(I) concentration recorded at 5 µm above the substrate after immersion for 5 hours was 9.8×10^{-6} mol/L, which compare with the concentration found for the Nafion® sample prepared from 1 mM $AgNO_3$ solution and Ag^+ reduced chemically.

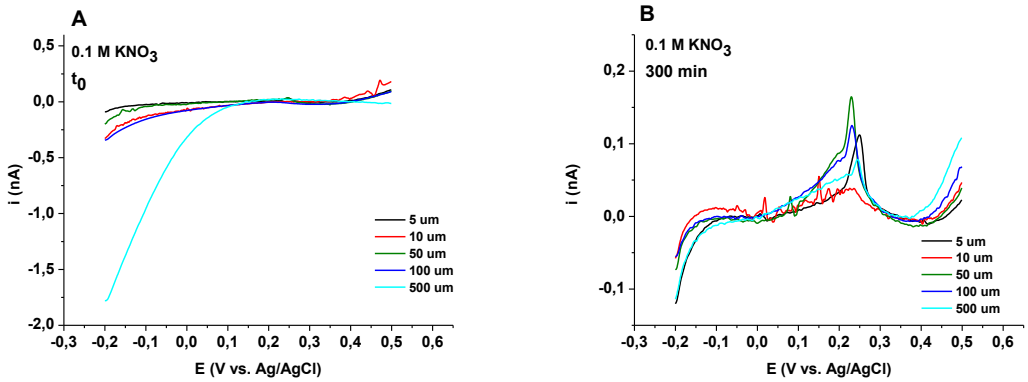

***Fig.5.30**: ASVs recorded above the ecv 1 mM Ag/Naf/GCE sample immersed in a 0.1 M KNO_3 aqueous solution. A) few min after the immersion and B) immersion time 300 min. Tip-substrate distances as indicated. Stripping scan rate 50 mV/s.*

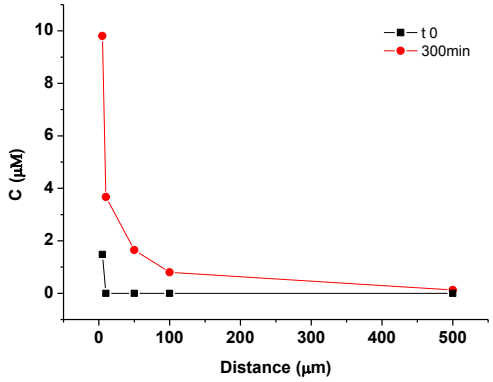

***Fig. 5.31**: Ag(I) concentration profile of the ecv 1mM Ag/Naf/GCE sample.*

Sample prepared from commercially available AgNPs

Also for these samples, SECM-ASV measurements were performed employing the conditions of Table 5.4.4, and using 0.1 M KNO_3 and 3% acetic acid + 0.04 M acetate buffer aqueous solutions. SECM-ASV responses are displayed in Figs. 5.32 – 5.33.

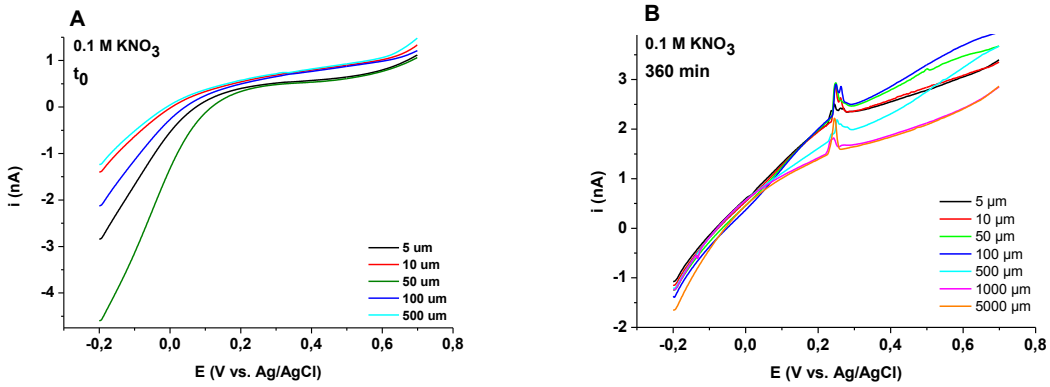

***Fig. 5.32**: ASVs recorded above the c-Ag/Naf/GCE sample immersed in a 0.1 M KNO_3 aqueous solution. A) few min after the immersion and B) immersion time 360 min. Tip-substrate distances as indicated. Stripping scan rate 50 mV/s.*

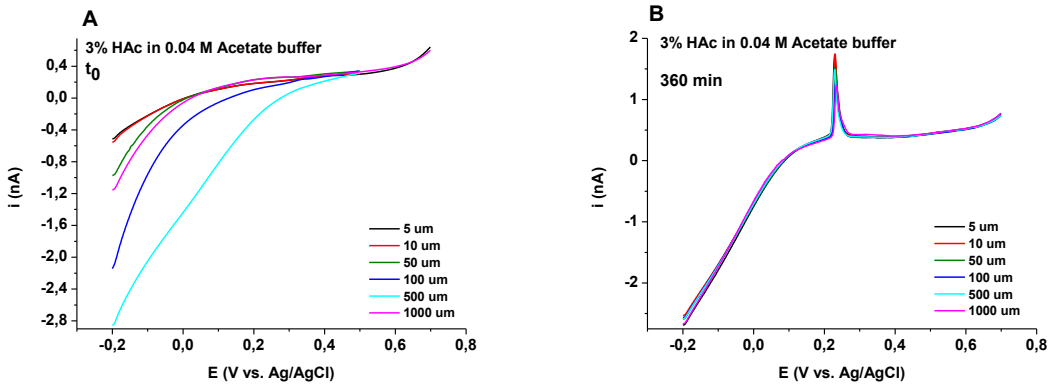

***Fig. 5.33** ASVs recorded above the c- Ag/Naf/GCE sample immersed in 3% acetic acid + 0.04 M acetate buffer aqueous solution. A) few min after the immersion and B) immersion time 360 min. Tip-substrate distances as indicated. Stripping scan rate 50 mV/s.*

As is evident at t_0, no ASV peak was obtained, regardless of the tip-substrate distance. Instead, unexpectedly, after 360 min immersion time, measurable amounts of Ag(I) species were recorded at all distances. Moreover, the ASV peaks decreased as the tip-substrate distance decreased. This is contrary to what observed with all other samples investigated. The different behavior was explained considering that the AgNPs in the c-Ag/Naf/GCE sample are mainly present in an oxidized form (see section 5.2 page 61). This can lead to a faster release of Ag(I) at the sample solution interface and consequently to a general higher amounts of Ag(I) diffusing towards the bulk. This process, for long immersion times, conceivably, brings about the achievement of a homogeneous Ag(I)-soluble species in the solution above the sample (generally 1 mL). From this point of view, the observed decreasing trend of the ASV peaks, as the SECM tip gets closer to the substrate, can be associated to hindered diffusion of Ag(I) from the bulk medium towards the tip electrode surface during the accumulation step (*i.e.*, like a negative feedback effect). By assuming that a uniform concentration of Ag(I) builds within the entire volume of the solution after 360 min immersion of the sample, Eq. 5.9 can be applied to estimate the Ag(I) released from the c-

Ag/Naf/GCE sample, using the charge of the ASV peaks recorded at sufficiently long distances, where the hindering effect due to the sample is negligible. In this way, concentration values of 4.86 $x10^{-8}$ mol/L and 3.42 x 10^{-7} mol/L in 0.1 M KNO_3 and in 3% acetic acid + 0.04 M acetate buffer solution, respectively, were evaluated. The higher concentration of Ag(I) in the acidic medium agrees with expectation.

5.4.4 Ag(I) release from AgNPs-EPS

The EPS is insoluble in alcohol and other organic solvents, except dimethylsufoxide and formamide. Thus, it was possible to evaluate Ag(I) released from the AgNPs-EPS samples in the hydroalcoholic mixtures.

Figs. 5.34 , 5.36 and 5.38 display typical SECM-ASV responses recorded in 10% v/v, 20% v/v and 50% v/v ethanol/water mixtures respectively, while in Figs. 5.35, 5.37 and 5.39 show the relative concentration profiles of Ag(I) released.

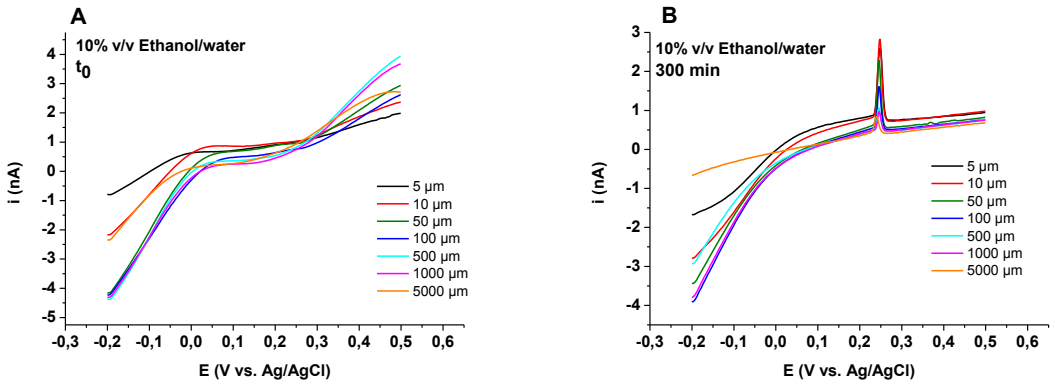

Fig. 5.34: *ASVs recorded above the AgNPs-EPS sample immersed in 10% v/v ethanol/water hydroalcoholic solution. A) few min after the immersion and B) immersion time 300 min. Tip-substrate distances as indicated. Stripping scan rate 50 mV/s.*

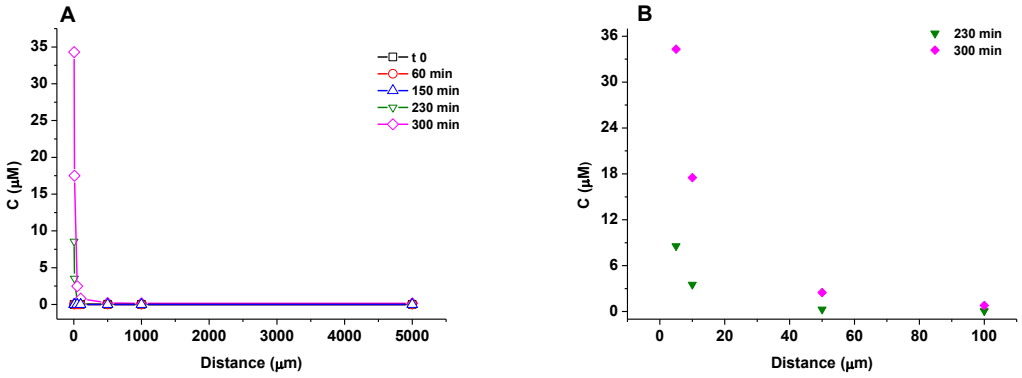

Fig. 5.35: *A)*: *Ag(I) concentration profile relative to the AgNPs-EPS B) and expanded plot.*

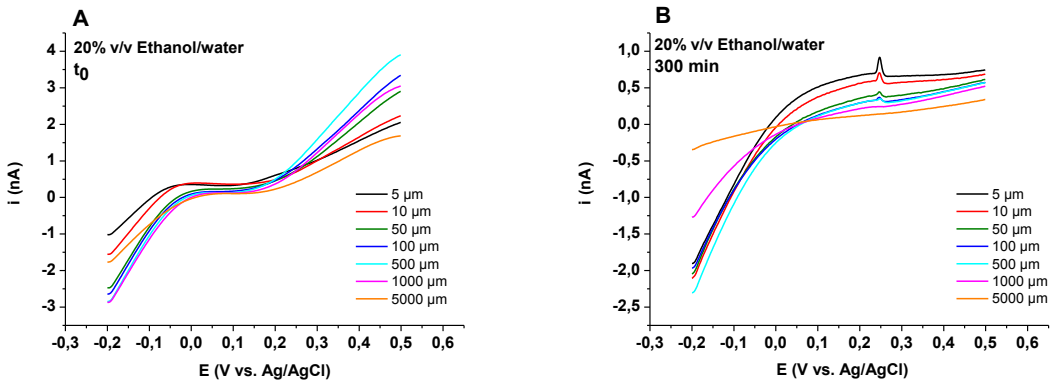

***Fig. 5.36**: ASVs recorded above the AgNPs-EPS sample immersed in 20% v/v ethanol/water hydroalcoholic solution. A) few min after the immersion and B) immersion time 300 min. Tip-substrate distances as indicated. Stripping scan rate 50 mV/s.*

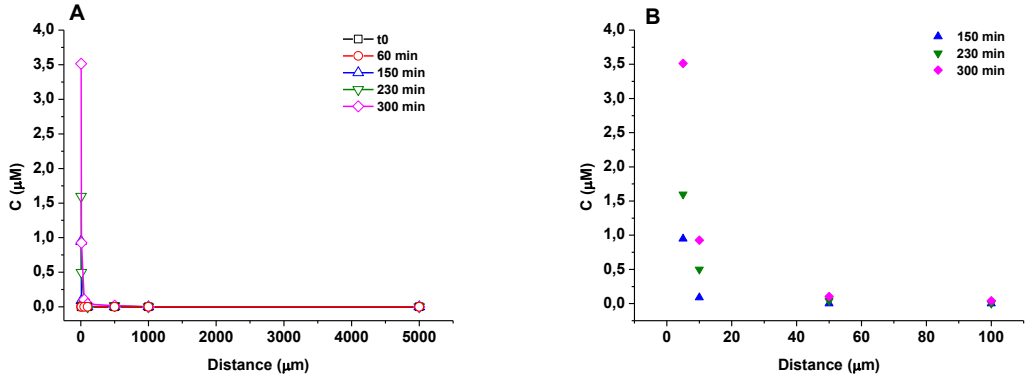

***Fig. 5.37**: A) Ag(I) concentration profile relative to the AgNPs-EPS and B) expanded plot.*

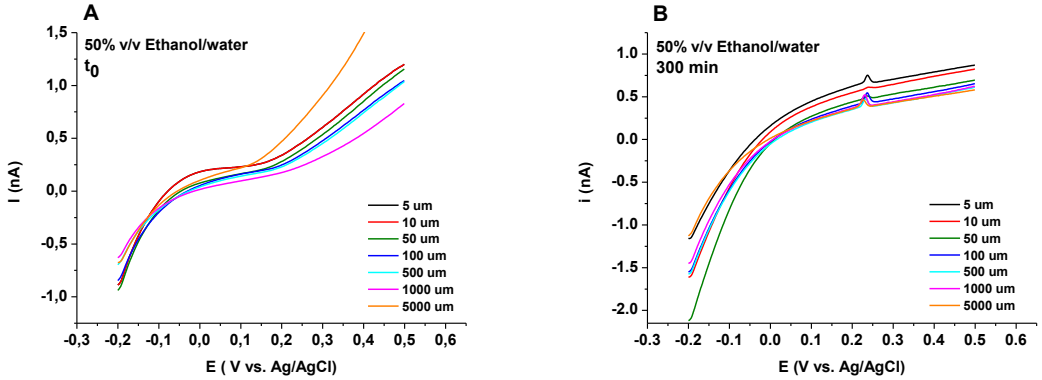

***Fig. 5.38**: ASVs recorded above the AgNPs-EPS sample immersed in 50% v/v ethanol/water hydroalcoholic solution. A) few min after the immersion and B) immersion time 300 min. Tip-substrate distances as indicated. Stripping scan rate 50 mV/s.*

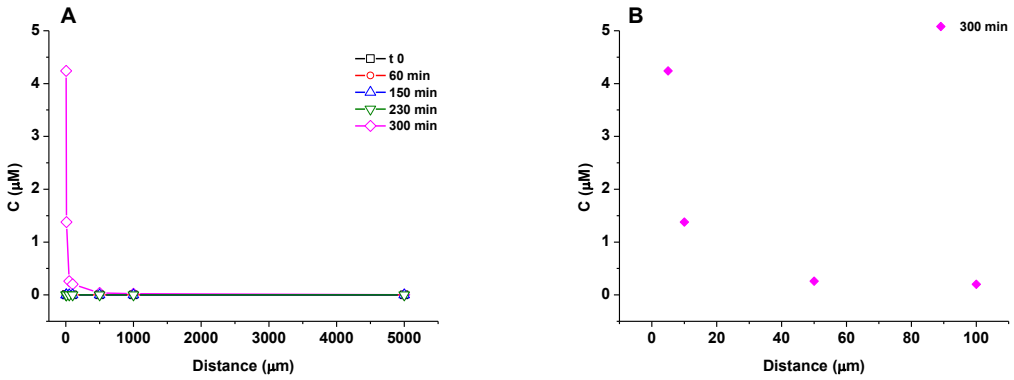

Fig. 5.39: *A) Ag(I) concentration profile relative to the AgNPs-EPS and B) expanded plot.*

Ag(I) concentrations evaluated at 5 μm above the substrate after about five hours of immersion are displayed in Table 5.4.5. These concentration values if compared with those obtained for bulk silver in the same media are significantly larger, in agreement with the effect of particle size on reactivity (see Table 5.4.3). The dissolution rate of AgNPs is in fact strongly linked to the surface area to volume ratio. Thus, the Ag(I) release varies inversely with the size of AgNPs[30,31].

Table 5.4.5: *Concentration of Ag(I) released, evaluated at 5 μm after 300 min of immersion of AgNPs-EPS samples in the indicated media and for an accumulation time of 120s.*

Solvent	*Concentration (μM)*
10% v/v Ethanol/water	34.3
20% v/v Ethanol/water	3.51
50% v/v Ethanol/water	4.24

5.5 Characterization of commercially available goods containing AgNPs

In this section, the strategies, discussed in the previous sections for evaluating either the Ag^0 content in a Ag-loaded sample and the release of Ag(I) forms at the substrate/solution interface, were applied to commercially available goods, in which according to the labels, would contain silver micro- or nano-particles. The products investigated (from local markets) were a microfiber kitchen cloth with antibacterial silver ions and an antimicrobial food container with Microban® 3G Silver™.

[30] W. Zhang, Y. Yao, N. Sullivan, Y. Chen, *Environ. Sci. Technol.* **2011**, 45, 4422-4428.
[31] D. He, M. W. Bligh, T. D. Waite, *Environ. Sci. Technol.* **2013**, 47, 9148-9156.

Microfiber kitchen cloth with silver ions

The microfiber cloth was cut in squares of 1.5 cm × 1.5 cm and both SEM and SECM measurements were performed. Fig. 5.40 shows a SEM micrograph of the cloth and the relative EDS spectrum.

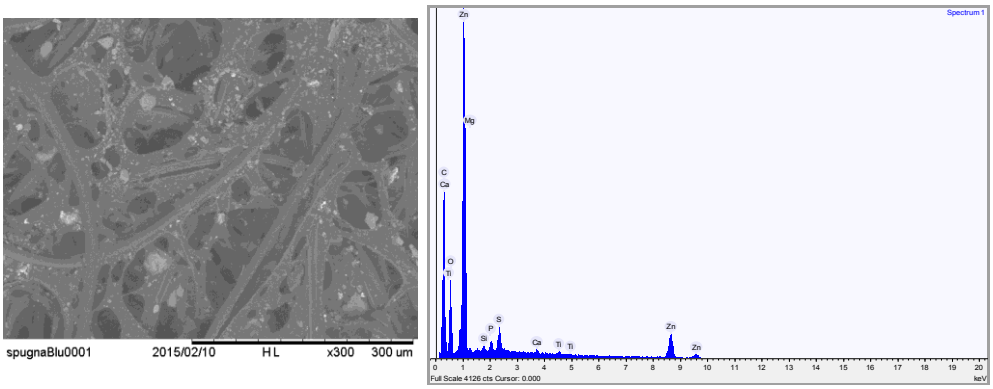

***Fig. 5.40**: SEM micrograph of the microfiber kitchen cloth with antibacterial silver ions and related EDS spectrum.*

The SEM image indicate that the cloth displays a fiber-like structure in which unevenly metal particles of micrometer size are embedded. EDS analysis revealed that they were made mainly of zinc compounds, while no peak due to Ag was evidenced.

To confirm the absence of Ag species in reduced forms, the microfiber cloth was examined by SECM in feedback mode using K_3IrCl_6 as redox mediator. Fig. 5.41 shows typical approach curves recorded above the sample in various zones, and as is evident in all cases only negative feedback profiles were recorded. This indicates the absence of Ag^0 species. The experimental approach curves, obtained at the closest tip-substrate distance, display flat profiles with no negligible currents. These were explained as due to the penetration of the SECM tip within the soft and porous sample, where diffusion of the redox mediator can still occur through solution-filled interstitial channels.

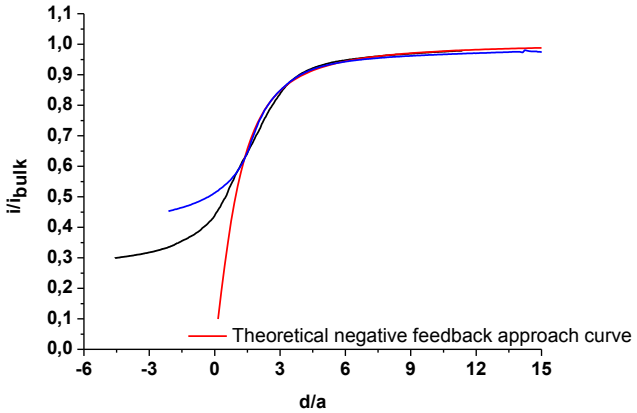

***Fig. 5.41**: Approach curves recorded in different locations of the microfiber kitchen cloth.*

To exclude also the presence of silver particles in the oxidized form in the matrix, SECM-ASV measurements were performed in the various media considered in the previous sections. The parameters employed in the ASVs were those shown in Table 5.4.4.

Fig. 5.42 displays typical responses obtained, from which it is clearly evident that no Ag(I) was detected, whatever was the medium.

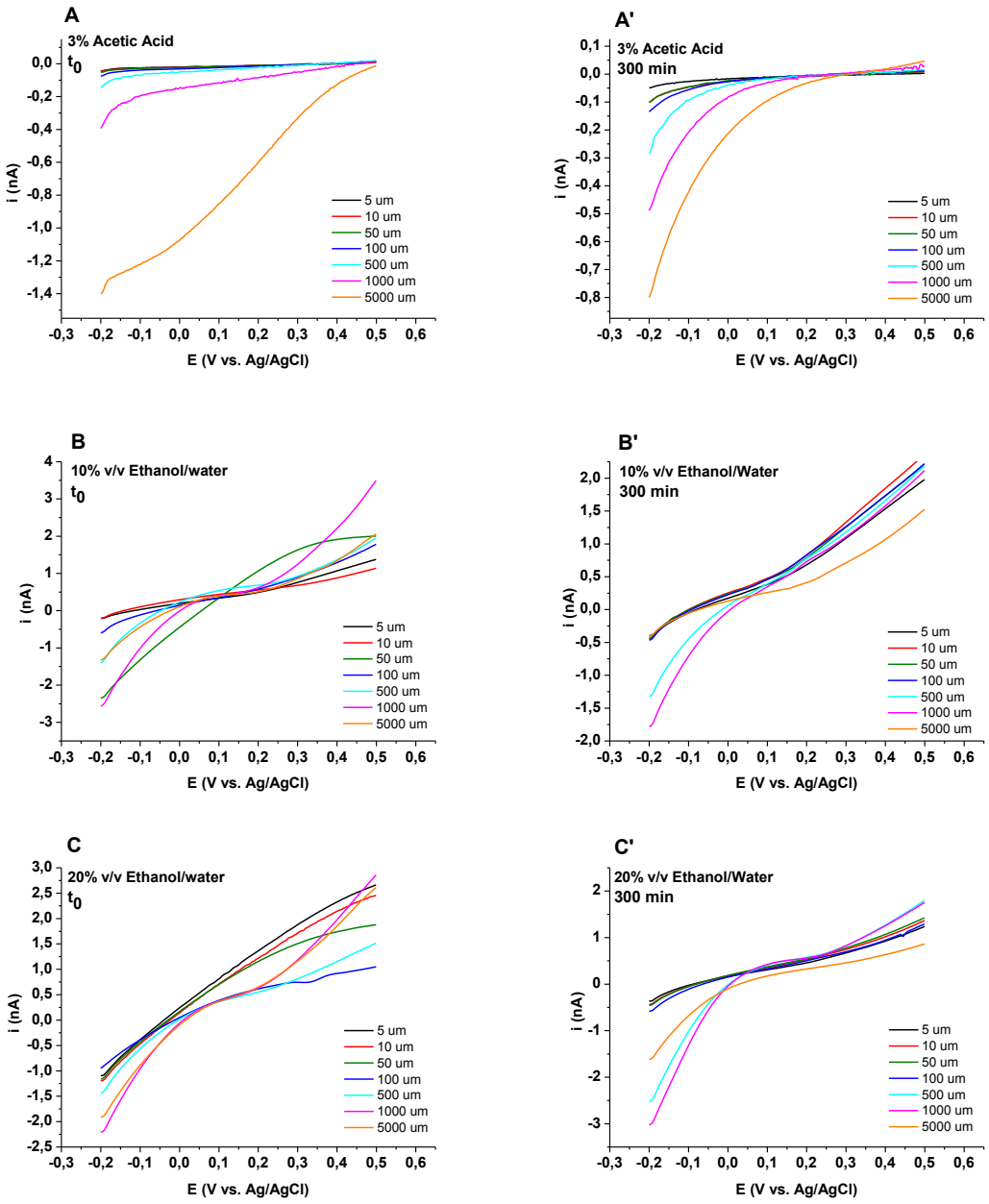

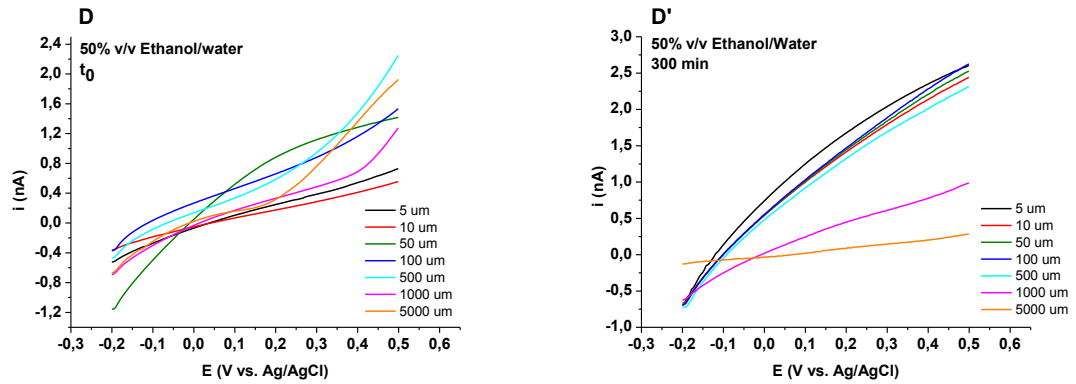

***Fig. 5.42**: ASVs recorded above the microfiber kitchen cloth sample immersed in A) 3% acetic acid aqueous solution, B) 10% v/v ethanol/water, C) 20% v/v ethanol/water and D) 50% v/v ethanol/water hydroalcoholic solutions A-D) few min after the introduction of the solution in the cell and A'-D') after five hours. Tip-substrate distances as indicated; stripping scan rate 50 mV/s.*

In order to further support the absence of any detectable Ag(I) species, a series of SECM-ASV measurements were also performed using an accumulation time, during the preconcentration step, of 300 s (instead of 120 s as for the previous cases). These to exclude any problem with the sensitivity of the measurements. The results obtained were in all cases identical to those reported in Fig. 5.42.

Considering these results, it is possible to conclude that the label of the product was reported a falsehood statement.

Antimicrobial food container

The food container was cut by a circular saw in squares of 2 cm × 2 cm and examined by either SECM and SECM-ASV, similarly as in the previous case.

Fig. 5.43 shows the approach curves obtained in different locations of the food container employing K_3IrCl_6 as redox mediator. Also, for this sample, in all cases negative feedback effects were recorded, apparently indicating that no Ag^0 forms were present in the matrix.

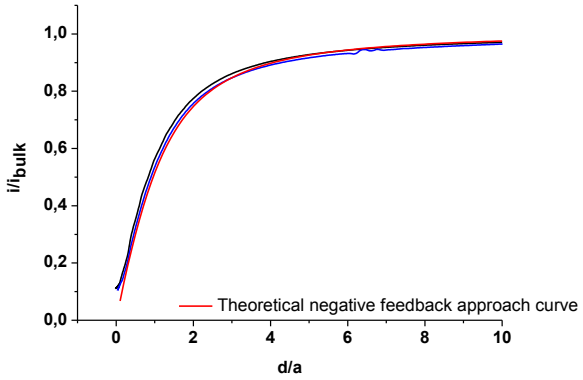

Fig. 5.43*: Approach curves recorded in different locations of the antimicrobial food container.*

However, when the release of eventual Ag(I) from the substrate was investigated by SECM-ASVs in 50 % v/v ethanol/water and in 3% acetic acid, employing the parameters reported in Table 5.4.4, measurable ASV peaks, due to silver, could be recorded in the latter medium. The different effect of the two media is shown in Figs. 5.44 and 5.45.

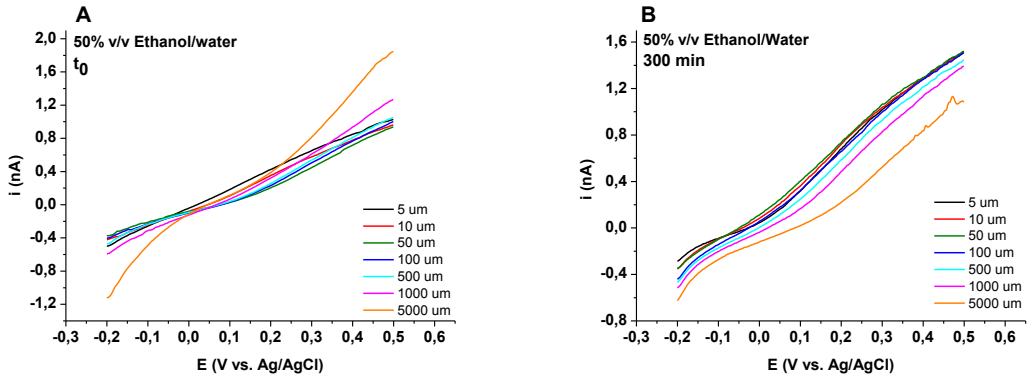

Fig. 5.44: *ASVs recorded in above the antimicrobial food container immersed in 50% v/v ethanol/water hydroalcoholic solutions. A) few min after the immersion and B) immersion time 300 min. Tip-substrate distances as indicated; stripping scan rate 50 mV/s.*

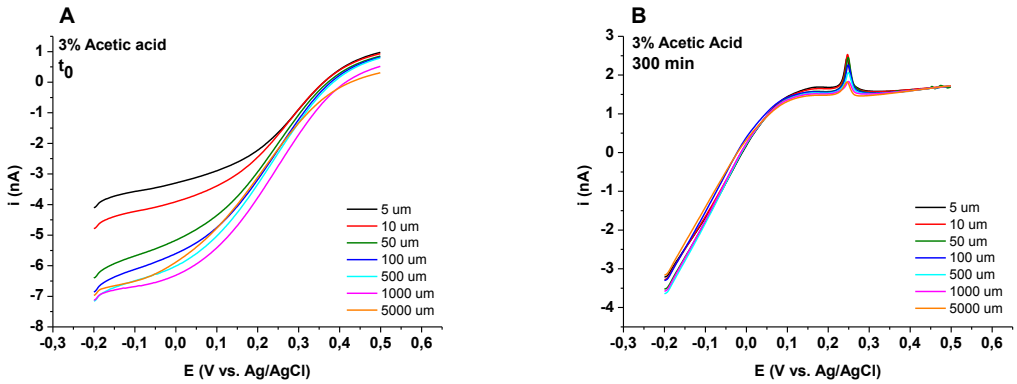

Fig. 5.45: *ASVs recorded above the antimicrobial food container immersed in 3% acetic acid aqueous solution. A) few min after the immersion and B) immersion time 300 min. Tip-substrate distances as indicated; stripping scan rate 50 mV/s.*

In the 3% acetic acid medium the concentration profile above the food container could also be evaluated, and data are summarized in Fig. 5.46.

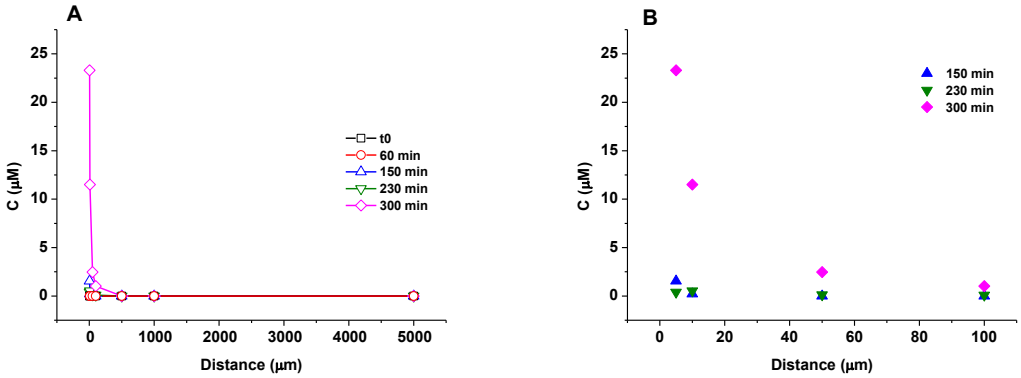

Fig. 5.46*: A) Ag(I) concentration profile relative to the antimicrobial food container and B) expanded plot.*

The silver concentration at 5 µm above the substrate was found to be 2.33×10^{-5} mol/L.

Finally, we can conclude that in the food container some silver particles are actually embedded within its matrix. From our data, apparently, they are formed by oxidized forms of silver. However, we cannot exclude the presence of Ag^0 particles, which could be buried within the plastic material, and consequently, not readily available to provide the regeneration of the Ir(III) redox mediator, as the substrate is scarcely wettable by simple water or water/ethanol media.

Chapter 6: SECM investigation of surface conductivity of graphene thin layers deposited on insulating and conducting substrates

Graphene is defined by IUPAC as "a *single carbon layer of graphite structure, describing its nature by analogy to a polycyclic aromatic hydrocarbon of quasi-infinite size"*[1].

Graphene is one of the thinnest materials with one-atom-thick planar sheet of sp^2-bonded carbon atoms densely packed in a honeycomb crystal lattice[2,3,4]. It is the basic structure of a variety of materials like graphite, carbon nanotubes and fullerenes (see Fig. 6.1)[2]. Due to the sp^2-bonds and its electronic configuration ($1s^2\ 2s^2\ 2p^2$), graphene possesses extraordinary properties, such as large surface area, theoretically 2630 m^2/g for a single layer, and doubles that of single-walled carbon nanotubes (SWCNTs)[5]. It shows exceptional thermal ($k = 5\times10^3$ W/m×K) and electrical conductivity (σ = 64 mS/cm). It can be considered a zero-gap semiconductor, because it presents no gap between conduction and valence bands, so it might be considered a semiconductor or a metal[5]. In physical properties, graphene possesses optical transparence, high mechanical strength (Young's modulus, ~1100 GPa) and elasticity[2,5].

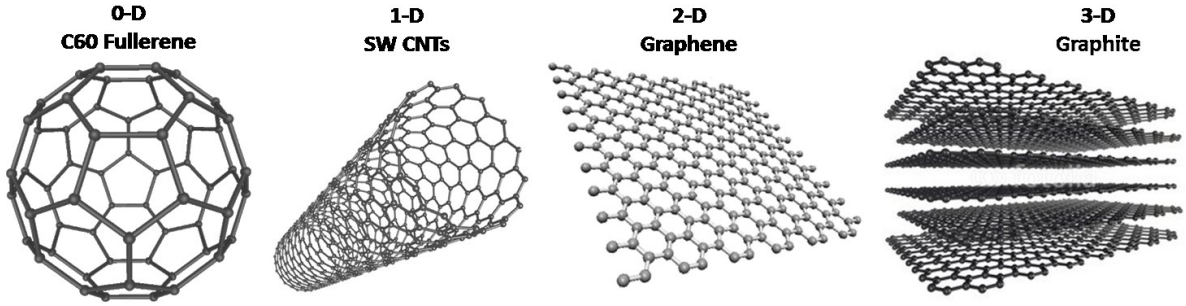

Fig.6.1*: Carbon nanostructures.*

The terminology used to define graphene materials is important, as many difference exist in the literature[5] . In particular, according to the number of layers, three groups are established: (i) single layer graphene, (ii) few layers graphene (typically between 2 and 9) and (iii) multi-layers graphene (more than 10). Another terminology adopted is established considering the chemical synthesis of graphene; this also includes the carbon source used for the preparation. Thus, if the

[1] A.Ambrosi, C. K. Chua, A. Bonanni, M. Pumera, *Chem. Rev.* **2014**, 114, 7150-7188.
[2] W. W. Liu, S. P. Chai, A. R. Mohamed, U. Hashim, *J. Ind. Eng. Chem.* **2014**, 20, 1171-1185.
[3] C. Reiner-Rozman, J. Schodl, C. Nowak, C. Kleber, *e-J. Surf. Sci. Nanotech.* **2015**, 13, 366-372.
[4] K. Torbensen, M. Kongsfelt, K. Shimizu, E. B. Pedersen, T. Skrydstrup, S. U. Pedersen, K. Daasbjerg, *Langmuir* **2015**, 31, 4443-4452.
[5] A. Martin, A. Escarpa, *Trends in Analytical Chemistry* **2014**, 56, 13-26.

carbon source is graphite, it is possible to obtain chemically modified graphene (which includes graphene oxide and reduced graphene oxide); (ii) when the carbon source is CNTs the resulting materials are graphene nanoribbons (prepared by unzipping of CNTs)[5]. Graphene oxide (GO) and reduced graphene oxide (rGO) are of interest in this work; considerations are, therefore, limited to these materials.

GO is a heavily oxidized graphene form[6] with C/O atomic ratio of ≈2, which is typically prepared from graphite oxide by liquid phase exfoliation via ultrasonication; it is hydrophilic and shows insulating behavior[7]. rGO is prepared from the reduction of graphene oxide by thermal, chemical[8] or electrochemical treatments[6]. It displays hydrophobic and conductive behavior; the use of different reducing agents will lead to various C/O ratios and chemical compositions[6]. These variable properties have a significant impact on the output characteristics of sensing devices based on rGO materials. Therefore, any method able to characterize the degree of the reduction success of the GO sheets over a specific area and the surface coverage of the substrate is ideal to make statements about the statistical quality of fabricated sensing devices.

A wide range of techniques have been used to characterize morphology, physical and chemical properties of graphene materials[1]. They include: (i) microscopic techniques such as optical microscopy, SEM, TEM, STM and AFM; (ii) spectroscopic techniques like Raman, IR, UV-Vis, NMR and XPS; (iii) X-Ray diffraction and (iv) electrochemical techniques. Microscopic techniques allow the evaluation of morphological aspects; spectroscopic techniques permit the estimation of the inner structure of the graphene materials; XRD lets the assessment of structural properties; electrochemical techniques allow the study of inherent electrical properties, such as conductivity. The latter property is of paramount importance when thin graphene films, deposited on an insulating substrate, have to be employed as electrode materials. Electrical properties have often been investigated with various methods which provided area-average characteristics. For instance, the conductivity of thin films is generally evaluated using a four-point probe technique[9]. This method requires putting metallic tips in contact with the substrate which unavoidably damages the film, especially when it is only few nanometers thick. In addition, this procedure provides a conductivity evaluation that is averaged over large areas, typically over millimeters ranges. This approach is useful for highly homogeneous films but it is not suitable for very thin films from which it cannot reveal the local variability of conductivity at micrometric scale.

Surface defects also play an important role in the electrochemical activity of finished graphene materials. These defects are usually composed of various types of organic oxygenated moieties such as carbonyl, carboxylic acid, lactone and quinone functional groups[1]. The reactivity of these groups can somewhat be predicted by computational methods[10]. Also, examples of electrochemical studies exist in the literature in which the area averaged-characteristics of thin layer grafene containing oxygenated species have been evaluated[1].

---

[6] M. Pumera, *Electrochem. Commun.* **2013**, 36, 14-18.
[7] L. B. Pires, B. Perez Lopez, C. C. Mayorga Martinez, E. Morales-Narvaez, N. Domingo, M. J. Esplandiu, F. Alzina, C.M. Sotomayor Torres, A. Merkoçi, *Biosens. Bioelectron.* **2014**, 61, 655-662.
[8] H. A. Becerril, J. Mao, Z. Liu, R. M. Stoltenberg, Z. Bao, Y. Chen, *ACS Nano* **2008**, 2(3), 463-470.
[9] Q. Zheng, W. H. Ip, X. Lin, N. Yousefi, K. K. Yeung, Z. Li, J. K. Kim, *ACS Nano* **2011**, 5, 6039-6051.
[10] N. Ghaderi, M. Paressi, *J. Phys. Chem. C* **2010**, 114, 21625-21630.

Spatially resolved measurements (at micrometric scale) to elucidate some properties of graphene materials are also of interest; these can be performed by the use of scanning electrochemical microscopy.

Recently, SECM has been used to locally investigate the heterogeneous electron transfer rate constant of the materials[11,12], to patterning graphene films on conductive surfaces[13] or local carboxylate graphene layer[4], to measure the local surface conductivity of GO thin films[11] and evaluate their electrochemical activity[3]. In the present study, SECM is employed for quantitative mapping of the electronic conductivity and redox activity of rGO produced with an innovative approach as described below. The final goal of the study is to ascertain the suitability of the graphene, deposited with the new approach on insulating and conducting substrates, to be utilized as electrodes for the production of electrochemical sensing devices.

6.1 Reduced graphene oxide fabrication and optical characterization

The graphene substrates were prepared in the Laboratory of Prof. A. Merkoçi at the Catalan Institut of Nanoscience and Nanotechnology (Universitat Autonoma de Barcelona, Spain) using a patented procedure based on a pressure/wax-based transferring technique (patent requested: P3046PC00 (02/04/2015)) employing chemical exfoliated graphene materials.

Firstly, GO was patterned onto PET or ITO substrates in bands of 75 or 500 µm width and 2 mm long, and in disk shaped geometries of 4-5 mm diameter. GO was then reduced by hydrazine vapor for 24 h at 60°C to obtain rGO, following a procedure available in the literature[8,14]. For these samples, the thickness of the deposit, evaluated by AFM measurements, resulted to be over in the range of 4-5 nm. An electrochemical approach was instead employed to reduce GO deposited onto ITO conducting substrates.

Fig. 6.2 shows optical images of two GO bands 500 µm width, deposited on a PET substrate, before (6.2 A) and after reduction with hydrazine (6.2 B).

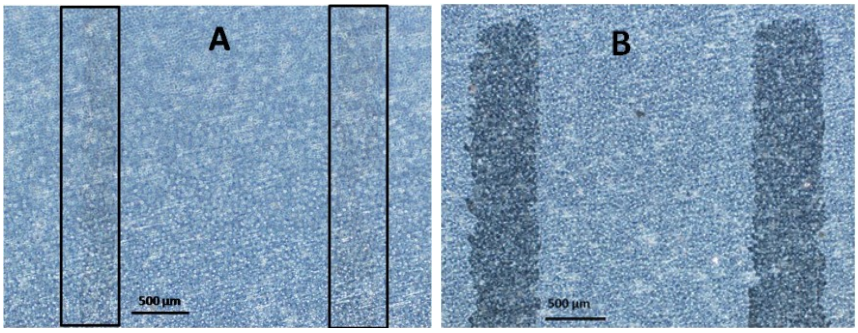

Fig. 6.2*: Optical images of two GO bands deposited on a PET substrate A) before and B) after chemical reduction with hydrazine.*

[11] J. Azevedo, C. Bourdillon, V. Derycke, S. Campidelli, C. Lefrou, R. Cornut, *Anal. Chem.* **2013**, 85, 1812-1818.
[12] C. Tan, J. Rodriguez-Lopez, J. J. Parks, N. L. Ritzert, D. C. Ralph, H. C. Abruna, *ACS Nano* **2012**, 6(4), 3070-3079.
[13] L. Liu, C. Tan, J. Chai, S. Wu, A. Radko, H. Zhang, D. Mandler, *Small* **2014**, 10(17), 3555-3559.
[14] D. C. Marcano, D.V. Kosynkin, J. M. Berlin, A. Sinitskii, Z. Sun, A. Slesarev, L. A. Alemany, W. Lu, J. M. Tour, *ACS Nano* **2010**, 4(8), 4806-4814.

As is evident, before the reduction process, the material is transparent, in agreement with literature reports[1,7] and it is not easy to individuate on the PET substrate (in the image of Fig. 6.2 A, the GO bands are highlighted with the black rectangles); after the reduction treatment, dark grey of rGO traces are clearly evident (image in Fig. 6.2 B). Under the optical microscope, the rGO bands appear not uniform, especially at their edges. Similar images (not shown) were also observed by optical examination of the GO and rGO bands 75 µm with. Since, these circumstances could affect the local electronic conductivity inside the films, the various graphene samples were investigated in detail by SECM.

6.2 SECM investigation on GO and rGO deposited on the PET substrate

The GO thin films, after their deposition on PET, were investigated by SECM in feedback mode, using either $K_3Fe(CN)_6$ or FcMeOH as redox mediators. Fig. 6.3 shows typical steady state voltammograms obtained with a Pt SECM tip 12.5 µm radius, using the two redox mediators in aqueous solutions containing 0.2 M KCl or 0.2 M KNO_3 as supporting electrolyte. From the voltammograms, half-wave potentials ($E_{1/2}$) of -0.177 V and 0.207 V for the $Fe(CN)_6^{3-/4-}$ and $FcMeOH/FcMeOH^+$ redox couples, respectively, were evaluated. For all SECM measurements, including approach curves, line and two-dimensional scans, were performed by biasing the Pt microdisk at -0.2 V and 0.4 V for $K_3Fe(CN)_6$ and FcMeOH, respectively.

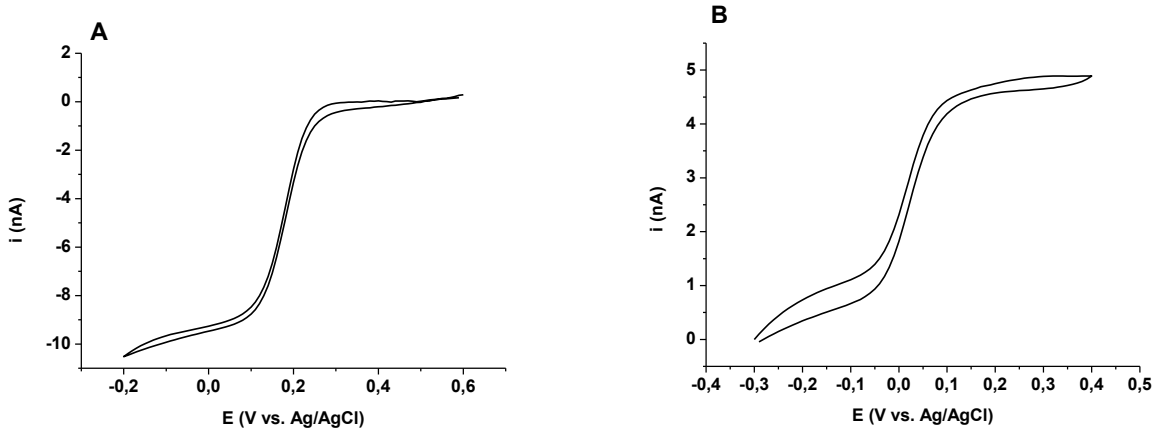

***Fig. 6.3**: Cyclic voltammetry recorded in A) 2 mM $K_3Fe(CN)_6$ + 0.2 M KCl and B) 2 mM FcMeOH + 0.2 M KNO_3 at 10 mV/s for a 12.5 µm radius Pt microdisk electrode.*

6.2.1 SECM of GO samples

Fig. 6.4 shows a typical approach curve (red line) recorded above a GO band 500 µm width, and, as is evident, it displays the negative feedback response expected for an insulating material[15]. This was confirmed by the fact that approach curves recorded above GO-uncoated regions of PET (blue line) and the theoretical diffusion controlled negative feedback approach curve (black line), fully overlapped (Fig. 6.4). The observed behavior agrees with those obtained for GO samples prepared with various methods[3,16,17].

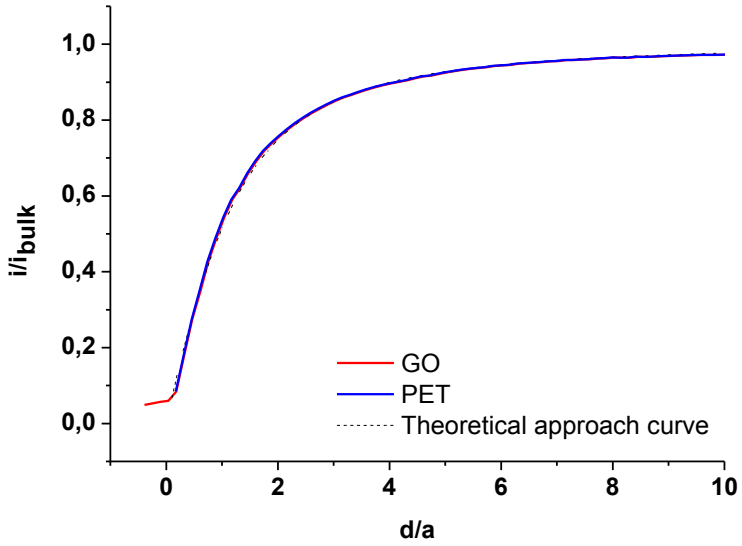

***Fig. 6.4**: Approach curve recorded above GO films (red line) and GO-uncoated PET (blue line) by using a Pt microdisk of 12.5 µm in radius in 2 mM $K_3Fe(CN)_6$ + 0.2 M KCl. For comparison, theoretical approach curve for negative feedback (black line).*

The GO samples were also investigated by using SECM in scanning mode, after positioning, firstly, the SECM tip few µm (5 -10 µm) above the samples; afterwards it was scanned across a line or the plane parallel to the substrate. Figs. 6.5 show a typical line scan (Fig. 6.5 A) and a two-dimensional scan (Fig. 6.5 B) above a GO band of 500 µm width. As is evident, both types of scans are featureless and the change of current along the axes can be attributed to the lack of perpendicular alignment, across the entire surface investigated, of the tip above the substrate (*i.e.*, so called tilting). This was ascertained by performing measurements, under the same conditions, above an GO-uncoated PET region, which provided similar responses (not shown).

[15] A. J. Bard, M. V. Mirkin, *Scanning Electrochemical Microscopy*, Marcel Dekker, Inc, New York **2001**.
[16] J. Molina, J. Fernandez, A. I. del Rio, B. F. Cases, *Appl. Surf. Sci.* **2013**, 279, 46-54.
[17] S. Rapino, E. Treossi, V. Palermo, M. Marcaccio, F. Paolucci, . Zerbetto, *Chem. Commun.* **2014**, 50, 13117-13120.

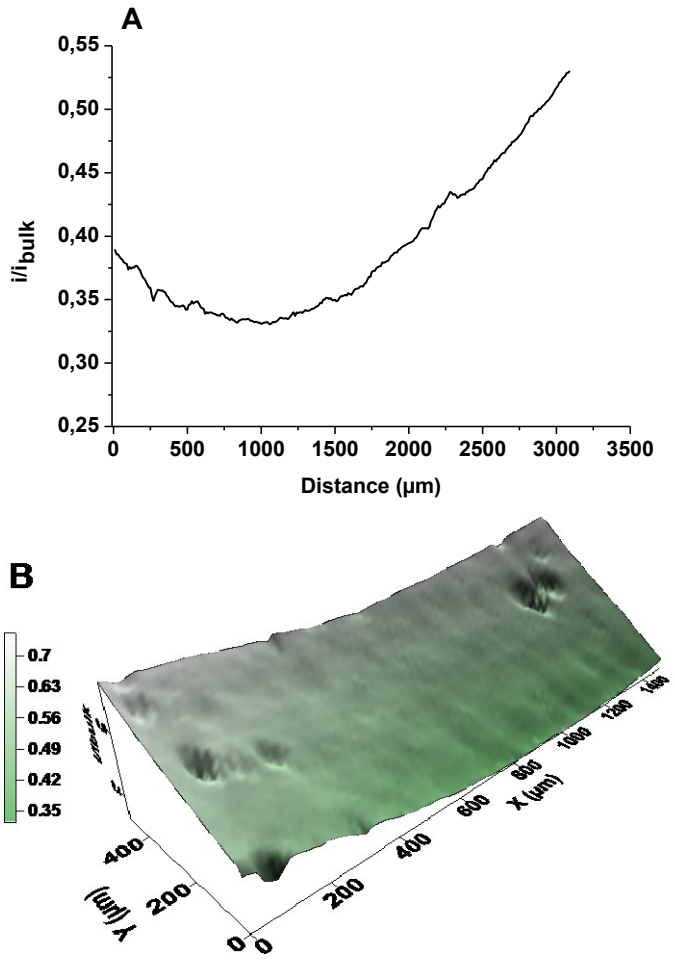

***Fig. 6.5**: A) Linear and B) 2D scans recorded above GO bands by using a Pt microdisk of 12.5 µm in radius and 2 mM $K_3Fe(CN)_6$ as redox mediator; E_{tip} = -0.2 V vs. Ag/AgCl.*

6.2.2 SECM of rGO samples prepared by chemical reduction

Fig. 6.6 shows typical approach curves recorded above a rGO band 500 µm width, using $K_3Fe(CN)_6$ as redox mediator. As is evident, in this case, depending on specific locations, responses ranging from attenuated negative feedback (Fig. 6.6 blue, cyan and magenta curves) to positive feedback (Fig. 6.6 green curve) were recorded.

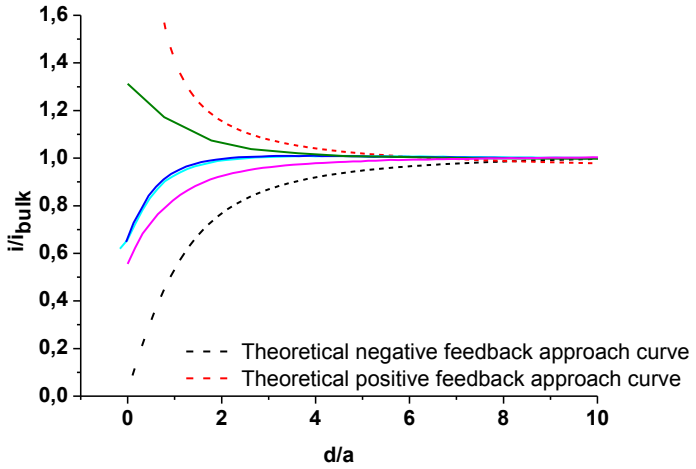

***Figure 6.6**: Approach curves recorded above rGO band of 500 µm width in different locations (E_{tip} = -0.2 V vs. Ag/AgCl). Approach curve for processes diffusion controlled are included.*

Since in all measurements, the substrate was unbiased, the different behavior observed can be explained by taking into consideration the following circumstances. As for the attenuated negative feedback responses, they can be due to: a limited size of the conducting substrate below the SECM tip (see later)[15,18]; a poor conductivity due to either the rather thin film of the rGO or to the local non-homogeneity of the film (conducting particles percolation[11]); a limited values of the heterogeneous electron transfer rate constant[1,15]. All these limitations are strongly affected by the oxidation degree of the rGO layers and, consequently, on the content of oxygenated species[1].

Since $K_3Fe(CN)_6$ has been reported to be highly sensitive to defects of carbon materials, including graphene[1,12], a series of approach curves were also performed using FcMeOH as redox mediators, which is known to be rather insensitive to the specific structure of the materials[1,12]. Also with FcMeOH, results similar (not shown) to those recorded with $K_3Fe(CN)_6$ were obtained, indicating that the SECM behavior of the rGO did not depend on the specific redox mediator employed or on their redox potential.

As for the positive feedback response, it arises for the bipolar nature of the system[18], since a significant area of the substrate away from the tip is bathed in a solution whose concentration has not been perturbed by the tip-reaction (scheme in Fig. 6.7, for a generic O/R redox mediator)[15,18]. Thus, in the latter zone, the substrate is poised at potentials established by the species in the bulk solution (*i.e.*, $K_3Fe(CN)_6$ or FcMeOH), and at open circuit, its potential is positive or negative with respect to $E_{1/2}$ of the corresponding redox couple. When the tip approaches the substrate, a portion of the substrate directly under the tip is exposed to the electrode reaction product, which instantaneously undergoes the inverse redox reaction. It must be noted that the potential of an unbiased substrate is also perturbed by the current flow, which is required for recycling the mediator. Thus, the feedback response can also be perturbed by finite heterogeneous electron-transfer kinetics[15]. The lateral electron transport scheme displayed in Fig. 6.7 is operative in

[18] A. I. Oleinik, D. Battistel, S. Daniele, I. Svir, C. Amatore, *Anal. Chem.* **2011**, 83, 4887-4893.

conductive substrate whose surface area is sufficiently larger than that of the micro-tip counterpart.

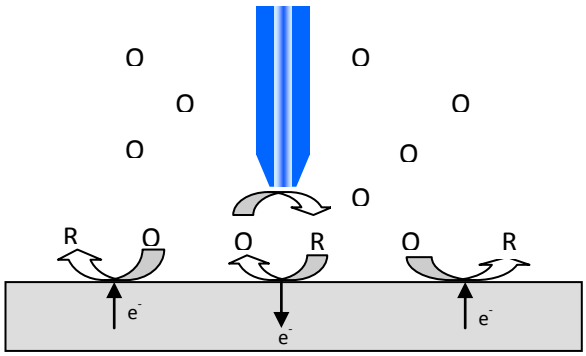

***Fig. 6.7**: Scheme of the lateral electron transfer and positive feedback at an unbiased substrate for a generic O/R redox mediator.*

More insights on the homogeneity of the rGO bands were obtained by performing line and two-dimensional scans over either a single or a couple of rGO bands both of 500 µm width. Typical scans obtained by using $K_3Fe(CN)_6$ and FcMeOH are shown in Figs. 6.8 and 6.9. As is evident, in both situations the rGO material deposited onto the PET surface could be individuated by the sudden current increase as soon as the SECM tip travelled above the conducting or active materials. However, high current fluctuations within the bands were also observed, indicating local non-homogeneity. Moreover, using the same redox mediator, maxima of feedback currents varied from zone to zone (Fig. 6.8 B and Fig. 6.9).

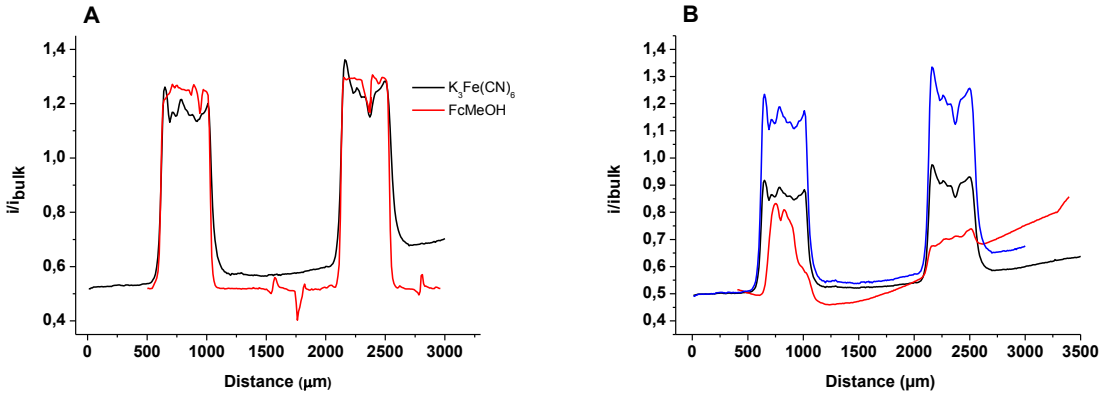

***Figure 6.8**: A) Linear scans recorded above rGO bands of 500 µm width by using a Pt microdisk of 12.5 µm in radius in (--) 2 mM $K_3Fe(CN)_6$ + 0.2 M KCl (E_{tip} = -0.2 V vs. Ag/AgCl) and (--) 2 mM FcMeOH + 0.2 M KNO_3 (E_{tip} = 0.4 V vs. Ag/AgCl). B) Linear scans recorded above rGO bands of 500 µm width in different locations by using 2 mM $K_3Fe(CN)_6$ + 0.2 M KCl; E_{tip} = -0.2 V vs. Ag/AgCl.*

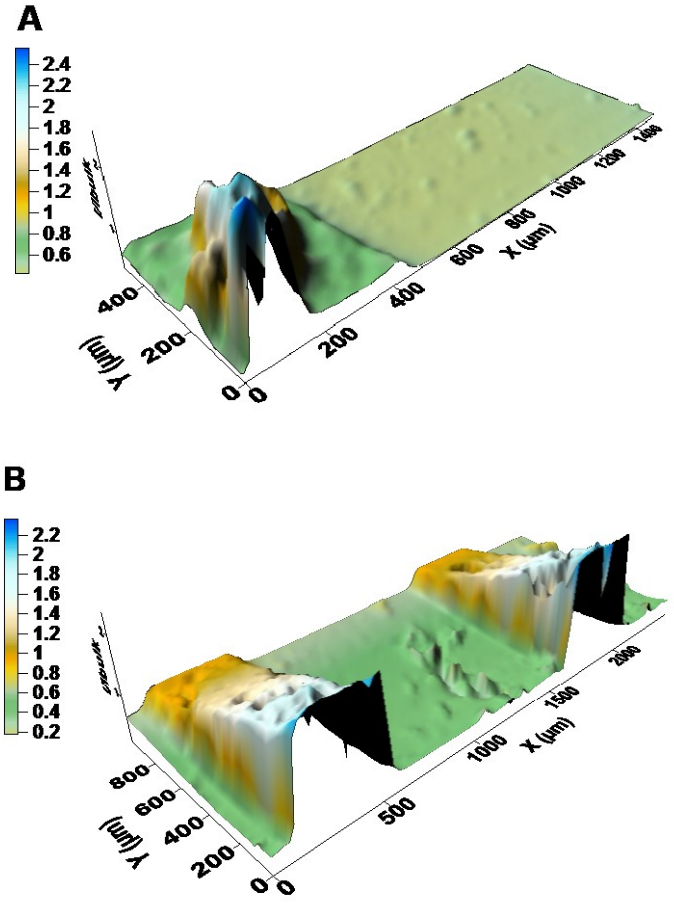

***Figure 6.9**: 2D scans recorded above rGO bands of 500 µm width by using a Pt microdisk of 12.5 µm in radius in A) 2 mM $K_3Fe(CN)_6$ + 0.2 M KCl (E_{tip} = -0.2 V vs. Ag/AgCl) and B) 2 mM FcMeOH + 0.2 M KNO_3 (E_{tip} = 0.4 V vs. Ag/AgCl).*

From the above results, the limitation due to the size of the substrates can be excluded. In fact, considering the length along where the current rises, a width of about 500 µm could be evaluated, *i.e.*, the expected size of the fabricated bands. At unbiased substrates, size effects manifest when the substrate is smaller than about 5 times the radius of the SECM tip[11,15]. This is not the case for the samples investigated. Also, because of the similar shape of the scan lines or the two-dimensional profiles recorded with both the redox mediators, no limitation due to the heterogeneous electron transfer rate could be invoked. Mechanical defects, due to damaging of the graphene surface or non-homogeneous coatings cannot be excluded. Thus, it is likely that problems related to low conductivity or defects, due to presence of chemical species at the surface of the material, are responsible of the variable feedback currents recorded. However, at this stage we are unable to distinguish which one of the two properties has major effects in the current inhibition. As a matter of fact, both the latter phenomena reflect on an apparent conductivity of the material. This property can be estimated by using a procedure, reported recently in the literature, based on the approach curves recorded by SECM[11] (Fig. 6.10).

In this approach, the electron transport inside the film is assumed to occur according to a local Ohms's Law. The surface conductivity, σ, is related to a dimensionless conductivity, σ^*, parameter by the following equation:

$$\sigma^* = \sigma e \frac{RT}{nF} \frac{1}{nFD\, C_b a} \tag{6.1}$$

where, *e* is the thickness of the conducting film, *R* is gas constant and the other symbols have their usual meanings.

An apparent conductivity, σ^*, can be evaluated by using the normalized current Ni_T (*i.e.*, i/i_{bulk}) (Fig. 6.10 b), which in turn depends on $L = d/a$, *RG* and on the ratio between the concentration of the two forms of the redox couple (*N*) present in the bulk solution. For instance, for FcMeOH *N* is given by the following expression[11]:

$$N = C_{bFcMeOH} / (C_{bFcMeOH} + C_{bFcMOH^+}) \tag{6.2}$$

For *N* = 1, a working curve, as that displayed in Fig. 6.10 b (taken from Ref. 11), can be used for evaluating σ^* from experimental Ni_T values. The family of plots of Fig. 6.10 b were obtained by a simulation procedure and depends on the dimensionless charge transfer kinetic constant, *k*. For a reversible process, the curve with black symbols holds. This working curve was employed here to obtain σ^* values, which, for *L* = 0.5 ranged between 0.20 and 0.55.

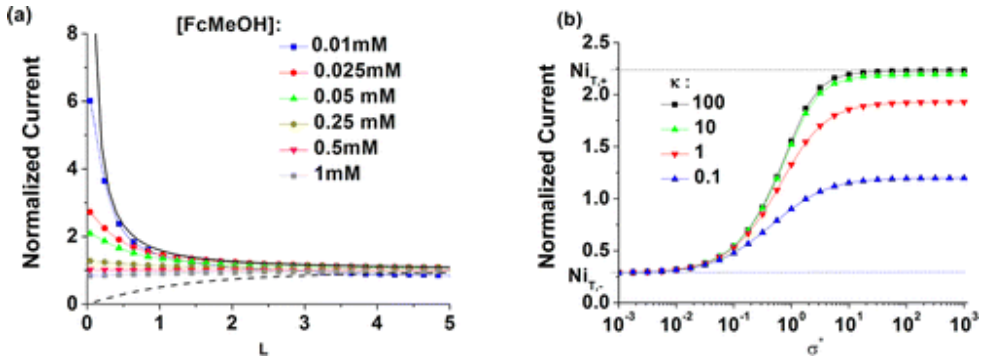

Fig. 6.10*: a) Experimental approach curves above a reduced GO layer with FcMeOH at different concentrations (see figure), for a probe polarized at 0.4 V vs. Ag/AgCl, RG = 10, a = 12 µm, N = 1. Black continuous line and black dotted line: theoretical pure positive and negative feedback approach curves, respectively (RG = 10). b) Normalized current as a function of the substrate conductivity for different charge transfer kinetic constants (see figure), for L = 0.5, RG = 10, Rs (is the normalized substrate size) = 100 and N = 1. All data were taken from Reference 11.*

For the special case of *N* = 0.5 the analytical expression (6.2) was also derived:

$$\sigma^* = (0.138L + 0.0858)(Ni_T^{0.6+2.27L/RG^{0.146}} + 0.22\ln(RG) + 0.4)^{3.28+2.3L/RG^{1.54}} - 0.1152RG^{0.2}L^{2-0.165\ln(RG)} - 0.0087RG - 0.03 \tag{6.3}$$

This equation is valid with 7% accuracy for: i) $0.3 < L < 1.5$; ii) $2 < RG < 20$ and iii) $0.1 < \sigma^* < 5$. Using both methods based on the working curve of Fig. 6.10 b and Equation 6.2, along with experimental Ni_T values, electrical conductivity over the range 37 (± 5) mS/cm – 102 (± 5) mS/cm and 30 (± 5) mS/cm – 82 (± 5) mS/cm were obtained, assuming for the graphene film a thickness of 4 nm and 5 nm, respectively. These values are comparable with those reported in the literature for graphene layers[5,19].

A series of SECM measurements, as those reported above for the rGO bands 500 µm width, was also performed for an array of rGO bands of 75 µm width, deposited on a PET substrate. Fig. 6.11 shows typical line and two-dimensional scans obtained on these systems. As is evident, also in this case, both types of scans allow revealing the active rGO surface, as indicated by the current increase, as the SECM tip travelled above the active zones of graphene. Moreover, current changes are smoother, suggesting that the rGO layers are more homogeneous than those of bigger width, and probably with little defects. The peak shaped responses observed in the line scans, and consequently also in the two-dimensional scans, are related to substrate size limitations, phenomenon already observed in the literature and proven by simulation in previous investigations[20].

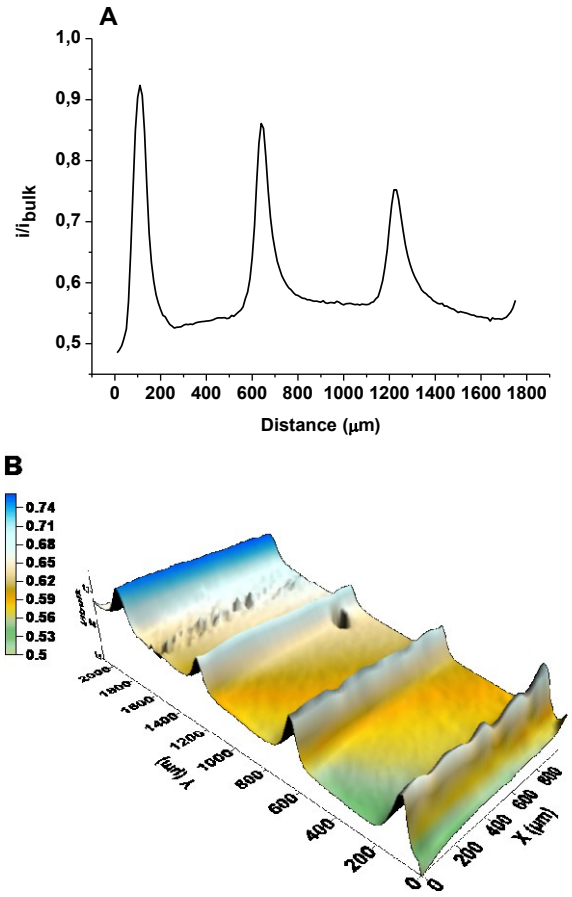

***Fig. 6.11**: A) Linear and B) 2D scans recorded above rGO bands of 75 µm width by using a Pt microdisk of 12.5 µm in radius and 2 mM $K_3Fe(CN)_6$ as redox mediator; E_{tip} = -0.2 V vs. Ag/AgCl*

[19] S. Park, R. S. Ruoff, *Nat. Nanotechnol.* **2009**, 4, 217-224.
[20] D. Battistel, *PhD Thesis*, University Ca' Foscari of Venice, **2009/2010**.

These results, therefore, indicate that the new procedure adopted for the preparation of graphene layers onto a PET substrate is more effective for small rather than for big rGO bands.

Finally, in order to ascertain whether eventually unreduced oxygen functional groups could contribute to the regeneration of the redox mediator, due to an inherent redox activity of the rGO samples produced by chemical reduction, a series of repetitive scans was performed on the same line. In fact, the increment of the current at the SECM tip, when it approaches the substrate, could occur through a simple effect of lateral electron transfer within the graphene films (*i.e.*, through scheme in Fig. 6.7), or by a chemical reaction involving the species of the redox mediator generated underneath the SECM tip and chemical functional groups on the graphene surface. In the first case repetitive scans should provide same responses; in the second case, changes on the chemical nature of surface could occur and this in turn could lead to different current responses depending on the scan repetition.

Figs. 6.12 and 6.13 show two typical consecutive line scans recorded with FcMeOH and $K_3Fe(CN)_6$, respectively, above a rGO sample. The line scans were performed, firstly in one direction; then, after returning to the initial position, above the same line.

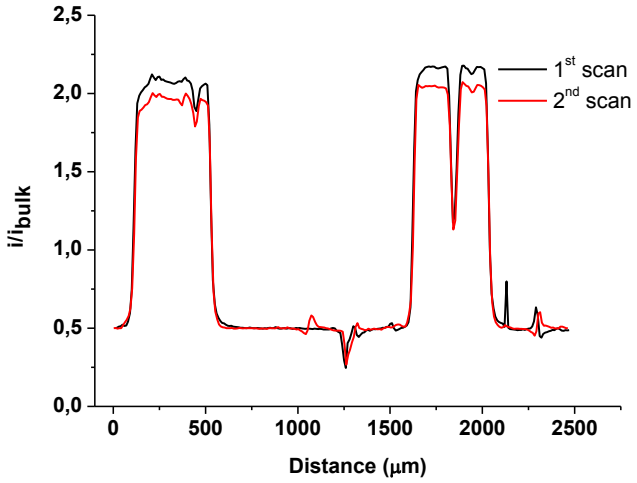

***Fig. 6.12**: Two consecutive line scans recorded above rGO bands of 500 µm width by using a Pt microdisk of 12.5 µm in radius in 2 mM FcMeOH + 0.2 M KNO_3 (E_{tip} = 0.4 V vs. Ag/AgCl).*

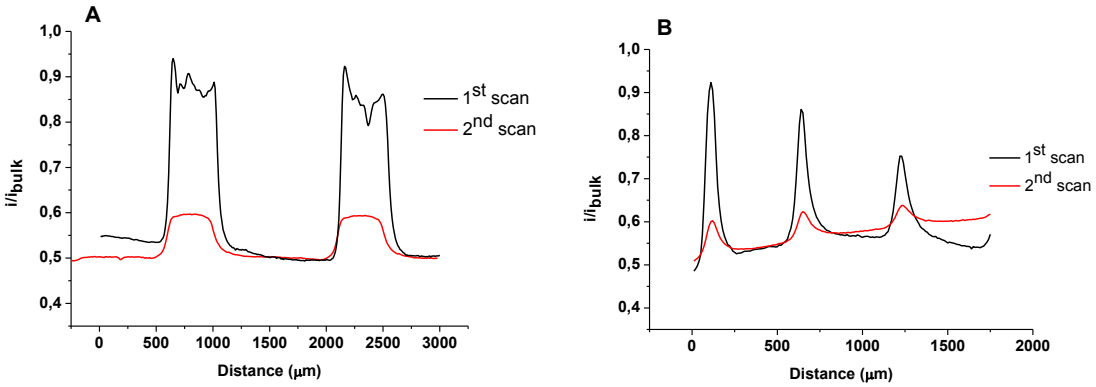

***Fig. 6.13**: Two consecutive line scans recorded above rGO bands of A) 500 μm and B) 75 μm width by using a Pt microdisk of 12.5 μm in radius in 2 mM $K_3Fe(CN)_6$ + 0.2 M KCl (E_{tip} = -0.2 V vs. Ag/AgCl).*

As is evident from Fig. 6.12, the current responses, in repetitive scans, varied to a relatively small extent (within 6%) when FcMeOH was used as redox mediator (the reaction product would act as an oxidant). Instead, a strong current decrease was recorded in the second scan when $K_3Fe(CN)_6$ was used as redox mediator (the reduction product acts as a reductant). These results, therefore, suggest that during the first scan, $Fe(CN)_6^{4-}$, formed at the SECM tip, can locally modify the graphene surface, ultimately leading to a partial passivation of the material. This phenomenon provided a current decrease of about 70% at both the 500 μm width and the 75 μm width rGO bands. At this stage, we have no clear idea on the type of surface modification which might occur. However, it can be hypothesized that $Fe(CN)_6^{4-}$, while is able to eliminate some residual reducible oxygen functionalities, at the same time, it partially destroys the graphene-like properties of rGO or edge-like planes present in the surface, which are known facilitating fast electron transfer[1].

6.3 SECM of rGO samples prepared by electrochemical reduction

Reduced graphene oxide thin films can also be produced through the electrochemical reduction of GO deposited on a conducting substrate[4,13,21,22]. The electrochemical reduction method is an interesting approach, as it can be performed under ambient conditions, does not require toxic or dangerous chemical agents, and requires only simple instrumentations. Thus, in order to ascertain the effectiveness of this reducing strategy for the preparation of rGO coupled to the pressure/wax-based transferring technique, circular GO layers (4-5 mm diameter) were patterned on the surface of a commercially available ITO/PET substrate (Fig. 6.14 A). The ITO/PET substrate was connected to the external circuit by a copper wire fixed at one edge of the ITO surface with a silver conducting resin.

[21] S. Y. Toh, K. S. Loh, S. K. Kamarudin, W. R. Wan Daud, *Chem. Engin. J.* **2014**, 251, 422-434.
[22] D. Wang, W. Yan, S. H. Vijapur, G. G. Botte, *Electrochimica Acta* **2013**, 89, 732-736.

The reduction process of GO was performed at constant potential of -1.65 V *vs*. Ag/AgCl, using a deposition time of 360 s, following a protocol reported in previous works[21,22]. The electrochemical cell was assembled in the conventional three electrode configuration, in which the GO/ITO/PET was the working electrode, a platinum coil and an Ag/AgCl acted as counter and reference electrode, respectively. The successful occurrence of the GO reduction was indicated by the transition from white to dark color during the reduction step. Fig. 6.14 B shows a picture of the rGO/ITO/PET thus obtained.

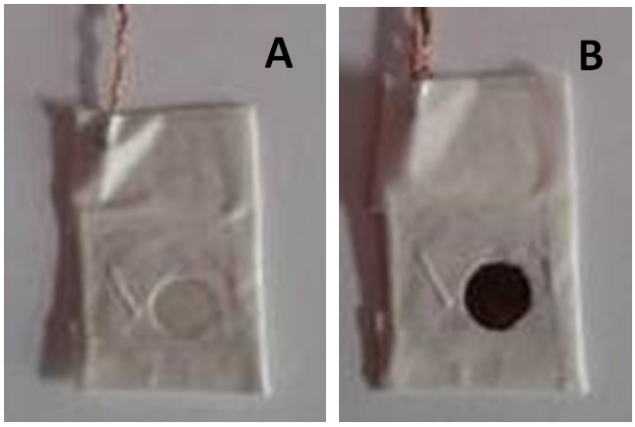

Fig. 6.14*: Pictures of GO thin films A) before and B) after the electrochemical reduction of the modified GO/ITO/PET.*

The various steps, leading to the final rGO product, were followed by cyclic voltammetry in an aqueous solution containing the redox probe K_3FeCN_6 (1 mM) + 0.1 M KCl, as supporting electrolyte. Fig. 6.15 compares typical CVs obtained for the GO-uncoated ITO/PET (black line), the GO-coated ITO/PET (red line) and the rGO/ITO/PET (blue line).

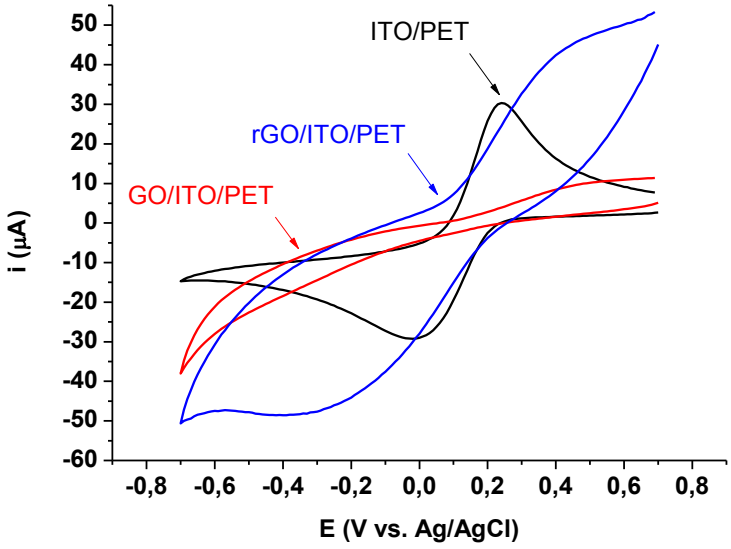

***Figure 6.15**: Comparison of CVs recorded in 1 mM K_3FeCN_6 + 0.1 M KCl aqueous solution for ITO/PET (black line), GO/ITO/PET (red line) and rGO/ITO/PET (blue line). Scan rate 50 mV/s.*

As is evident, the voltammogram recorded at the uncoated ITO/PET substrate is that expected for a conventional electrode of millimeter size, where planar diffusion occurs[23]. The analysis of the response provided a cathodic to anodic peak separation (*ΔEp*) of 0.261 V, which is much larger than the 0.059 V predicted for a one-electron reversible process[23]. This rather high *ΔEp* value can be attributed to a ohmic drop effect. The backward to forward current peak ratio was 0.96, indicating that no homogeneous chemical reactions were coupled to the heterogeneous electron transfer step.

After the ITO surface had been coated with the GO film, the current in the CV dropped to small values (Fig. 6.15, red line), though two small peaks located at -0.4 V (in the cathodic scan) and 0.5 V (in the anodic scan) can still be discerned. These are probably due to the redox probe, which can reach the underlying ITO substrate through physical defects (*i.e.*, pinholes) present within the insulating GO layer. The results are, in general, congruent with what is reported in the literature for conducting surfaces treated with GO layers[3,16,17].

The CV recorded with the electrochemical treated GO/ITO/PET film (*i.e.*, rGO/ITO/PET electrode) displayed a general current enhancement in the voltammetric profile, which was even higher than that obtained with the uncoated ITO/PET substrate (Fig. 6.15, blue line). However, a rather broad couple of peaks (cathodic-anodic), conceivably due to the redox probe, with *ΔEp* of about 0.9 V were observed. The very high peak separation can be attributed to either a very high effect due to ohmic drop or to a very low electron transfer kinetic occurring at the rGO surface. In both cases, these results indicate that the electrochemical procedure adopted for the rGO production was not effective, and therefore the material resulted unsuitable for electrochemical applications.

[23] A. J. Bard, L. R. Faulkner, *Electrochemical Methods*, M. Dekker, New York, **2001**.

In order to further support the above scenario, the local conductivity of the rGO material prepared by electrochemical treatments was investigated by SECM in feedback mode. Fig. 6.16 shows a series of approach curve recorded above the rGO/ITO/PET sample in different locations, in an aqueous solution containing 1 mM K_3FeCN_6 + 0.1 M KCl.

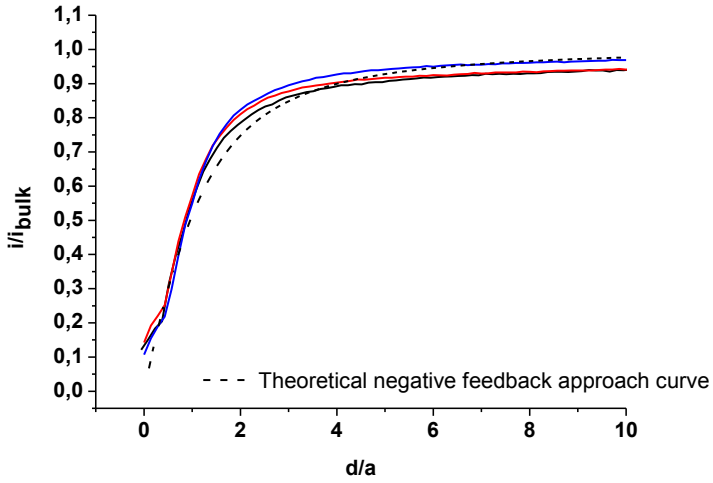

***Fig. 6.16**: Approach curves recorded above rGO/ITO/PET in different locations by using a Pt microdisk of 12.5 µm in radius in 1 mM $K_3Fe(CN)_6$ + 0.1. M KCl (E_{tip} = -0.2 V vs. Ag/AgCl). For comparison, theoretical approach curve for negative feedback (black dotted line).*

As is evident, negative feedback approach curves were in any case recorded, regardless the position. Also, line and two-dimensional scans provided featureless responses of the type shown in Fig. 6.5. These results confirm that the conductivity of the rGO film or the electron transfer process involving the redox mediator at its surface are strongly inhibited. Because of these unsatisfactory electrochemical performance, this material was not further investigated.

Chapter 7: Conclusions

In this thesis various types of investigations, based on Scanning Electrochemical Microscopy (SECM), Microcapillary (MC) and Voltammetric techniques, have been performed for probing and modifying micro- and nano-locations of various surfaces, and to establish the chemical and electrochemical activity of nanostructured materials at the interfaces realised with electrolyte solutions. The main achievements and relevant concluding remarks for each specific topic are summarised below for each chapter.

7.1 Use of micropipette for surface characterization and patterning

The results presented in this chapter have allowed establishing several strategies for obtaining information on spatial distribution and size of small pores, which can be formed when metal substrates are coated with an insulating layer of polymer or metal oxides. The methods are based on scanning micropipettes of micrometer-size orifices, which form micro-electrochemical cells with the investigated substrate. The approach proposed here is particularly useful to investigate the electrochemistry of electroactive species in single submicrometer-sized recessed electrodes, randomly distributed over a wide surface area of the substrate, and with distances between adjacent pores of tens or hundreds of micrometers. The usefulness of the method adopted here to reveal small pores was verified on platinum substrates coated by thin alumina films prepared by r.f. magnetron sputtering, which contained pores of size varying from about 55 to 350 nm and apart from one another more than 100 μm. More generally, the MC-based strategies, proposed here, can be used to establish number and size of defects, pinholes or cracks which can be formed during a variety of technological processes involving deposition of protective thin layers over a metal substrate. Alternatively, it can be employed to decorate, with different catalytic systems, ensembles of recessed micro- and nano-electrodes wired in parallel by the same underlying metal conductor. Also, flat conducting surfaces can be patterned by foreign metallic species. With this regard, in the thesis, an example was reported in which a platinum surface was patterned with arrays of circular silver deposits, each of about 50 μm of diameter. The deposits were made by spherical particles of about 200 nm diameter. In view of the catalytic properties displayed by both platinum and silver, the MC fabricated systems can be employed as micro-electrochemical devices for the detection of small organic and inorganic molecules, such as formic acid, glucose, H_2O_2 and, more in general, reactive oxygen species.

Some theoretical aspects, to rationalize the steady state responses obtained with MC at both flat and recessed substrates, have been underpinned by numerical modeling of mass transport in the microcell formed at the pipette meniscus. These have taken into account the particular geometry of the realized meniscuses and a range of depths of the recess. The simulations were performed with COMSOL Multiphysics, a commercial finite element solver. These simulations are typically conducted in 2D domains assuming an axi-symmetric geometry. Here a few simulations

were conducted in 3D domains devoid of symmetry to include the cases in which the pipette is not centred with respect to the single pore/recess investigated.

7.2 SECM and voltammetric investigations on silver micro- and nano-particles

In this chapter, a comprehensive investigation was performed to investigate the general properties of silver micro- and nano-particles synthesized by various procedures within polymeric matrices. In particular, the chemical properties and reactivity at the sample/solution interface were studied by using scanning electrochemical microscopy and voltammetry. The silver particles were synthesized within a Nafion® and an exopolysaccharide matrix, the latter biosynthesized using a *K. oxytoca* BAS-10 strain.

The silver particles embedded in the Nafion® matrix were produced by mixing water solutions containing $AgNO_3$ at different concentrations and various amounts of Nafion® solutions 0.5% w/v in methanol. The reduction process of the Ag^+ ions was performed by following different chemical or electrochemical procedures. Among them, those based on chemical reduction, using formaldehyde as reductant, provided quite homogeneous and small silver particles, *i.e.*, about 200 nm of diameter. The electrochemical reduction of Ag^+ in silver-loaded Nafion® membranes, cast on the surface of a glassy carbon electrode, proved less effective, as the particles produced were less homogeneously distributed and of micrometer size.

Very small particles, on average, a few nanometer sizes, were instead produced by using the biosynthesized exopolysaccharide material.

The oxidation state of the silver particles embedded within the membranes, were investigated by SECM in feedback mode. From these measurements it was proven that both Ag(0) or Ag(I) forms were present in the various samples and their abundance depended on the amount of $AgNO_3$ initially employed for their preparation. Ag(I) forms present in the various matrices could conceivable be due to the oxygen of air, which could promote the oxidation of Ag(0) forms in the silver particles.

The reactivity of the silver micro- and nano-particles embedded in the polymeric matrices was investigated by coupling SECM with voltammetry (either CV or ASV were utilized). The measurements, in particular, were devoted at establishing either the amount of Ag(I) species released at the sample/solution interface or the relevant concentration profiles due to soluble diffusing species. The media equilibrated with the solid samples were water, water acidified with acetic acid and water/ethanol mixtures. This choice was related to the circumstance that, according to European Recommendations, they can be regarded as food simulants in the food packaging industry. The SECM-CV or SECM-ASV procedures were initially performed using a bulk silver sample, to optimize the methods and to obtain comparative data. The quantification of Ag(I) released was made by using the charge involved in the voltammetric responses and using equations derived assuming a thin layer behavior within the gap formed between the SECM tip and the substrate. The parameters involved in these equations were obtained by performing steady-state voltammetric measurements in the simulant containing $AgNO_3$ without and with supporting electrolyte. This to

render the experimental conditions for the release Ag(I) measurements as close as possible to those generally employed in official tests.

From these investigations, it was found that the amount of Ag(I) released at the interface depended on the size of the silver particles and the matrix in which the samples were immersed. For given amounts of silver loaded in the polymers, the largest concentration of Ag(I) released was observed in water acidified media. The water/ethanol mixture with the highest alcohol content was instead the medium in which the activity of the silver particles was the lowest.

The ability of the various Ag-loaded samples to provide soluble diffusion Ag(I) species is important, as this aspect could imply a potentially higher or lower antimicrobial activity. The antibacterial activity of the various samples towards both Gram positive and Gram negative bacteria is currently under investigation in our laboratory.

7.3 SECM investigation of surface conductivity of graphene thin layers deposited on insulating and conducting substrates

In this chapter, spatially resolved measurements (at micrometer scale) were performed to elucidate some properties of graphene materials. In particular, the measurements were devoted to establish the electronic conductivity of reduced graphene oxides (rGO) deposited onto substrates using a patented procedure based on a pressure/wax-based transferring technique, employing chemical exfoliated graphene materials. The rGO-preparation methods included patterning graphene oxides (GOs) onto PET or ITO substrates in bands of 75 or 500 µm width and 2 mm long, and in disks of 4-5 mm of diameter. GO was then reduced by hydrazine vapor or electrochemically (when deposited on the ITO conducting substrate), following protocols available in the literature. The investigations on either the GO or the rGO films (4-5 nm thick) were performed by using SECM in feedback mode. It was found that the rGO film prepared by the chemical reduction method was more effective than the electrochemical one to obtain rGO having suitable electronic conductivity. This parameter at micrometer scale was evaluated by using a recent procedure reported in the literature, which makes use of the approach curves recorded above the substrate, using redox mediators characterized by a reversible electrochemical behavior. Both a working curve, plotting normalized feedback current against a dimensionless conductivity parameter, and an analytical expression, also based on the registration of approach curves, were employed to obtain conductivity values ranging between 30 mS/cm and 102 mS/cm for the rGO samples prepared by chemical reduction of the GO films. However, SECM measurements performed in the scanning mode, both in line and two-dimension scans, indicated a non-homogeneous distribution of the rGO material across the entire substrate (probably due to the presence of physical defects), when band-shaped films of 500 µm width and a few millimeters long were patterned. Instead, better results were obtained when bands of 75 µm width and a few millimeters long were produced.

Overall, the results obtained in this chapter suggested that the pressure/wax-based transferring technique to pattern GO films, coupled with a chemical reduction approach to produce rGO, is promising for obtaining graphene materials suitable for mass production of electrochemical devices.

Publications and Conferences Participation

Publications in international journals

- D. Battistel, G. Pecchielan, S. Daniele, *Micropipette Contact Technique as a Tool to Reveal, Characterize and Modify Nanopore Electrodes*, *ChemElectroChem* **2014**, 1, 140-146

- D. Battistel, G. Pecchielan, S. Daniele, *Microcapillary voltammetry at flat and recessed conducting surfaces. A theoretical approach*. Submitted.

- G. Pecchielan, D. Battistel, S. Daniele, *Characterisation of silver particles in a Nafion membrane by the use of Scanning Electrochemical Microscopy*. In preparation.

Oral Presentations to international and national conferences

- G. Pecchielan, D. Battistel, S. Daniele, *Investigation on the release of Ag^+ from silver nanoparticles by using Scanning Electrochemical Microscopy and Voltammetry*, YISAC – 20th Young Investigators' Seminar on Analytical Chemistry, Maribor - Slovenia, June 26 – 29, 2013.

- G. Pecchielan, D. Battistel, S. Daniele, *The use of micropipette for surface patterning*, YISAC – 19th Young Investigators' Seminar on Analytical Chemistry, Nova Gorica - Slovenia, June 27 – 30, 2012.

- G. Pecchielan, G. Bonazza, S. Daniele, *Scanning Electrochemical Microscopy and Anodic Stripping Voltammetry to characterize silver nanoparticles at solid/solution interfaces*, XXV National Congress of the Division of Analytical Chemistry of the Italian Chemical Society, Trieste, Italy, September 13 – 17, 2015.

Poster contribution to national conferences

- G. Pecchielan, D. Battistel, S. Daniele, *The use of micropipette for surface patterning. Application to analytical purposes*, XXIII National Congress of the Division of Analytical Chemistry of the Italian Chemical Society, Isola d'Elba, Italy, September 16 – 20, 2012.